

# The H1 Forward Muon Spectrometer at the HERA Collider

J.P. Sutton

A thesis submitted to the University of Manchester for the degree  
of Doctor of Philosophy in the Department of Physics in the  
Faculty of Science.

April 1993

ProQuest Number: 10871295

All rights reserved

INFORMATION TO ALL USERS

The quality of this reproduction is dependent upon the quality of the copy submitted.

In the unlikely event that the author did not send a complete manuscript and there are missing pages, these will be noted. Also, if material had to be removed, a note will indicate the deletion.



ProQuest 10871295

Published by ProQuest LLC (2018). Copyright of the Dissertation is held by the Author.

All rights reserved.

This work is protected against unauthorized copying under Title 17, United States Code  
Microform Edition © ProQuest LLC.

ProQuest LLC.  
789 East Eisenhower Parkway  
P.O. Box 1346  
Ann Arbor, MI 48106 – 1346

TH17850  
(DAEJQ)  
✓ VAS 79958



# Contents

<b>1</b>	<b>Introduction</b>	<b>7</b>
1.1	The Standard Model . . . . .	7
1.2	Structure Functions . . . . .	11
1.3	Additional HERA Physics . . . . .	13
<b>2</b>	<b>HERA and the H1 Detector</b>	<b>16</b>
2.1	The HERA Collider . . . . .	16
2.2	The H1 Detector . . . . .	20
2.3	Calorimetry . . . . .	21
2.4	Tracking . . . . .	26
2.5	Instrumented Iron and Muon Detection . . . . .	28
2.6	Luminosity Monitor and Electron Tagger . . . . .	29
2.7	Trigger and Data Acquisition . . . . .	30
2.8	H1 Simulation . . . . .	31
<b>3</b>	<b>The Forward Muon Detector</b>	<b>33</b>
3.1	General Description . . . . .	33
3.2	Drift Chamber Design . . . . .	34

<i>CONTENTS</i>	3
3.3 The Readout System . . . . .	38
3.4 Track Reconstruction . . . . .	40
3.5 Momentum Resolution of FMD . . . . .	42
<b>4 The Drift Chambers</b>	<b>48</b>
4.1 Operation of Drift Chambers . . . . .	48
4.2 Determination of the Space-Time Relationship . . . . .	50
4.3 Electrostatic Modelling of the Drift Cells . . . . .	52
4.4 Determination of Drift Velocity and T-zero . . . . .	56
4.5 Determination of the Drift Time from Raw Pulse Data . . . . .	64
4.6 Charge Division . . . . .	68
<b>5 Alignment</b>	<b>73</b>
5.1 Introduction . . . . .	73
5.2 The 'Checksum' Method . . . . .	75
5.3 'Angled' Tracks . . . . .	80
5.4 Nature of Beam Halo . . . . .	82
5.5 Alignment with Beam Halo . . . . .	84
5.6 Alignment with Real Beam Halo Data . . . . .	89
5.7 Further Alignment Considerations . . . . .	95
<b>6 <math>J/\psi</math> Physics</b>	<b>97</b>
6.1 $J/\psi$ Production Mechanisms . . . . .	97
6.2 Simulations of $J/\psi$ . . . . .	102
6.3 Effect on Muon Tracks of Passage Through the H1 Detector . . . . .	103

<i>CONTENTS</i>	4
6.4 Reconstruction of $J/\psi$ from their Dimuon Decays . . . . .	107
<b>7 Summary and Conclusion</b>	<b>113</b>
<b>Bibliography</b>	<b>115</b>

### Abstract

The H1 detector started taking data at the electron-proton collider HERA in the beginning of 1992. In HERA, 30 GeV electrons collide with 820 GeV protons giving a strong boost of the centre-of-mass in the direction of the proton (forward direction). For detection of high momentum muons in this region, a muon spectrometer has been constructed. The design of this forward muon spectrometer (FMD) is described and simulations are used to study its momentum resolution. Calibration of the drift chambers from which the FMD is composed is discussed and measurements of the spatial resolution of the drift chambers are presented. Alignment of the drift chambers within the FMD is considered in detail. In particular, alignment using straight tracks produced by penetrating muons resulting from background events in the proton beam is studied using both simulated and real data.  $J/\psi$  production mechanisms at HERA are discussed and simulations of inelastic  $J/\psi$  production via photon-gluon fusion are used to investigate the measurement of muons, resulting from  $J/\psi \rightarrow \mu^- \mu^+$  decays, by the FMD.

No portion of the work referred to in this thesis has been submitted in support of an application for another degree or qualification of this or any other institute of learning.

## Biographical Note

The author was educated at Woodhey High School, Bury between 1979 and 1984 and at Peel Sixth Form College, Bury between 1984 and 1986. He obtained his first degree at Oxford University in 1989. In 1990 he was awarded a Diploma in Advanced Studies in Science from Manchester University. The work presented in this thesis was carried out at Manchester University and DESY, Hamburg.

To my mother and father

This work was supported financially by the Science and Engineering Research Council (S.E.R.C.) between October 1989 and October 1992.

# Chapter 1

## Introduction

### 1.1 The Standard Model

The most fundamental constituents of matter and the interactions between are described by the 'Standard Model' which is discussed in detail in [1, 2]. The standard model is an example of a quantum field theory. In such theories a quantized field  $\hat{\Psi}(\underline{x}, t)$  is introduced, the equation of motion of which is represented by setting up a Lagrangian,  $\hat{\mathcal{L}}(\underline{x}, t)$ , and minimizing the action,

$$\hat{S} = \int \hat{\mathcal{L}}(\underline{x}, t) dt$$

Bosonic fields, corresponding to particles with integer spins, are quantized by introducing the equal-time-commutation relations,

$$[\hat{\Psi}(\underline{x}, t), \hat{\Psi}(\underline{x}', t)] = 0$$

$$[\hat{\Pi}(\underline{x}, t), \hat{\Psi}(\underline{x}', t)] = i\delta^3(\underline{x} - \underline{x}')$$

$$[\hat{\Pi}(\underline{x}, t), \hat{\Pi}(\underline{x}', t)] = 0$$

where  $\hat{\Pi}(\mathbf{r}, t)$  is momentum, canonically conjugate to  $\hat{\Psi}(\mathbf{r}, t)$ , defined by

$$\hat{\Pi}(\mathbf{r}, t) = \frac{\partial \hat{\mathcal{L}}(\mathbf{r}, t)}{\partial(\partial \hat{\Psi} / \partial t)}$$

For fermionic fields, corresponding to particles with integer plus half spins, the commutators are replaced by anti-commutators in the above relations. The quantized excitations of the field,  $\hat{\Psi}(\mathbf{r}, t)$ , are identified as particles. In the standard model, there are twelve Dirac fields, corresponding to spin-1/2 particles. These are divided into three generations, each generation containing two quarks and two leptons. These are shown in table 1.1.

By imposing local gauge invariance and introducing corresponding vector boson fields, interaction terms are produced in the Lagrangian which couple these vector bosons to the Dirac particles. To demonstrate this consider a free Dirac field described by the Lagrangian,

$$\hat{\mathcal{L}} = \hat{\Psi}(i\gamma^\mu \partial_\mu - m)\hat{\Psi}$$

Imposing invariance under the U(1) gauge transformation,

$$\hat{\Psi}'(\mathbf{r}, t) \rightarrow \hat{\Psi}(\mathbf{r}, t) \exp^{i\theta(\mathbf{r}, t)q}$$

the minimum substitution which must be made for  $\partial_\mu$  is  $D_\mu$  where

$$D_\mu = \partial_\mu - iq\hat{A}_\mu$$

and a vector boson field has been introduced,  $\hat{A}_\mu$ . The Lagrangian for the free Dirac field now contains an interaction term,

$$q\hat{\Psi}\gamma^\mu\hat{A}_\mu\hat{\Psi}$$

which couples the vector boson field,  $\hat{A}_\mu$ , to the Dirac field,  $\hat{\Psi}$ , with strength specified by the coupling constant,  $\alpha = q^2/4\pi$ .

Table 1.1: The particles of the Standard Model.

Dirac fermions			
	Generations		
Leptons	$\nu_e$	$\nu_\mu$	$\nu_\tau$
	e	$\mu$	$\tau$
Quarks	u	c	t*
	d	s	b

Vector bosons	
Interaction	Exchange boson
Gravitation	Graviton
Electromagnetism	Photon
Weak	$W^\pm, Z^0$
Strong	$8 \times$ Gluons

Scalar bosons	
H <sup>0*</sup>	The single neutral scalar boson of the minimal Higg's model.

\*Yet to be observed.

The standard model is based on the  $SU(3) \otimes SU(2)_{Left} \otimes U(1)$  local gauge invariance, corresponding to the following gauge transformation of the Dirac fields:

$$\hat{\Psi}'(\underline{r}, t) \rightarrow \hat{\Psi}(\underline{r}, t) \exp(i\theta(\underline{r}, t)q) \exp(i\theta'_{n=1,3}(\underline{r}, t)\tau^n/2) \exp(i\theta''_{m=1,8}(\underline{r}, t)\lambda^m/2)$$

$$U(1) \qquad \qquad \qquad SU(2)_{Left} \qquad \qquad \qquad SU(3)$$

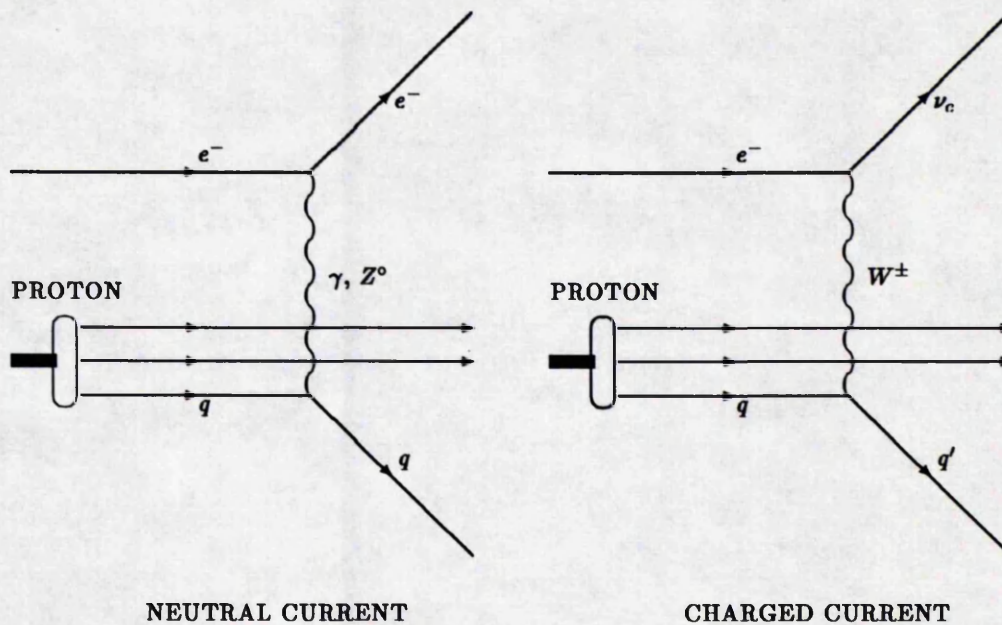
The  $SU(3)$  gauge invariance corresponds to eight vector bosons called gluons. These couple to colour which is carried by the quarks and also by the gluons themselves.  $SU(3)$  and  $SU(2)$  are examples of non-abelian groups. In such groups the gauge bosons couple to each other as well as the Dirac fields. Quarks combine into  $SU(3)$  colour singlets, either composed of three quarks (or three antiquarks) or quark-antiquark pairs to produce baryons (antibaryons) or mesons, respectively.

The  $SU(2)_{Left}$  gauge invariance leads to three vector bosons which couple to weak isospin. The subscript 'Left' indicates that weak isospin is carried by the left chiral component of the Dirac fields only. The  $U(1)$  gauge invariance produces a single vector boson which couples to weak hypercharge. In the standard model, the  $SU(2)_{Left} \otimes U(1)$  gauge symmetry of the Lagrangian is hidden, via the Higg's mechanism [2]. In the minimal Higg's mechanism, an isospin doublet scalar field is introduced which has a non-zero vacuum expectation value which may have any gauge. On choosing a particular gauge, the  $SU(2)_{Left} \otimes U(1)$  gauge symmetry of the Lagrangian appears to be broken leaving only a  $U(1)$  gauge invariance. The weak isospin and weak hypercharge vector boson fields are mixed to produce four vector boson fields: photon,  $W^\pm$ ,  $Z^\circ$ . The photon corresponds to the remaining  $U(1)$  gauge invariance and is responsible for the electromagnetic interaction. The photon remains massless but  $W^\pm$  and  $Z^\circ$  vector bosons acquire mass due to their coupling with the Higg's vacuum field. After the symmetry has been broken, only a real scalar field, the Higg's boson, is left from the original complex scalar doublet. By including interaction terms, coupling the Dirac fields to the scalar doublet field, the Dirac particles are allowed to acquire mass due to their coupling with the Higg's vacuum field, in the same manner as for the  $W^\pm$  and  $Z^\circ$  vector bosons. For quarks, the weak isospin states are not the mass eigenstates. The mixing of the mass eigenstates to give the weak isospin states is given by the Cabibbo-Kobayashi-Maskawa matrix [4] which is a  $3 \times 3$  unitary matrix. The vector bosons in the standard model and the Higg's boson for the minimal Higg's mechanism are shown in table 1.1.

Interactions between particles can be calculated perturbatively using quantum field theory. Each term in the perturbative expansion can be represented by a Feynman diagram in which the interactions can be interpreted to be due to the exchange of virtual particles. The number of vertices at which vector bosons couple to the Dirac particles in a Feynman diagram corresponds to the order of the term in the perturbative expansion. When loops are included in the Feynman diagram, some of the resulting integrals over the loop propagator 4-momenta are divergent. However, in all gauge theories, these divergences can always be absorbed into a redefinition of the 'bare' coupling constants and particle masses to give the physical measurable finite, referred to as renormalized, coupling constants and masses.

## 1.2 Structure Functions

The structure of baryons and mesons are of interest as they allow the nature of the interaction between quarks and gluons to be studied and compared to the predictions from the SU(3) component of the standard model, referred to as quantum chromodynamics. Collisions between electrons and protons allow the structure of the proton to be studied. At high centre of mass energies, the electron actually collides with one of the constituent components of the proton, either one of three valence quarks or a virtual quark or gluon. The simplest Feynman diagrams are:



The cross-section for each of these two processes is given in terms of three structure functions,  $F_{i=1,2,3}^{NC,CC}(x, Q^2)$ , where  $Q^2$  is the 4-momentum transfer carried by the exchange boson and  $x$  is the fraction of the proton's 4-momentum carried by the struck quark. For example, the neutral current cross section is given by

$$\frac{d^2\sigma}{dx dQ^2} = \frac{4\pi\alpha_{em}^2}{xQ^4} \left( y^2 x F_1^{NC}(x, Q^2) + (1-y) F_2^{NC}(x, Q^2) \pm \left(y - \frac{y^2}{2}\right) F_3^{NC}(x, Q^2) \right)$$

where  $y = Q^2/xs$ ,  $s$  is the square of the centre of mass energy of the  $ep$  collision

and  $\alpha_{em}$  is the electromagnetic coupling constant.  $F_3$  is required to account for parity violating V-A interference and contributes with opposite sign for electrons and positrons. Measurement of the neutral and charged current cross sections provides a test of the exchange bosons as described by the standard model and provides information about the structure of the proton.

In QCD, the renormalized strong coupling constant,  $\alpha_s(Q^2)$  decreases with  $Q^2$ . Thus, for small distances within the proton (corresponding to large  $Q^2$ ),  $\alpha_s(Q^2)$  tends to zero and quarks behave as if free - a phenomenon called asymptotic freedom. For ep collisions at large  $Q^2$ , the electron probes a small distance within the proton and picks out a single quark which behaves as if free. This leads to the QCD prediction that the structure functions for the above processes are independent of  $Q^2$  in the limit  $Q^2$  tends to infinity, as is observed. Further, for quarks which are spin-1/2 point-like Dirac particles, the Callan-Gross relation,  $2xF_1 = F_2$  is expected to hold, as is found to be the case [3]. At lower  $Q^2$ , there are QCD corrections, described by the Altarelli-Parisi equations [5], which give the evolution of the structure functions with  $Q^2$ . At low  $x$ , the Altarelli-Parisi equations do not fully describe the QCD behaviour of the structure functions, due to the large gluon density in this region. Refinements of the Altarelli-Parisi equations exist, such as the Fadin-Kuraev-Lipatov kernel [6] and the Gribov-Levin-Ryskin equation [7], which extend the region over which the structure functions can be evolved to lower values of  $x$ .

The structure functions yield information about the probability densities,  $q_{flavour}(x, Q^2)$ , of all the different flavours of quark and antiquark and for the gluons,  $G(x, Q^2)$ , in the proton. For example, the gluon distribution of the proton, which is of particular interest at low  $x$ , can be obtained from measurement of longitudinal structure function,  $F_L = F_2 - 2xF_1$ , at various centre of mass energies [8].

The electron proton collisions provided by the HERA accelerator at DESY ( $\sqrt{s} = 314$  GeV) extends the kinematic region available in the  $x - Q^2$  plane beyond that presently studied, as shown in figure 1.1. Thus, QCD can be tested,  $\alpha_s(Q^2)$  can be determined and the quark and gluon densities of the proton can be measured over the extended kinematic range. In particular, HERA will allow low  $x$  behaviour of the structure functions to be studied.

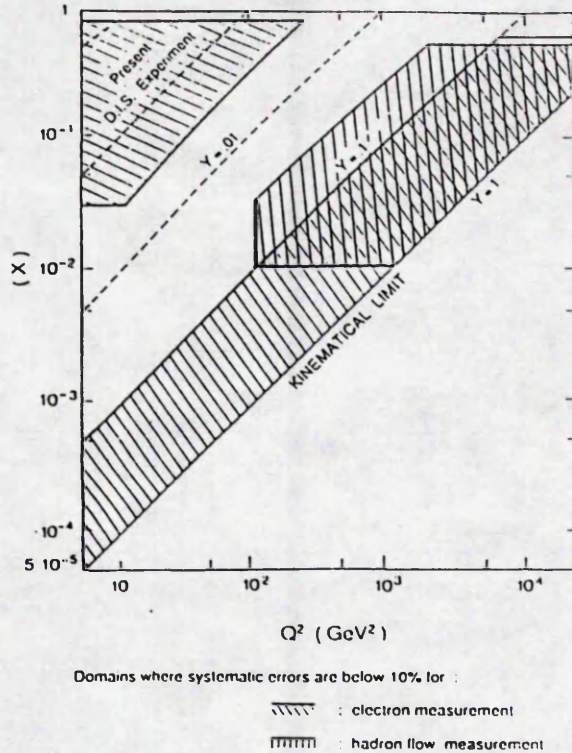


Figure 1.1: The  $(x, Q^2)$  kinematic region available at HERA.

### 1.3 Additional HERA Physics

In addition to the test of QCD provided by the measurement of the proton structure functions over the extended kinematic region available at HERA, a study of the final jet structure will allow a further test of QCD. For example, multi-jet production due to gluon bremsstrahlung and quark pair creation provides a direct test of QCD and allows  $\alpha(Q^2)$  to be measured [9].

HERA can also be considered as a photon-proton collider for low  $Q^2$ , almost real, photon exchange. This is exemplified by  $J/\psi$  production [10] which occurs via several mechanisms of which three are shown in figure 1.2. Figure 1.2a) shows photon-gluon fusion from which the gluon distribution of the proton can be determined. Figure 1.2b) shows the photon coupling to a vector meson such as a  $J/\psi$  which is then diffractively scattered by the proton. Such low momentum transfer, diffractive processes are considered to be due to the exchange of pomerons. Processes such as 1.2b) will allow the nature of the pomeron and photon-hadron

coupling to be studied. At HERA, processes are expected to be observed for the first time which resolve the parton content of the photon. For example the process in figure 1.2c) shows a gluon from proton scattering off a gluon from the photon.

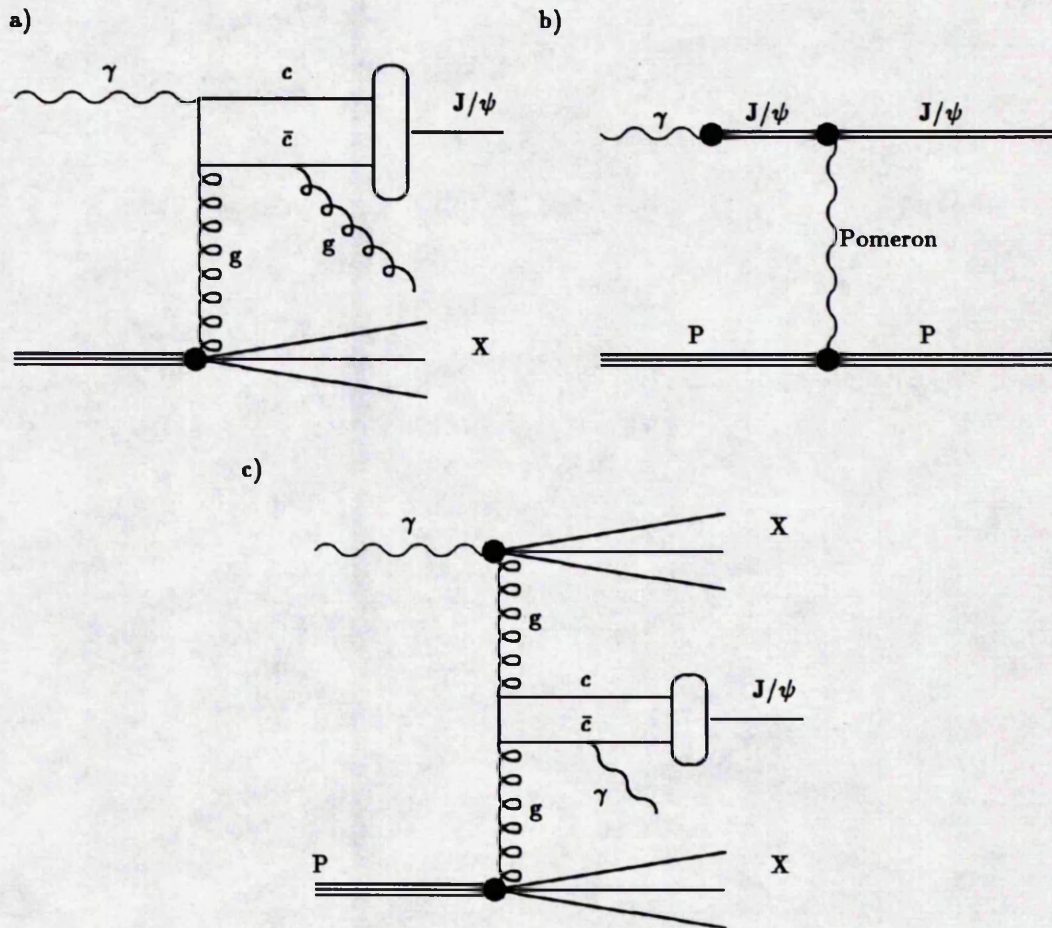
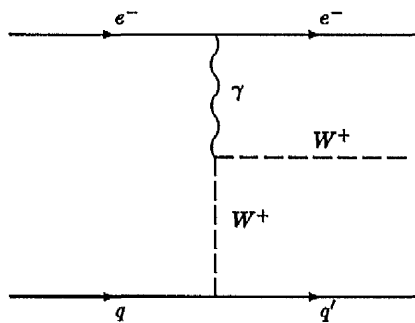


Figure 1.2: Examples of  $J/\psi$  production mechanisms.

More generally, heavy flavour production can be studied at HERA [11]. The main source for heavy quark production is photon-gluon fusion. The photon-gluon process is well defined and calculable in perturbative QCD. It is estimated that  $10^8$  charmed hadrons and  $10^6$  B-hadrons per  $100 \text{ pb}^{-1}$  integrated luminosity will be produced at HERA. Measurement of charm and beauty production will thus provide information about the gluon distribution of the proton and provide a test of perturbative QCD to higher orders. Beauty and charm decay modes may also

be studied and measurements of  $\bar{B}^0 - B^0$  and  $\bar{D}^0 - D^0$  mixing parameters made. The cross-section for top quark production, which is predominantly via the process  $Wg \rightarrow tb$ , is small at HERA, making observation of the top quark difficult, despite there being a kinematic window for top quark production.

Direct production of standard model gauge vector bosons (other than the photon) is low at HERA; of order few tens of  $W^\pm$ ,  $Z^0$  events are expected in  $100 \text{ pb}^{-1}$  [12]. However, such events are an important test of electroweak theory as they allow the  $WW\gamma$  triple gauge boson coupling to be measured [13].



The  $WW\gamma$  vertex is associated with the non-abelian nature of the electroweak interaction and is uniquely determined in the standard model.

At HERA, there is the possibility of detecting new particles which correspond to extensions to the standard model [14]. New heavy quarks or leptons may be observed, such as right handed neutrinos. These may couple to new heavy vector bosons, such as right handed gauge bosons. New gauge bosons may also be observed indirectly as propagators. There is the possibility of discovering excited leptons, as predicted by composite models. Almost any theoretical scheme beyond the standard model which makes a connection between quarks and leptons predicts hybrid particles called leptoquarks or leptogluons. Such particles may be observed at HERA, either directly or indirectly. Supersymmetry predicts as yet unobserved partners for all known particles. These supersymmetric particles may be observed at HERA, the ease of detection depending on the supersymmetric scheme being considered. Higg's production is estimated to be of order of only a few per  $100 \text{ pb}^{-1}$  [12], making detection unlikely at HERA.

## Chapter 2

# HERA and the H1 Detector

### 2.1 The HERA Collider

The HERA collider at DESY, Hamburg is the first electron (positron) - proton collider [15, 12]. It consists of two independent accelerators, housed in the same underground tunnel, which are designed to store 210 bunches of 820 GeV protons and 30 GeV electrons (or positrons) respectively. To store the 820 GeV protons in the HERA ring of radius 797 m requires a bending magnetic field of 4.68 T and hence, superconducting magnets must be used. Head on collisions between the two counter rotating beams are possible at four interaction points, on straight sections, spaced uniformly around HERA's 6.3 km circumference. At these interaction points, the bunch crossing interval is 96 ns, to produce the design luminosity of  $1.5 \times 10^{31} \text{ cm}^{-2} \text{ s}^{-1}$ . The layout of the HERA rings and the position of the experimental halls is shown in figure 2.1. The main parameters of the HERA rings are listed in table 2.1.

The electron (positron) beam can be longitudinally polarised which is useful for electroweak physics studies. Longitudinal polarisation is achieved from the natural transverse polarisation of a storage ring, by a series of magnets preceding and following the interaction region which respectively rotate the electron spin vector to longitudinal and then back to transverse. These magnets are arranged so as to use

Table 2.1: The main parameters of the HERA rings.

	p	e
Nominal energy/GeV	820	30
Polarization Time/min	—	28
Luminosity/cm <sup>-2</sup> s <sup>-1</sup>	1.5 × 10 <sup>+31</sup>	
Interactions points	4	
Crossing angle/mrad	0	
Circumference/m	6336	
Magnetic field/T	4.68	0.165
Number of particles/10 <sup>13</sup>	2.1	0.8
Injection energy/GeV	40	14
Filling time/min	20	15
$\sigma_x$ /mm at I.P.	0.29	0.26
$\sigma_y$ /mm at I.P.	0.07	0.02
$\sigma_z$ /mm at I.P.	110	8.0
Energy loss per turn/MeV	6.24 × 10 <sup>-6</sup>	127
RF-power/MW	1	13.2

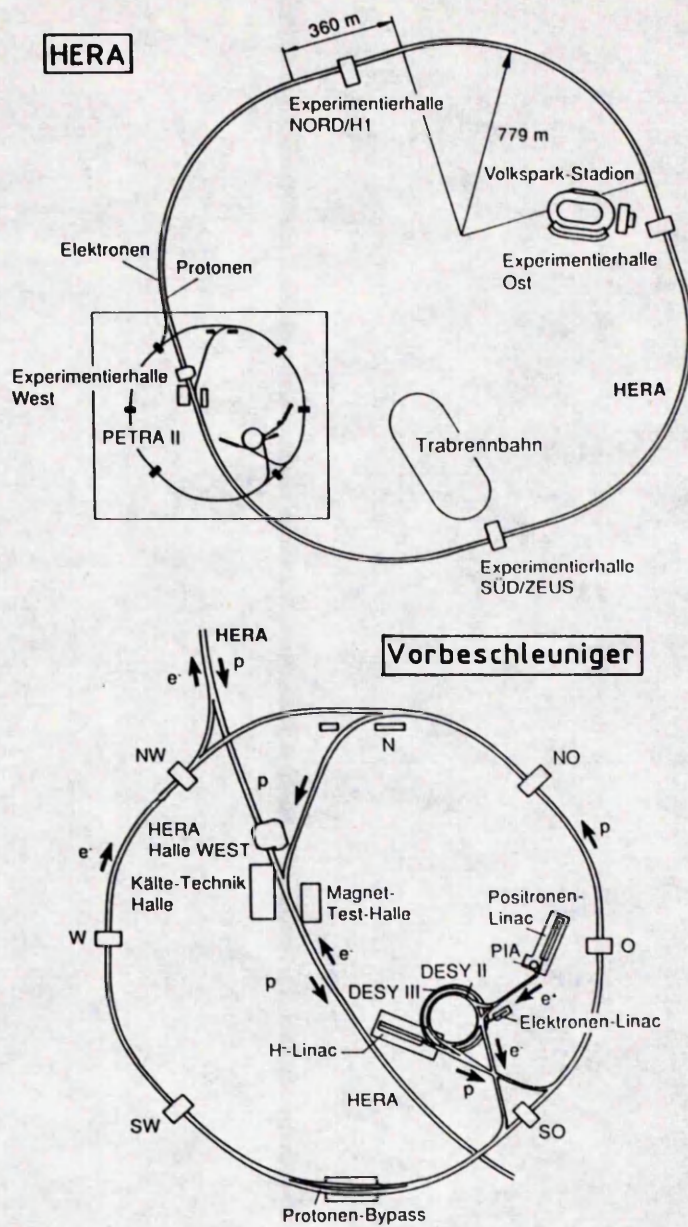


Figure 2.1: The layout of the HERA accelerator and pre-accelerators.

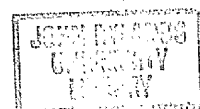
the difference between the cyclotron orbital and the Larmor spin precession frequencies, to produce the spin rotation. It is estimated that a longitudinal polarisation of up to 80% could be obtained.

The electron (positron) injection complex is based on available accelerators. Electrons (positrons) from a 500 MeV linear accelerator are accumulated on a small storage ring before being injected into DESY II where they are accelerated to 7 GeV. They are then transferred to the modified PETRA II ring and accelerated to 14 GeV. Finally, they are injected into the HERA electron ring and accelerated to 30 GeV. A whole new chain of pre-accelerators was required for the HERA proton beam. Negatively charged hydrogen ions are produced by a 50 MeV linear accelerator and then stripped of electrons upon their injection into DESY III where the protons are accelerated to 7.5 GeV. The protons are then transferred to PETRA II, accelerated to 40 GeV and injected into the HERA proton ring where they are accelerated to 820 GeV. The layout of the HERA pre-accelerators is shown in figure 2.1.

For beam stability, the beam crossing angle has been fixed at  $0^\circ$ . To achieve this, the electron beam is deflected into the interaction region; however, this results in a flux of synchrotron radiation. With several synchrotron absorbers and collimators added along the beam pipe to reduce the synchrotron radiation, the rate of spurious hits due to synchrotron photons is predicted from simulations to be handleable [16].

Interaction of beam protons and electrons with the residual gas in the vacuum pipe produces high multiplicity events in the interaction region [16]. For the proton beam, the expected interaction rate with beam-gas is  $3 \text{ kHz m}^{-1}$  and the HERA detectors are expected to be sensitive to interactions up to 100 m upstream of the interaction point. For the electron beam, the expected interaction rate with beam-gas is  $1 \text{ kHz m}^{-1}$ . Due to the lower electron energy, the detector sees only about  $\pm 5 \text{ m}$  of the beam line around the interaction point.

Assuming a lifetime of 10 hr for the proton beam, a proton loss rate of  $300 \text{ kHz m}^{-1}$  is expected [16]. This is considerably higher than the interaction rate with the residual gas. Most of these off momentum protons will be lost due to interactions with the beam-wall at the narrow points in the beam pipe, such as the proton beam quadrupoles. The synchrotron absorber masks nearest to the



interaction point are also significant as they will produce high multiplicity events in the tracking region.

Two general purpose detectors, H1 and Zeus, are situated at the North and South interaction points respectively. Services to the machine are supplied from the surface at West Hall, which is located on the DESY site. There is a third HERA experiment at East Hall, HERMES [17], which uses the polarised electron beam of HERA in collision with a polarised atomic beam at  $90^\circ$  to measure the proton and neutron spin dependent structure functions.

## 2.2 The H1 Detector

The H1 detector [16, 18] has been designed to investigate the physics programme outlined in the previous chapter. The resulting H1 detector design is shown in figure 2.2. The asymmetric design of the H1 detector reflects the asymmetric nature of the collisions produced at the HERA storage ring between 820 GeV protons and 30 GeV electrons. The collision products are Lorentz boosted in the laboratory frame along the proton direction (forward direction) and emphasis must thus be placed on detection in the forward direction, where track densities and momenta are much greater than in the barrel or rear regions.

On travelling outwards from the interaction region, the H1 detector consists of the following components:

- The system of tracking chambers which is divided into two components: the central and the forward tracker.
- The calorimeters which consist of the liquid argon electromagnetic and hadronic calorimeter in the forward and central region, a lead-scintillator electromagnetic calorimeter in the backward region and a copper-silicon pad hadronic plug calorimeter close to the beam pipe in the very forward region.
- A large superconducting coil which provides a homogeneous axial magnetic field of 1.2 T in the central and forward tracking regions. A superconducting

compensation magnet, with a maximum field of 6 T is included to produce a zero integrated field along the beam axis for beam stability.

- The iron magnetic flux return yoke which is instrumented to provide a 'tail-catcher' for the liquid argon hadronic calorimeter and to provide a muon filter and tracker. This is supplemented in the forward region by the forward muon spectrometer, which improves muon identification and tracking in the forward region.

## 2.3 Calorimetry

In order to accomplish the experimental programme at HERA, the H1 detector must have good energy flow measurement, requiring good energy resolution with good absolute energy resolution and a high degree of hermeticity with a minimum of dead material. This is necessary, for example, for the accurate measurement of neutral and charged current structure functions and to infer the presence of neutral penetrating particles such as neutrinos or photinos. Precise energy flow measurement is provided by the calorimeter which is divided into two components: electromagnetic which detects electrons and photons and hadronic which detects hadrons.

When a particle is incident on a calorimeter, it interacts with the material to produce secondary particles, which in turn generate tertiary particles, and so on, resulting in a shower. The incident particle energy is determined by measuring the energy lost by the shower due to ionisation or excitation of material in the calorimeter. The energy resolution  $\sigma_E/E$  varies as  $1/\sqrt{E}$ , determined by the fluctuation in the number of particles produced in the shower, and thus, calorimetry becomes increasingly important with increasing track energies. For electromagnetic calorimetry, the shower results from bremsstrahlung of electrons and pair production from photons. In hadronic calorimetry, the shower is produced by inelastic nuclear collisions which result in the production of secondary hadrons. In a hadron shower a significant fraction of the incident hadron energy is lost by nuclear processes which do not produce an observable signal, such as breakup of nuclei. As

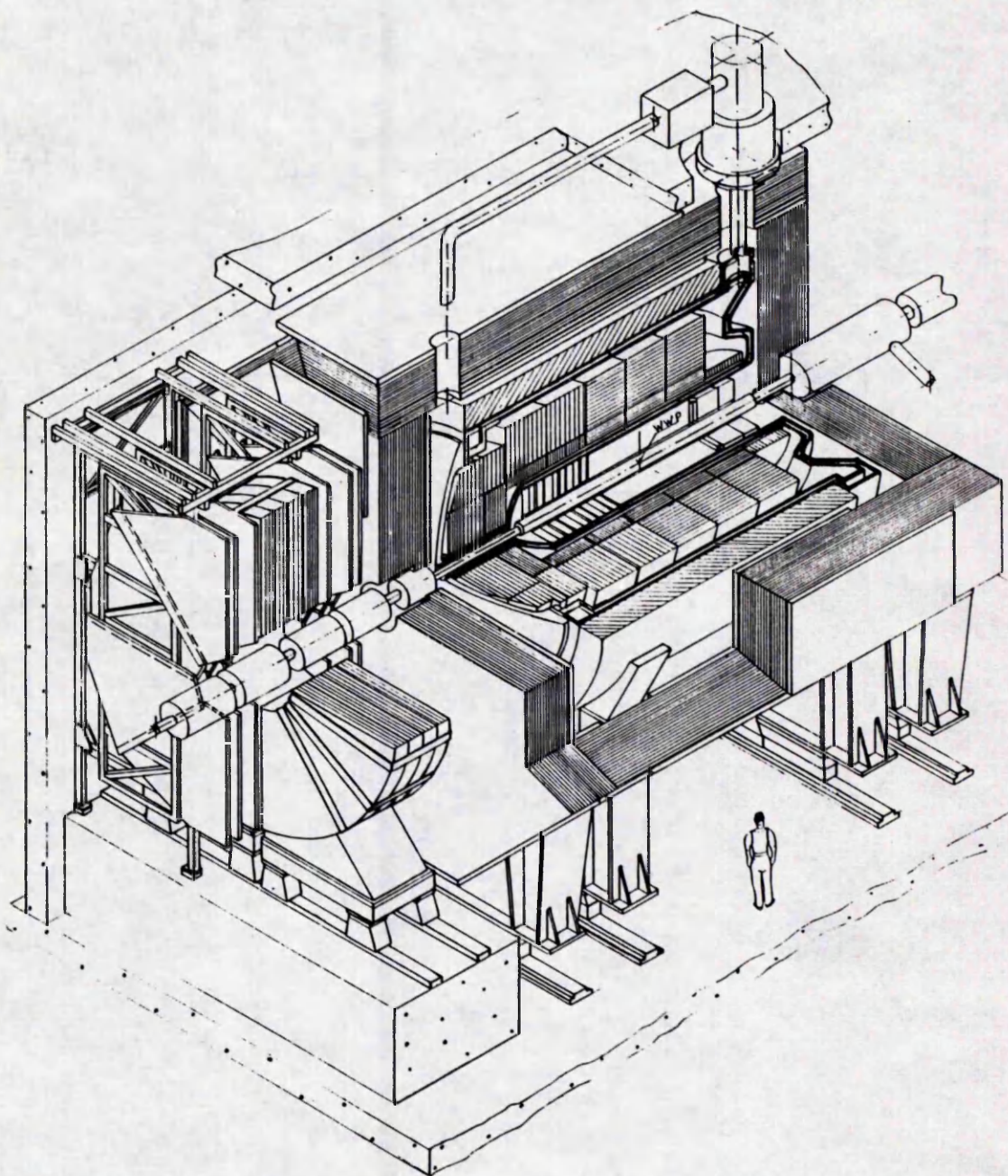


Figure 2.2: The H1 detector.

neutral and charged pions produce electromagnetic and hadronic cascades respectively, the energy measured by the hadronic calorimeter fluctuates depending on the ratio of neutral to charged pions in the hadronic shower. These fluctuations can be compensated for, as described later.

Electromagnetic calorimetry for the H1 experiment is provided by the inner part of the liquid argon calorimeter in the forward and barrel region and by the lead-scintillator calorimeter in the backward region. Hadronic calorimetry is carried out by the outer part of the liquid argon calorimeter in the forward and barrel region and by the copper-silicon pad 'plug' calorimeter in the very forward region. The instrumented iron serves as a hadronic shower tail catcher in the central and forward region and as the hadronic calorimeter in the backward region.

The liquid argon calorimeter consists of stacks of absorber plates, lead for the electromagnetic calorimeter and stainless steel for the hadronic calorimeter, contained in a single liquid argon cryostat to minimize the amount of dead material, as shown in figure 2.3. The eight fold  $\phi$ -segmentation with highly non-projective cracks in the hadronic part is used to minimize energy leakage through cracks. The charged component of the showers which develop in the absorber plates produce ionization in the liquid argon filled gaps between the plates. This charge is collected by high voltages across the gap, onto pads which vary from  $3 \times 3 \text{ cm}^2$  in the forward direction to  $8 \times 8 \text{ cm}^2$  in the backward direction in electromagnetic calorimeter and which have double these dimensions in the hadronic calorimeter. These pads form towers which are longitudinally segmented, the charge collected by the pads within these segments being summed together before being readout. The segmentation of the liquid argon calorimeter is shown in figure 2.4. Measurement of the longitudinal and transverse development of showers is very important for electron identification and allows the fluctuations in the electromagnetic and hadronic components of the hadronic showers to be compensated for. Good transverse segmentation of the calorimeter is also required to give good shower centre determination, allowing tracks and jets detected by the tracking devices to be matched to the corresponding shower in the calorimeter. The expected energy resolutions for the liquid argon calorimeter are  $\sigma_E/E = 55\%/\sqrt{E} \pm 2\%$  for hadrons and  $\sigma_E/E = 10\%/\sqrt{E} \pm 1\%$  for electrons, where  $E$  is in GeV.

The backward electromagnetic calorimeter is composed of 88 calorimeter

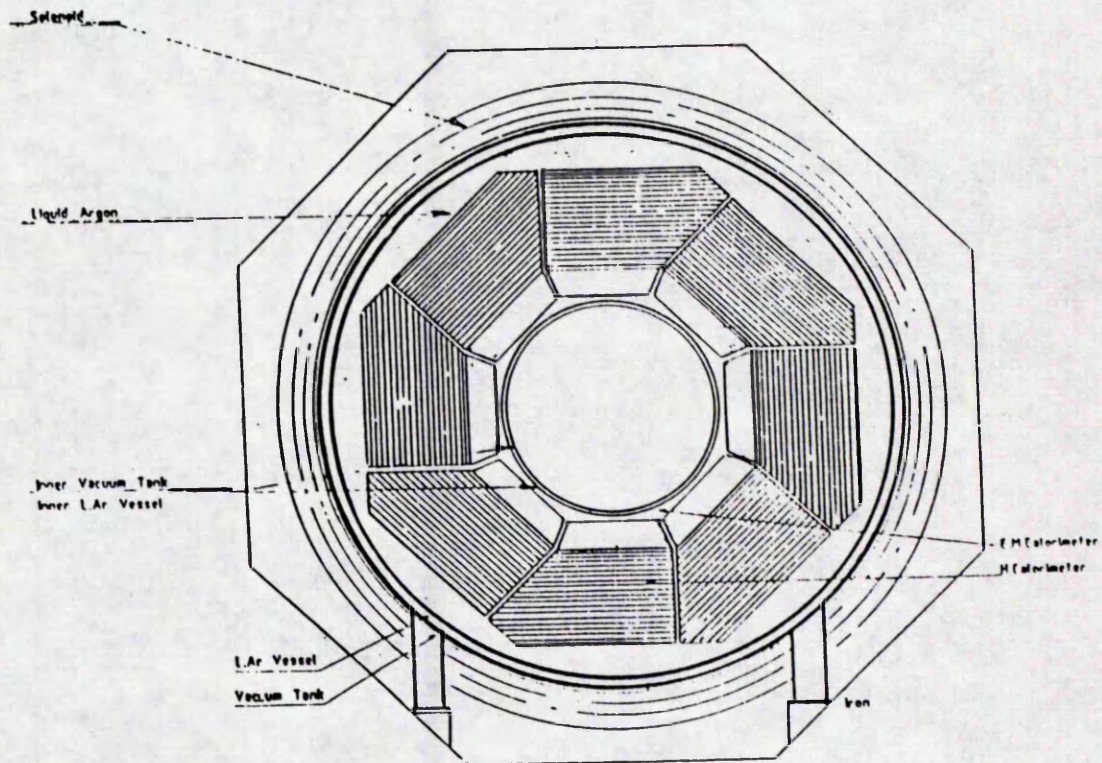


Figure 2.3: The liquid argon calorimeter (transverse cross section).

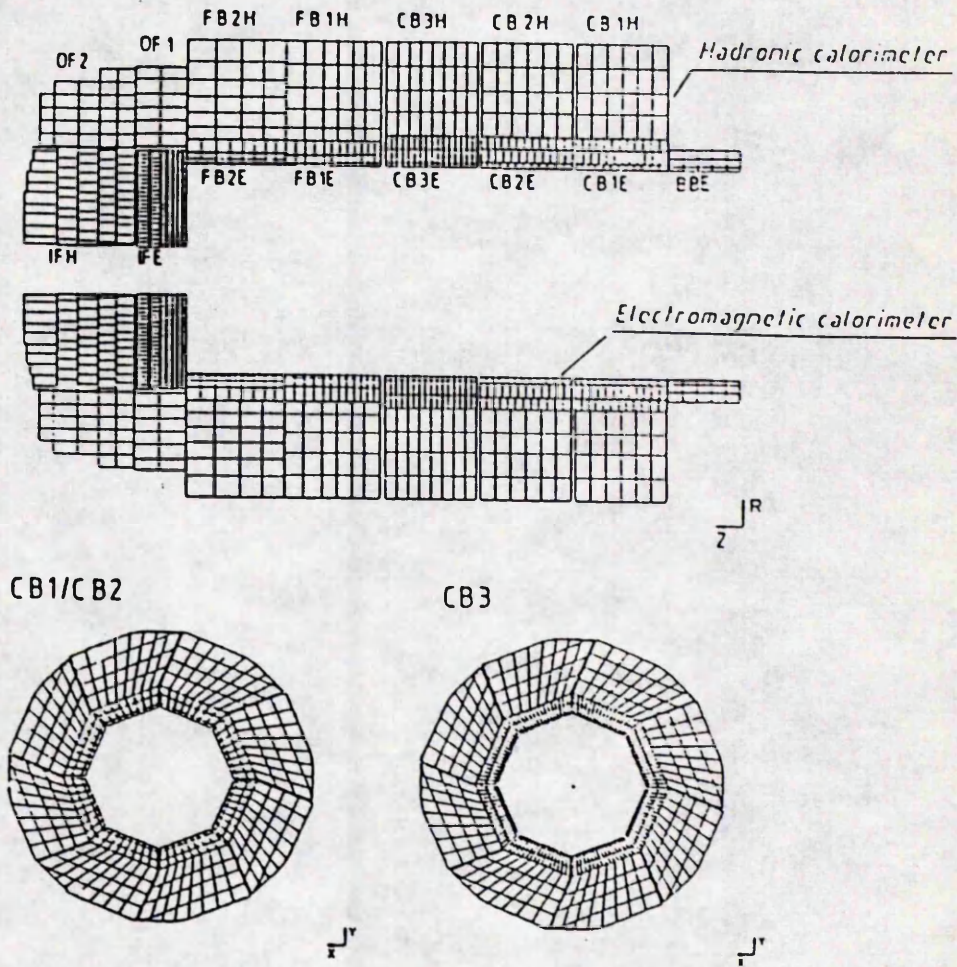


Figure 2.4: Segmentation of the liquid argon calorimeter along beam axis (top) and  $\phi$ -segmentation (bottom).

stacks parallel to the beam pipe which define the transverse segmentation. These stacks consist of layers of lead-scintillator sandwiches, the lead acting as the absorber material and the electromagnetic shower produced being sampled in the layers of scintillator. Readout of the scintillation light is done, via wavelength shifters which extend over the full length of the stacks, by photodiodes. The energy resolution for electrons is expected to be  $\sigma_E/E = 10\%/\sqrt{E} \pm 1\%$ , where  $E$  is in GeV.

The plug calorimeter in the very forward direction consists of eight layers of copper absorber with a silicon pad between each layer to sample the hadronic shower. The silicon detectors are divided laterally into  $5 \times 5$  cm<sup>2</sup> cells and are linked together longitudinally in pairs for readout.

## 2.4 Tracking

The tracking detectors allow the event topology and jet structure to be determined. The system of tracking chambers used by the H1 detector is shown in figure 2.5. The tracking detectors are designed to provide, in conjunction with the strong homogeneous field generated by the large superconducting coil, good momentum resolution,  $3 \times 10^{-3}$  (GeV/c)<sup>-1</sup>, over most of the angular range for individual charged tracks. They also provide improved electron identification, both independently and by comparison of the calorimetric energy measurement with the tracking momentum measurement.

When a charged particle passes through the gas of tracking detector, it creates ionization along its path. In a drift chamber, the resulting negative charge drifts in a moderate electric field towards a sense wire where it is amplified in the strong electric field near the wire. The signal induced on the sense wire allows the drift distance to be determined accurately from the drift time and by measuring how the charge was divided between the two ends of the sense wire, the distance along the sense wire can be roughly determined. With several such hit coordinates, the particle's track can be determined and by measuring the bend of the track in a magnetic field, the momentum of the particle can be obtained. Measurement of the amount of ionization produced,  $dE/dx$ , provides improved electron identification. In a multiwire proportional chamber, there is no drift field and instead the ionization is

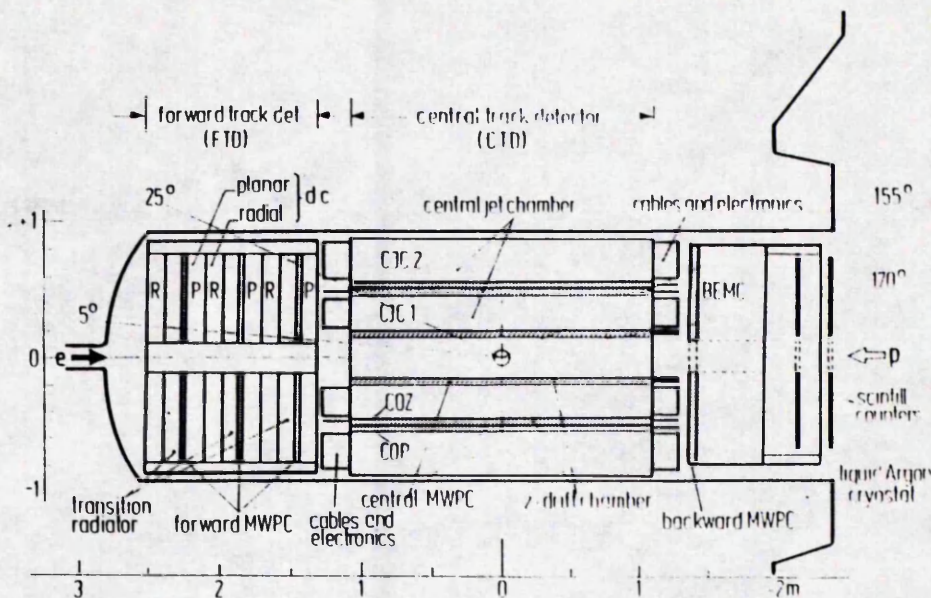


Figure 2.5: The system of tracking chambers of the H1 detector.

directly amplified by a strong electric field. The spatial resolution of such chambers is limited to the wire separation, but they provide fast track information, useful for the trigger.

The central tracker consists of six sets of cylindrical chambers which are, moving radially outwards from the interaction region, the inner multiwire proportional chamber, the inner  $z$ -chamber, the inner jet chamber, the outer  $z$ -chamber, the outer multiwire proportional chamber and the outer jet chamber. In the jet chamber, the wires are strung parallel to the beam pipe and, hence,  $r\phi$  is measured accurately from the drift time and  $z$  is measured roughly from charge division.  $dE/dx$ -measurements are also made to improve electron identification. Accurate  $z$ -measurement is provided by the  $z$ -chambers in which the wires are strung around the beam pipe so as to form polygons. The  $z$ -chambers also provide rough  $r\phi$  measurement by charge division.

The forward tracker consists of three identical sections called supermodules, each composed of a planar module, a multiwire proportional chamber, a transition radiator and a radial module. Each planar module has three layers of parallel wires

oriented at  $60^\circ$  in  $\phi$  to each other. Combining the accurate drift time measurements from these three layers in a supermodule, allows precise space points to be determined. The radial module consists of layers of wires strung radially, providing accurate  $\phi$ -measurement and rough  $r$ -measurement. In addition to  $dE/dx$ -measurement, electron identification is improved by the transition radiator which consists of layers of polypropylene foils. When a charged particle crosses the boundaries of the polypropylene foil, soft x-rays are produced (transition radiation) which are detected by the radial chambers. The intensity of the x-ray production depends on the Lorentz,  $\gamma = \text{Energy}/\text{Mass}$ , of the charged particle and is only significant for electrons, allowing them to be discriminated.

There is a further (backward) multiwire proportional chamber behind the central tracker, in addition to the forward and central multiwire proportional chambers, to complete the system of multiwire proportional chambers. These provide prompt track information for the trigger, an independent value for the bunch crossing time and a fast reconstructed vertex position which aids discrimination of beam background events.

## 2.5 Instrumented Iron and Muon Detection

Good lepton identification, in general, is important for heavy flavour studies and for the detection of new exotic particles. So, in addition to electron identification, muon identification is also of importance. Measurement of high energy muons is also necessary to preserve the hermeticity of energy flow measurement. Muons are identified by their penetration through the calorimeters and instrumented iron yoke.

The return yoke for the magnetic flux is longitudinally divided into slabs of iron between which are single layers of limited streamer tubes with wire and pad readout to provide the tail catcher for the hadronic calorimeter. These pads form towers which match the towers in the liquid argon hadronic calorimeter and these towers are longitudinally segmented, the signal from the pads within each segment being summed together. These provide an energy resolution of  $\sigma_E/E = 100\%/\sqrt{E}$ , where  $E$  is in GeV. Limited streamer tubes are similar, in principle, to proportional

chambers, except that they are operated in limited Geiger mode which produces considerably larger amplifications in the field near the sense wire. Thus, the signal induced on the wires, pads and strips requires no further electronic amplification. There is also a double and a triple layer of limited streamer tubes with wire and strip readout, mounted on the inside and outside of the yoke respectively, for muon detection. Muon momentum is best measured by the central and forward trackers. However, the large bending field inside the liquid argon calorimeter and the return yoke allows an independent measurement of the muon momentum to be made by the instrumented iron. This improves momentum resolution, particularly at higher momenta and also improves the discrimination of muons resulting from pion and kaon decays.

In the forward direction, in addition to the increase in track density and track momentum due to the Lorentz boost, the magnetic bending produced by the solenoid is reduced leading to a poorer muon momentum resolution. Thus, a forward muon spectrometer is introduced to improve muon identification and momentum resolution in the forward region,  $3^\circ < \theta < 17^\circ$ . It consists of an iron toroidal magnet, before and after which are layers of drift chambers. Muons are tracked by the drift chambers and their momenta determined from their bend in the magnetic field of the iron toroid.

## 2.6 Luminosity Monitor and Electron Tagger

The luminosity monitor consists of a photon detector and an electron tagger, situated 107 m and 37 m in the backward direction, respectively. They are both crystal shower counters instrumented with photomultipliers to measure the Čerenkov radiation produced by the shower. Čerenkov radiation is emitted by a charged particle passing through a medium if its velocity is greater than the local phase velocity of light in that medium. By measuring  $ep \rightarrow ep\gamma$  bremsstrahlung, these detectors provide a fast, coarse luminosity monitor. In addition, the electron tagger is used to provide a trigger for photoproduction events.

## 2.7 Trigger and Data Acquisition

The high bunch crossing rates and high beam background rates lead to the requirement of a sophisticated trigger and data acquisition system [19].

The analogue output signals from the subdetectors are fed into frontend digitising units where they are pipelined, this allowing the trigger decision to be delayed. The analogue output signals from subdetectors are also fed to the subdetector trigger where they are converted into so called trigger elements in which the decisions are encoded in bits. These trigger elements are sent to the central trigger logic where they are combined to provide the level one and level two triggers, after typically  $2 \mu\text{s}$  and  $20 \mu\text{s}$ , respectively, if the event satisfies the loaded trigger condition. The level one trigger freezes the frontend pipelines and the level two trigger signals the readout of the digital information from the frontend pipelines. In parallel, a level three trigger based on a microprocessor refines the trigger and possibly arrives at a reject condition which aborts the event readout. Without a reject condition, the event is readout completely and the frontend buffers released again for the next trigger. The data from each subdetector is placed in so called multievent buffers, the event being identified by a unique mark. The event builder task, which proceeds in a completely asynchronous manner to the previous operations, collects the data from each subdetector and assembles the full event. Once the event has been built it is presented to the level four filter farm which works on precise information of the full event to make a filter decision. If the event passes the level four filter farm it is sent off for final logging to the main DESY computing centre.

Trigger information is provided by the calorimetry, tracking and muon detection, of varying degrees of refinement, to the different trigger levels. Tracking uses multiwire proportional chambers, in addition to the drift chambers, to provide trigger information. Two walls consisting of a double layer of scintillators, the veto wall and time-of-flight counters, give prompt time information which can be used to veto against beam halo tracks. The veto wall is 6.5 m away from the interaction point in the backward direction and covers the same area as the beam tunnel. The time-of-flight counter covers the area behind the backward electromagnetic calorimeter and is required to detect beam halo tracks which pass, undetected by the veto wall, close to the beam pipe or which were produced in the beam pipe following the veto wall.

## 2.8 H1 Simulation

The H1 detector is simulated as closely as reasonable by the 'H1SIM' program [20] which reads in generated events, in the form of particle four vectors and their generation vertices, and produces a file of simulated detector responses in the same form as is produced by the real detector. Figure 2.6 shows the flow of the simulation data for the H1 detector.

H1SIM is divided into three parts: GEANT, DIGI, TRIG. The main part of the simulation program is the GEANT module which tracks the passage of the particles resulting from the generated event through H1 and requires most of the CPU time. It simulates all the physics associated with passage of particles through matter, including multiple scattering, secondary particle generation, particle decays and interactions, the effect of magnetic fields and shower development, using the GEANT code [21] from CERN upgraded with shower parameterization packages based on the ALGORIX and GFLASH algorithms for faster calorimeter simulations. The output from the GEANT module, referred to as hit banks, are the  $xyz$ -coordinates of the entry and exit points of the particle trajectories through the sensitive parts for the tracking detectors and energy depositions for calorimeter type detectors. The DIGI module converts these hit banks into detector response banks which have the same form as those produced by the real detector. The DIGI module simulates the detection characteristics of the sensitive parts of the real detector, such as resolutions. The TRIG module calculates the trigger response using the detector response banks as input. All non-event data such as the detector geometry or detector resolutions is contained in the H1 database.

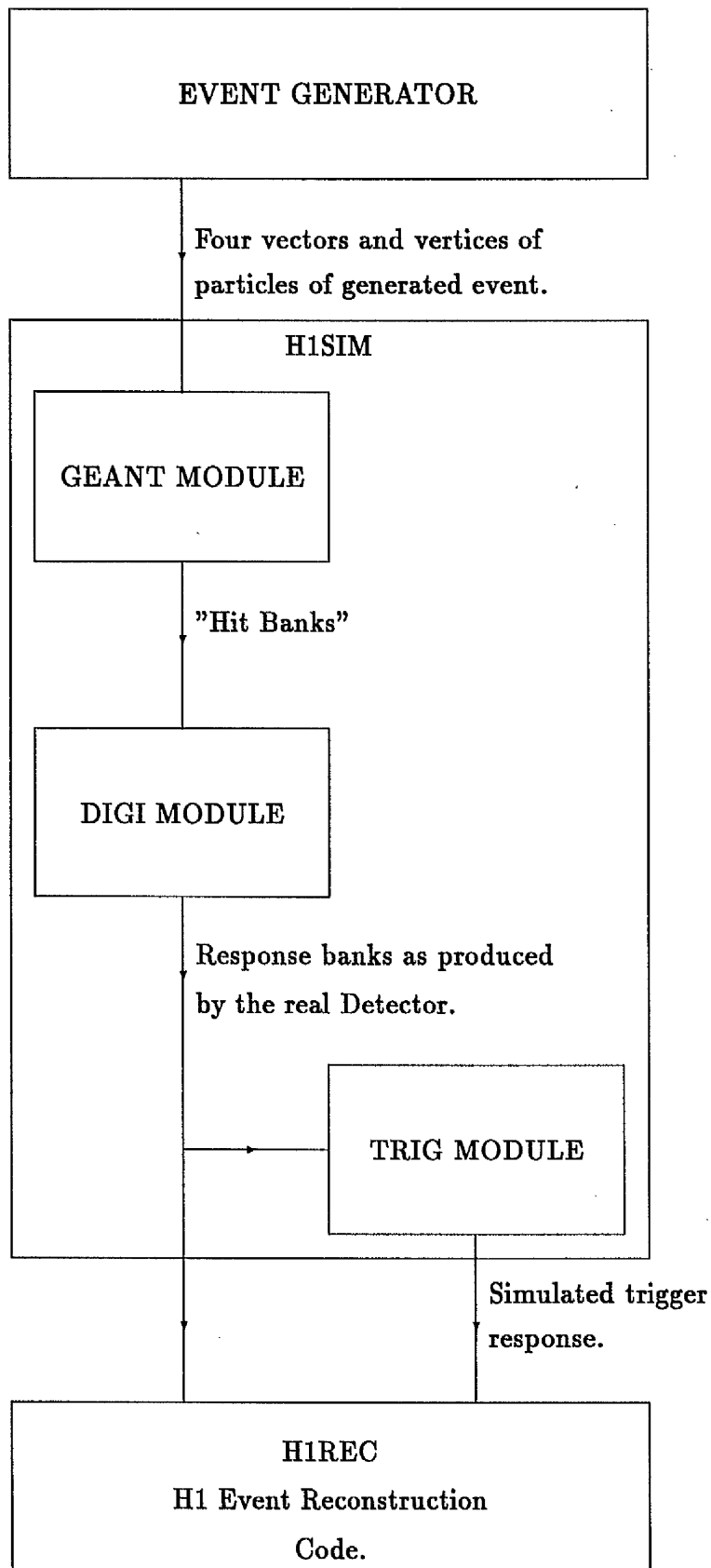


Figure 2.6: Flow of simulation data for the H1 detector.

## Chapter 3

# The Forward Muon Detector

### 3.1 General Description

The forward muon spectrometer is designed to measure particles which have penetrated through the instrumented iron return yoke of H1, largely muons, in the polar angles  $3^\circ < \theta < 17^\circ$ . The muons are detected by drift cells which form the four theta layers and two phi layers. On either side of a toroidal magnet there is a theta-phi-theta combination of layers, as shown in figure 3.1, which allow the track of a muon to be determined. The bend of the muon track in the magnetic field of the iron toroid allows the momentum of the muon to be measured. Each of the layers is made up of two half-layers consisting of four octants in the form of a maltese cross, which are superimposed to produce a full layer of eight octants. The two half-layers are displaced relative to each other along the beam axis, so that the preamplifiers can be attached to the end of cells without any loss of acceptance. Figure 3.2 shows a full layer with one of the half-layer drawn with a solid line and the other with a dashed line. The radial extent of the layers varies so as to cover the polar angular range of  $3^\circ < \theta < 17^\circ$ . The octants which make up the theta and phi layers are composed of single sense wire drift cells. The drift cells in the theta and phi octants are oriented with their sense wires arranged as shown in figure 3.3. The theta layers essentially measure the polar angle,  $\theta$ , and the phi layers the azimuthal angle,  $\phi$ , from a measurement of the drift time. These measurements are supplemented by

a charge division measurement obtained by comparing the signals read out from the two ends of the sense wire. Each octant is composed of two layers of drift cells which are displaced by half a cell width, as shown in figures 3.3 and 3.4, to resolve left-right ambiguities and also to allow the determination of  $t$ -zero. In figure 3.3 cells represented by dashed lines are behind cells represented by the solid lines and cells represented by dotted lines are in front. The total number of drift cells in the forward muon detector is 1520.

The two layers of drift cells which form an octant are mounted on an aluminium frame using dowels which position the drift cells to  $50 \mu\text{m}$  parallel to the drift axis and to 1 mm along the remaining two axes. A pair of octants are mounted on an aluminium 'door' frame to form a quadrant. Four quadrants are supported by a main iron frame to form a full layer of eight octants. The octants on the door frames closest to the central vertical axis of the detector and the door frames themselves can be moved outwards, to allow access to the beam pipe.

High beam background rates at low polar angles may be encountered. To accommodate for this possibility, the sense wire gain voltage of the 12 innermost drift cells of the theta octants can be controlled separately from the outer drift cells. For the phi octants the inner section of drift cells, shaded grey in figure 3.3, have been designed to move radially outwards.

The iron toroid is 1.2 m thick and constructed from eight semicircular steel modules with an inner radius of 0.65 m and an outer radius of 2.9 m. The toroid can be opened up to allow access to the beam pipe. Twelve rectangular coils provide the field, each of which is fifteen turns of copper tube,  $11.5 \times 11.5 \text{ mm}^2$ , through which cooling water flows. The field varies in strength from 1.75 T at the inner radius to 1.5 T at the outer radius.

## 3.2 Drift Chamber Design

All drift cells have a rectangular cross-section with an ionisation depth of 2 cm, a width of 12 cm and lengths between 40 cm and 240 cm. A single central sense wire divides the drift cell into two 6 cm drift regions. The sense wire is  $50 \mu\text{m}$

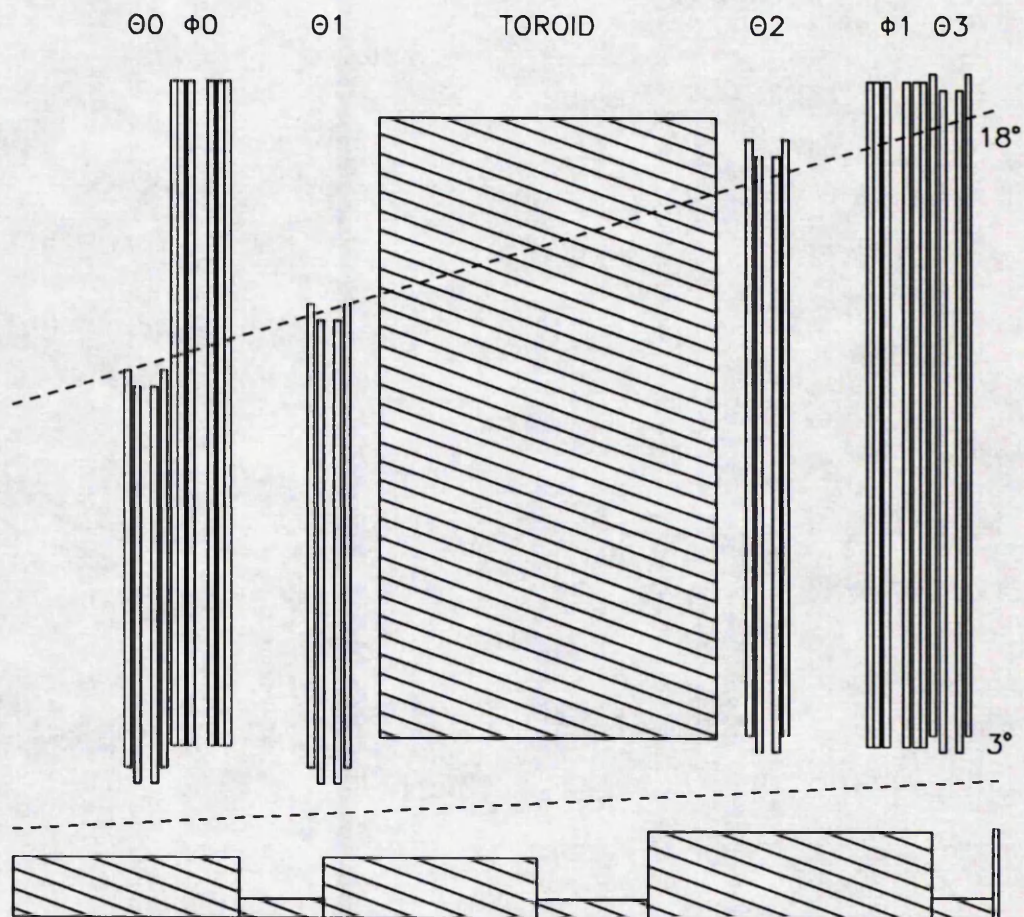


Figure 3.1: Schematic diagram of the forward muon detector.

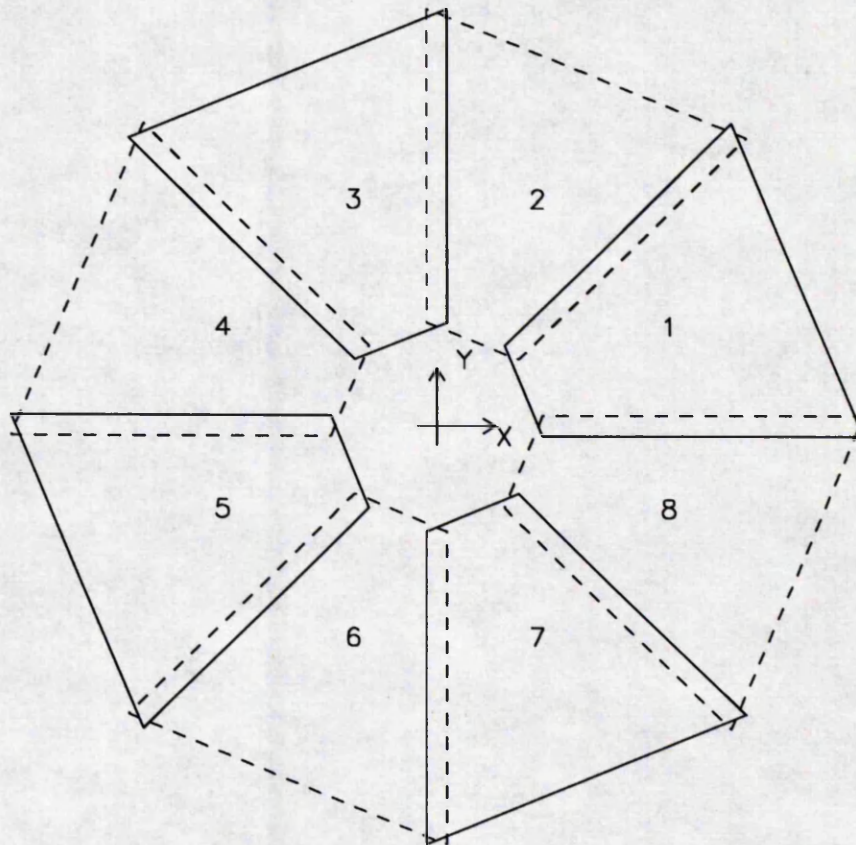
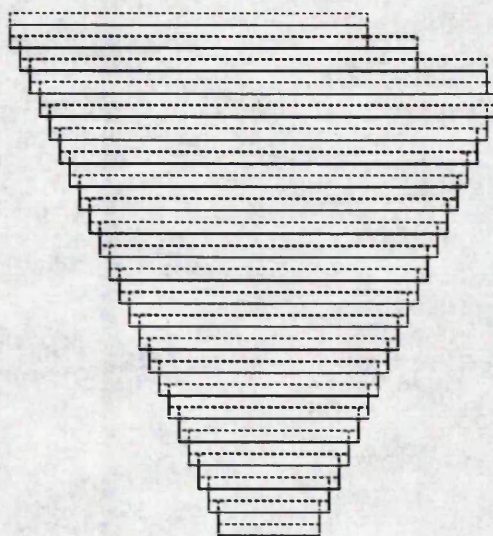
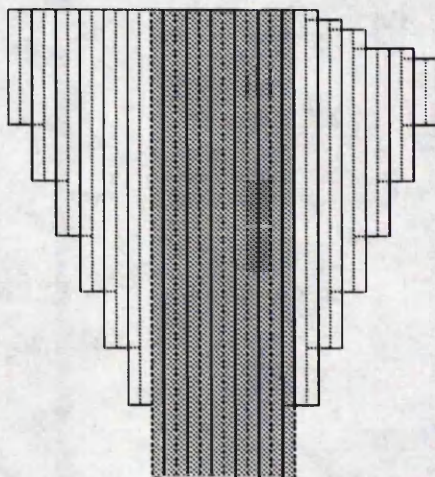


Figure 3.2: Full layer composed of eight octants.



THETA OCTANT



PHI OCTANT

Figure 3.3: Diagram of individual theta and phi octants.

thick nichrome resistive wire except for the inner short cells where the diameter is  $40\ \mu\text{m}$ . For cells longer than 1.5 m there is a wire support in the middle. As illustrated in figure 3.4, each cell is comprised of two PCB planes, copper-coated on both sides, and 0.7 mm thin extruded aluminium profiles. The outer copper surface of the PCB and the aluminium profiles are kept at ground to form a screened box. The inner copper surface of the PCB has been machined to form 4 mm wide strips running parallel to the sense wire, separated by 2 mm gaps. These are connected to a 230 M $\Omega$  metal film resistor chain mounted on the end cap and act as drift electrodes to produce a uniform drift field. The end caps are made of moulded Noryl with high precision holes to locate the crimp pins for fixing the sense wires and provide holes for the gas connections. They also contain a dowel hole for accurately mounting the cell on the aluminium octant frame. One end contains the high voltage distribution resistor chain and the sense wire readout connection isolated from the sense wire high voltage supply by a 1 nF ceramic disc capacitor. At the other end, sense wires of adjacent cells are linked together via a 330  $\Omega$  resistor to reduce the number of readout channels required.

The gas currently chosen for the chambers is 92.5% argon, 5% CO<sub>2</sub> and 2.5% methane which is mixed and purified in a recirculator. The drift voltage across the distribution resistor chain is 3 kV and this produces an average drift field of 0.45 kV cm<sup>-1</sup>. The sense wire is kept at 4.5 kV, so as to give a gain potential difference of 1.5 kV, relative to the centre drift electrode. The high voltage is supplied to the detector by a 120-channel CAEN 127 system via distribution boxes which are situated on the detector. There is a continuous monitoring of the gas composition and flow rates as well as of high voltage, communicated via an Apple Macintosh II ci in the H1 control room. From this work station it is also possible to control the high voltage of the detector and the toroid magnet.

### 3.3 The Readout System

The signals are readout into eight channel preamplifiers of standard H1 design mounted along the sides of the octants. The output pulses are fed through 50 m long multi-coaxial cables to F1001 flash analogue to digital converters (FADC).

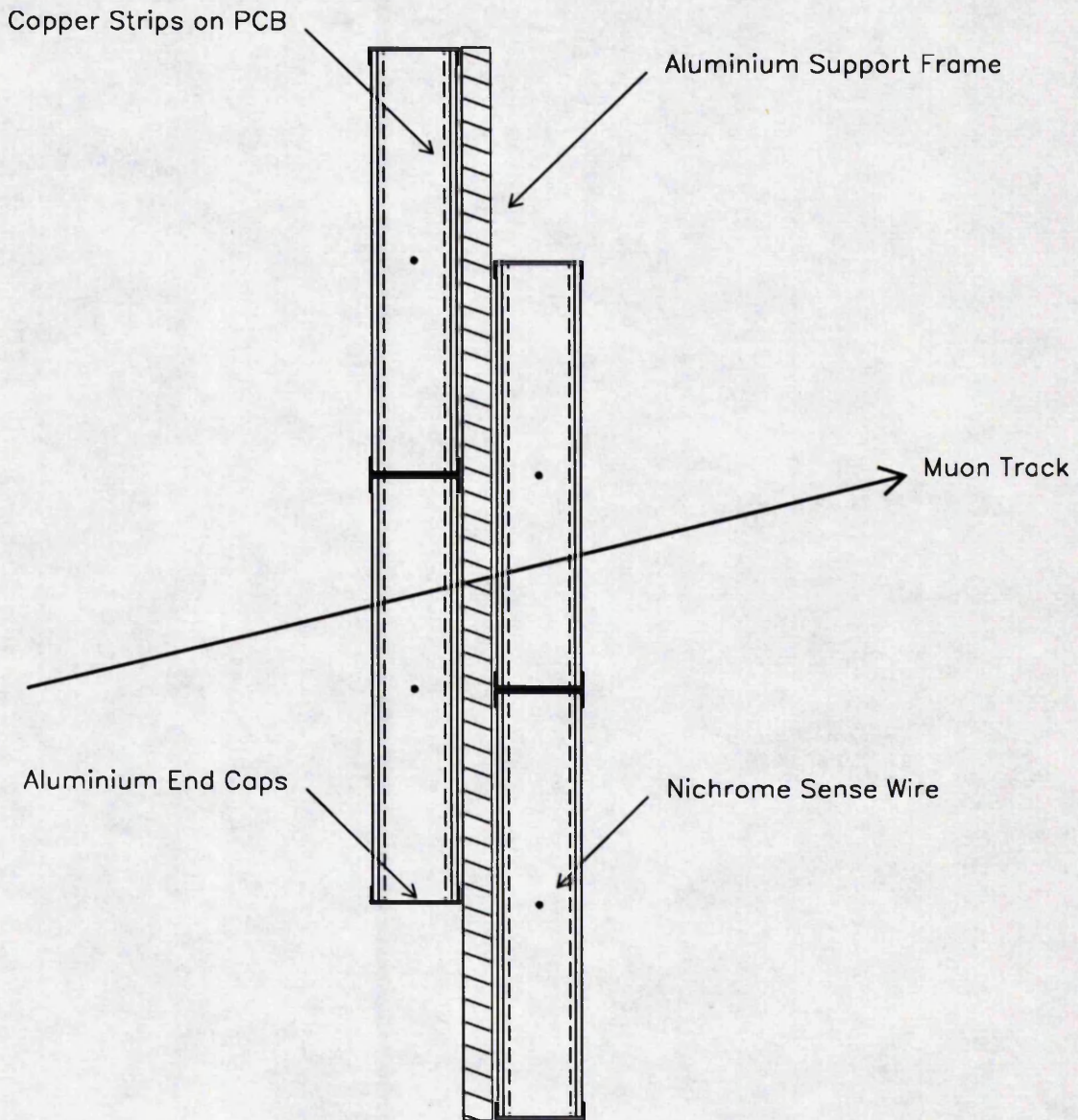


Figure 3.4: Cross-section of forward muon drift cells mounted on an octant frame.

Signals are digitised at ten times the HERA beam crossing frequency in time bins of 9.6 ns and then stored in a frontend pipeline which has a depth of 256 time bins. The level one trigger stops the FADC sampling, freezing the last 2.5  $\mu$ s of readout history in its memory. On receiving the level two trigger, the SCANNER unit reads out the 256 time bins of the 256 FADC channels of one crate into its own buffer. Simultaneously with the readout, the data is scanned for the occurrence of pulses. Pointers to the time bins where a pulse crosses a pre-set threshold are stored separately. This information is used by a frontend processor to readout only the selected pulses, reducing the amount of data retained. The frontend processor also performs online signal (Qt) analysis to determine the pulse drift time and charge. The readout chain for a linked pair of cells is shown in figure 3.5.

### 3.4 Track Reconstruction

The reconstruction code [22] first converts the charge and drift time information produced by the Qt analysis of chamber hits into space points. Assuming that the track points back to the nominal interaction vertex, hits in the two planes of drift cells of an octant are matched and the ambiguity in drift direction resolved. Using these paired hits and vertex information, a track is extrapolated to the other theta layer on the same side of the toroid and a search for hits, paired or unpaired, is made within a cone in the estimated track direction to find possible track segments. Straight line fits are made to each of these possible track segments which are then selected according to a  $\chi^2$ -cut. In future the information from the phi layers will also be used.

By extrapolating pre-toroid segments through the toroid for a muon with the minimum momentum of interest for both muon charges, a region is defined after the toroid inside which segment are considered for linking to form tracks. For possible segment pairs, a first rough estimate of the inverse track momentum,  $p^{-1}$ , is made from the change in track theta angle and the integrated field through the toroid. Based on this estimate, the pre-toroid segment is extrapolated through the toroid for several values of inverse track momentum,  $p^{-1}$ , to determine the minimum in the  $\chi^2$  versus  $p^{-1}$  curve. A quadratic fit is then made to the five points about

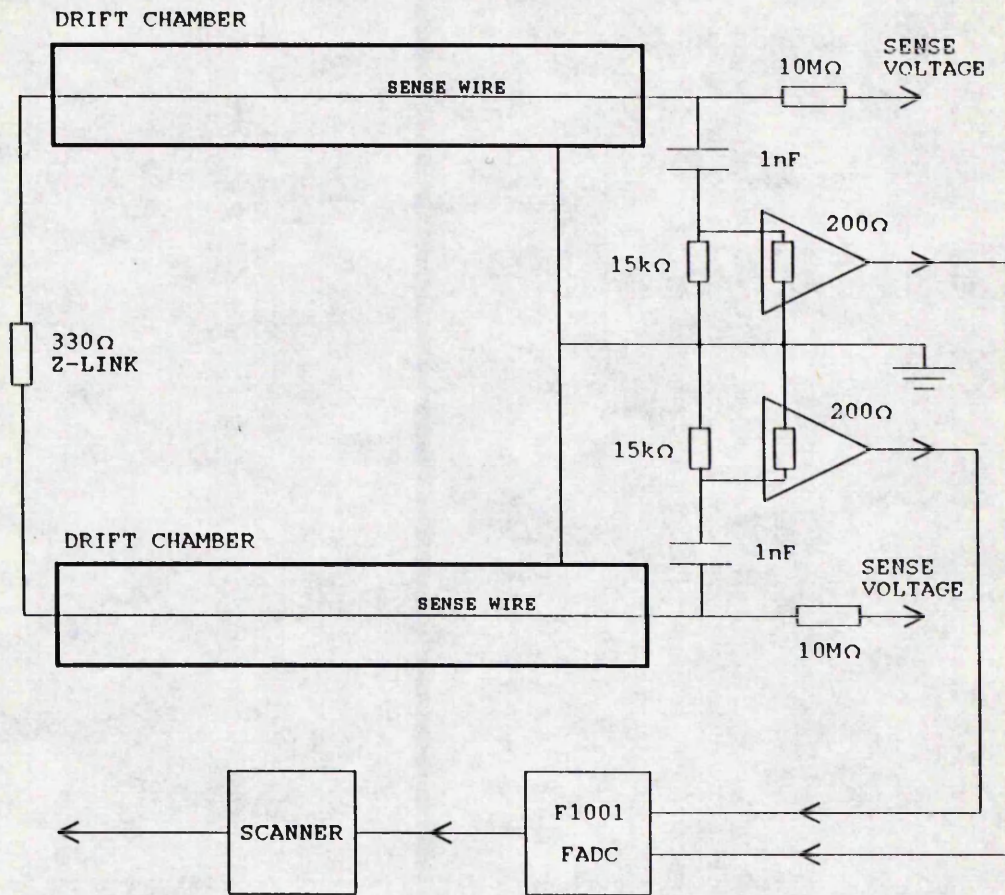


Figure 3.5: Readout chain for forward muon drift cells.

this minimum and the track momentum is taken to be the minimum of the fitted quadratic curve, for which a final extrapolation is done. A  $\chi^2$ -cut is made on the final fitted tracks and duplicate tracks are removed, retaining only the track with the lowest  $\chi^2$ .

The extrapolation through the toroid is done in small steps for which the muons trajectory can be represented by a circular path. In each step energy loss of the muon and multiple scattering are taken into account. The parameterization used for the magnet field in the toroid is:

$$B = \frac{1.68}{r^{0.098}}$$

where  $B$  is the magnetic field strength at a radius,  $r$  from the  $z$ -axis of the H1 detector. The magnetic field lines form concentric circles centred about the  $z$ -axis. This describes the magnetic field in the real toroid to a precision of 1% and is checked by measurement of the fringe field. This parameterization of the magnet field of the toroid is also used by the simulator of the H1 detector.

### 3.5 Momentum Resolution of FMD

To evaluate the performance of the FMD, simulations with the forward muon toroid field on were carried out with muon tracks, which were generated in a plane immediately in front of the FMD and pointed back to the nominal H1 vertex. They were generated at two phi angles ( $25^\circ$  and  $40^\circ$ ), with either charge and with six discrete momenta (3, 5, 10, 20, 40 and 80 GeV/c). The two phi angles correspond to tracks which pass through the central axis of an octant ( $\phi = 25^\circ$ ) and through the edge of an octant ( $\phi = 40^\circ$ ). This allows the effect of the charge division coordinate to be studied which is expected to be particularly significant in this case where only the theta octants were present. The generated tracks were evenly distributed in theta between  $3^\circ < \theta < 18^\circ$  to prevent the results being significantly effected by large number of tracks passing through the gap between cells. Gaussians were fitted to the difference between the generated and reconstructed inverse momentum,  $((\frac{1}{p})_{rec} - (\frac{1}{p})_{gen})$ , of these muon tracks for each combination of track phi

angle, charge and momentum. Figure 3.6 shows the fractional statistical error in the reconstructed inverse track momentum,  $(\sigma_{\perp})_{rec}/(\frac{1}{p})_{gen}$ , against  $p_{gen}$ . Figure 3.7 shows the systematic shift between the reconstructed and generated inverse track momentum as a ratio of  $(\frac{1}{p})_{gen}$  against  $p_{gen}$ . The distribution of the theta angle of the generated tracks for reconstructed tracks covered the range  $4.5^{\circ} < \theta < 17.0^{\circ}$ . Thus, out of the 595 muon tracks generated for each combination of track phi angle, charge and momentum, 496 tracks are expected to be reconstructed by the FMD. Figure 3.8 shows the efficiency for each combination of track phi angle, charge and momentum defined to be the percentage of these 496 generated tracks actually reconstructed with an inverse momentum in the range zero to twice the generated inverse momentum.

The momentum of a reconstructed muon track is essentially determined from the change in the theta angle of the track,  $\Delta\theta$ , on passing through the magnetic field of the iron toroid,  $B$ ,

$$\Delta\theta = \frac{0.3BL}{p} \quad (3.1)$$

where  $p$  is the muon track momentum in GeV/c,  $L$  is the width of the toroid in m,  $B$  is in Tesla and  $\Delta\theta$  is in radians. The resolution of the momentum measurement is primarily dictated by multiple scattering of the muon track in the iron toroid. The bulk of the multiple scattering for muons results from elastic Coulomb scattering of the muons by the iron nuclei within the toroid. The distribution of the angular deflections,  $\theta_{scat}$ , due to multiple Coulomb scattering is a Molière distribution which is approximately Gaussian, except at large angles where the deflection is due mainly to single scattering. A Gaussian approximation can be used for non-critical applications with an rms of the deflection in a particular plane given by [23]

$$\sigma_{scat} = \frac{14.1 \times 10^{-3}}{p\beta} Z_{inc} \sqrt{\frac{L}{L_R}} \left[ 1 + \frac{1}{9} \log_{10} \left( \frac{L}{L_R} \right) \right] \quad (3.2)$$

where  $p$  is the muon momentum in GeV/c,  $\beta = \frac{v}{c} \approx 1$ ,  $Z_{inc}$  = the modulus of the charge on the incident particle,  $\frac{L}{L_R}$ , is the thickness of the iron toroid in radiation lengths, (120/1.76) for the iron toroid and  $\sigma_{scat}$  is in radians. Combining equations

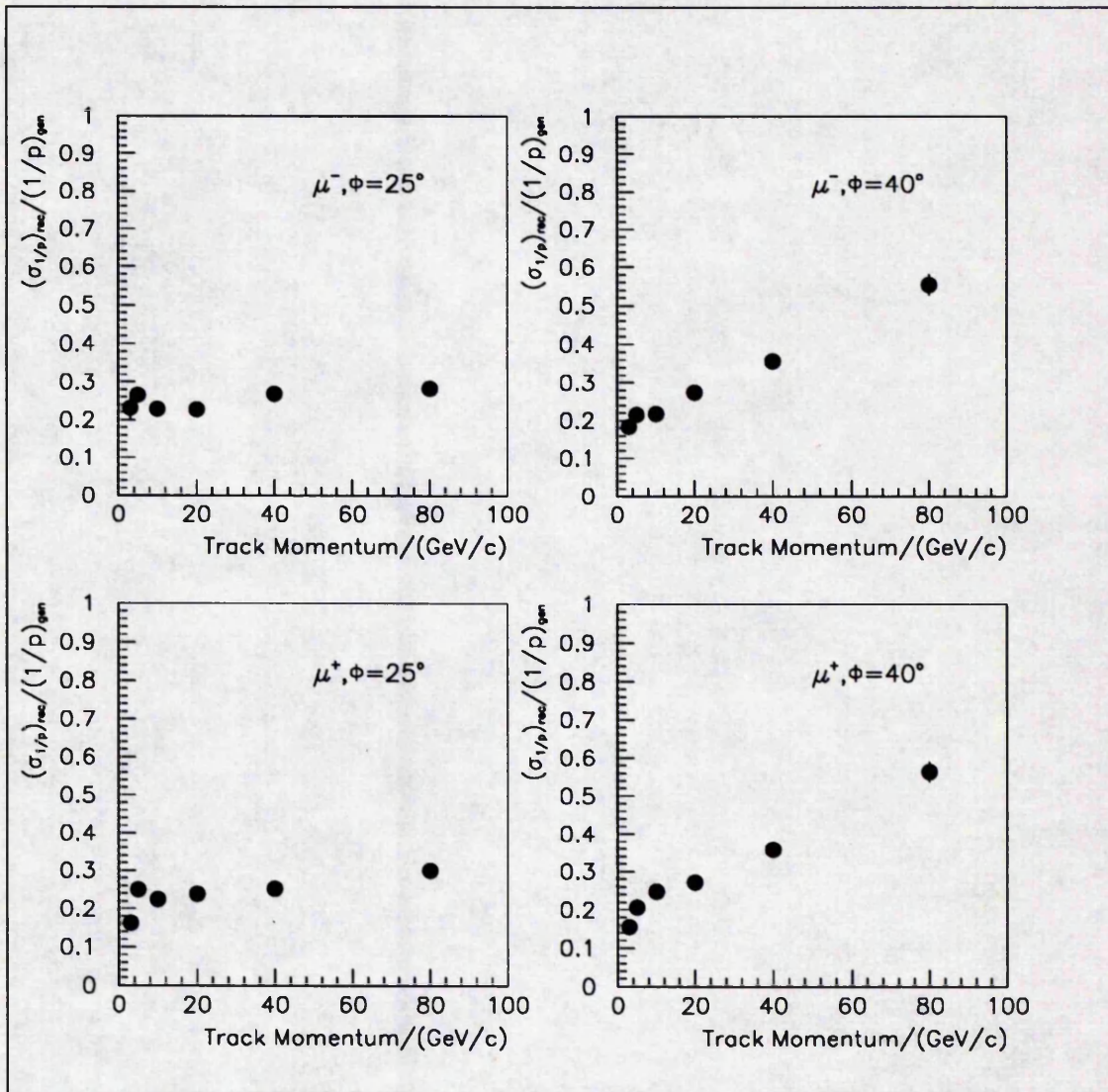


Figure 3.6: Statistical error in the reconstructed inverse track momentum for the FMD,  $(\sigma_{1/p})_{rec}/(1/p)_{gen}$ .

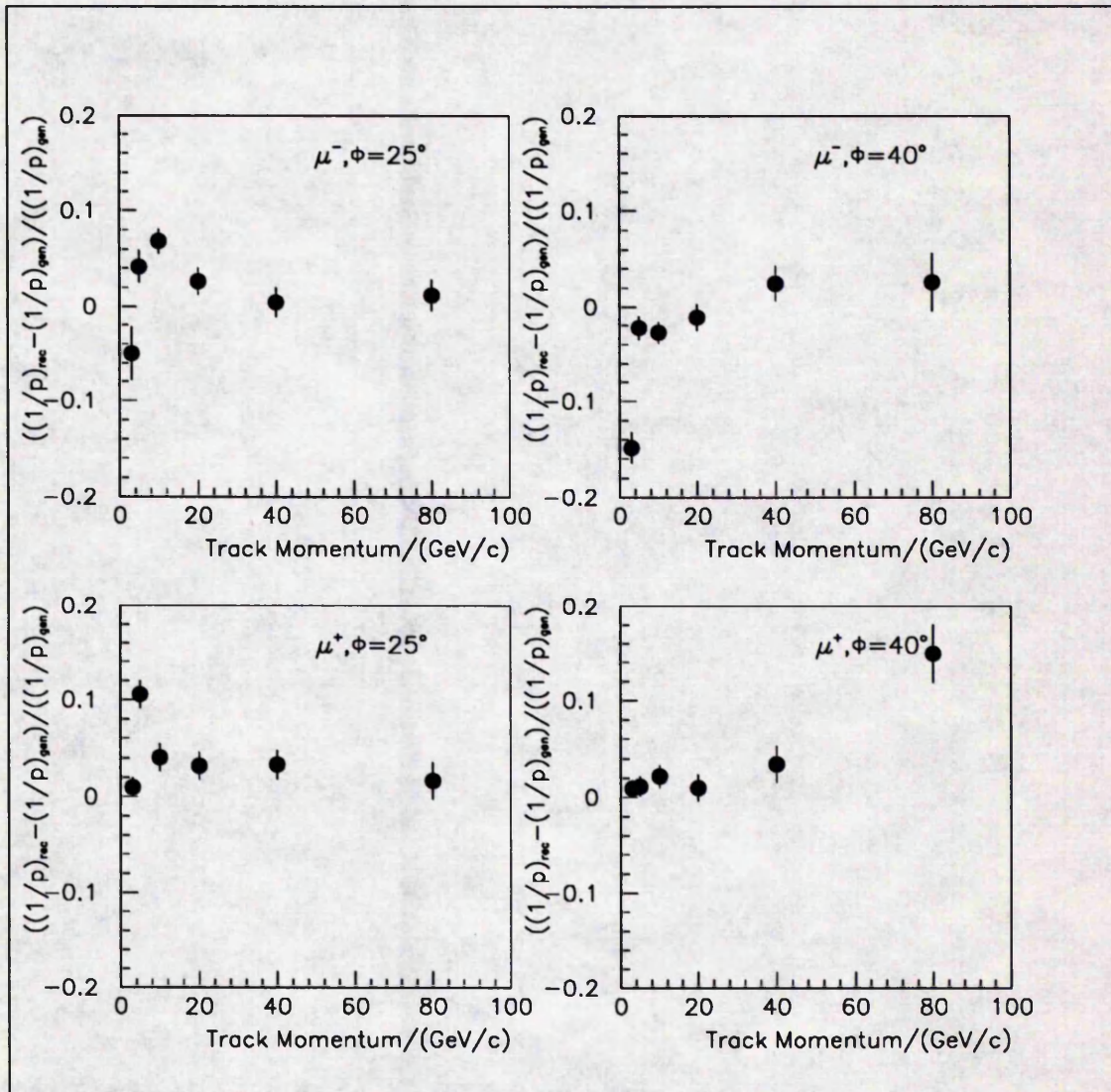


Figure 3.7: Systematic shift in the reconstructed inverse track momentum for the FMD,  $((1/p)_{rec} - (1/p)_{gen}) / ((1/p)_{gen})$ .

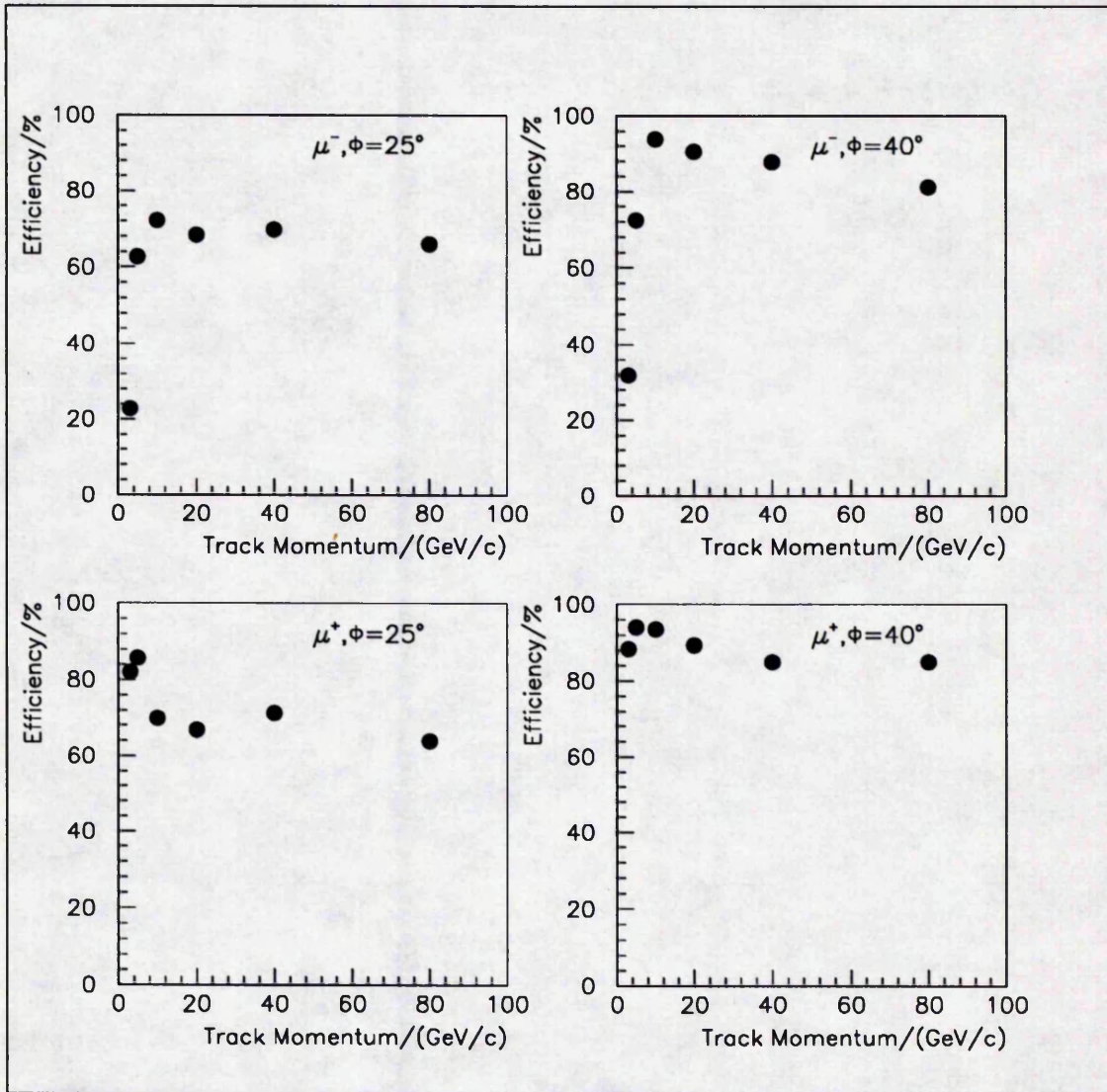


Figure 3.8: Efficiency of forward muon detector reconstruction.

3.1 and 3.2, the following expression for the momentum of the FMD is obtained:

$$\frac{\sigma_{1/p}}{1/p} = 0.26 \quad (3.3)$$

The spatial resolution of the drift chambers leads to an additional contribution to equation 3.3 which becomes increasingly important as the track momentum increases. In the case of the simulation done here, where phi chambers have not been included, this additional contribution is determined mainly by the spatial resolution of the coordinate along sense wire obtained by charge division. As can be seen from figure 3.6, this contribution becomes significant at only a few tens of GeV/c, especially for tracks which pass through the theta octants at large phi angles relative to the central axis of a theta octant. Inclusion of the phi layers will effectively remove dependence on the charge division measurements. The spatial resolution contribution to the momentum resolution will then be determined mainly by the drift time resolution. This increases the muon track momentum at which spatial resolution becomes significant, the spatial resolution contributing only 10% of the momentum resolution for a 100 GeV/c muon track.

The systematic shift in reconstructed inverse momenta are consistent with zero, except for low momenta track with  $\phi = 25^\circ$  where the approximate nature of the extrapolation of the tracks through the toroid in the reconstruction code produces a significant systematic shift. To reduce this systematic shift, the number of steps in the extrapolation through the toroid was increased here from three to ten. The efficiency of reconstructing a track is typically 90% for tracks with  $\phi = 40^\circ$  and 70% for tracks with  $\phi = 25^\circ$ ; the difference results from the  $\phi = 25^\circ$  tracks in the range  $\theta = 6^\circ \rightarrow 10^\circ$  passing through the gap between two cells and consequently being consistently misreconstructed. For the negatively charged muon tracks the efficiency of reconstruction drops at low momenta. This is due to the reconstruction code being unable to reconstruct tracks which are bent inwards by the magnetic field of the iron toroid by an angle in  $\theta$  greater than the initial  $\theta$  angle of the track.

# Chapter 4

## The Drift Chambers

### 4.1 Operation of Drift Chambers

The operation of a drift cell is discussed in detail in [24]. A single sense wire drift cell consists of a gas-filled chamber over which is placed a moderate electric field. In the centre of the cell is a fine anode sense wire surrounded by a strong electric field. When an incoming charged particle passes through the gas of the drift chamber, a discrete number of primary ionizing collisions occur which liberate electron-ion pairs. The electrons ejected can have enough energy to produce secondary pairs, resulting in the formation of ionisation clusters along the incoming particle's track. These clusters of electrons drift along the moderate electric field, towards the anode sense wire. In the strong electric field around the sense wire, the probability of a drifting electron gaining enough energy between impacts to ionize atoms on collision becomes sufficient to produce an exponential increase in the number of ion pairs. Due to lateral diffusion, a drop-like avalanche develops which surrounds the wire. Such avalanche multiplication can produce gains typically of the order of  $10^5$ .

The detected signal is the result of the change in the energy of the system due to the movement of the electrons and the positive ions toward and away from the anode respectively. The majority of the electrons in the avalanche are produced very close to the anode (half of them in the last mean free path of an electron between

ionising collisions). Thus, electrons only have to drift a small distance compared to the positive ions which have to drift across the whole drift chamber. This results in the positive ions generating the majority of the detected signal. The positive ions produce no further ionization as their greater mass prevents them from gaining enough energy between impacts to produce ionisation.

As avalanche multiplication occurs in noble gases at much lower fields than in gases of complex molecules (this is a consequence of the many non-ionising dissipation modes available in polyatomic molecules), noble gases are usually used as the main component of the gas mixture which is used to fill drift chambers. However, gains in excess of  $10^3$  to  $10^4$  can not be obtained without entering into the permanent discharge mode of the drift chamber. Permanent discharge results from photons or argon ions, produced in the avalanche, releasing electrons from the drift field forming wires which lead to further avalanches. The addition of a polyatomic gas, quenching agent, is used to allow improved gains of order  $10^5$ . The polyatomic molecules absorb the photons and undergo ion exchange with the argon ions and are excited to a non-radiative/non-ionizing state which produces no further photons or electrons; the energy of the excited polyatomic molecules is dissipated either by elastic collisions or by dissociation into simpler radicals. The quenching agent concentration falls as a result of the production of simpler radicals which recombine to form simpler molecules (dissociation) or larger molecules (polymerization). Thus, the gas mixture is allowed to flow through the drift chambers in order to maintain the concentration of quenching agent and to remove the impurities produced from the quenching agent.

From the drift time of the electron and a knowledge of the space-time relationship the position of the track, with respect to the anode wire, may be deduced. By comparing the charges contained in the pulses at the two ends of the sense wire, it is possible to obtain an approximate coordinate along the sense wire. This is achieved using the idea of charge division in which the charge is considered to be divided between the two ends of the sense wire in a ratio inversely proportional to the resistance of the wire along which the pulse has travelled.

## 4.2 Determination of the Space-Time Relationship

To determine the drift distance from the drift time, the space-time relationship must be known:

$$x = f(t - t_0)$$

where  $x$  is the drift distance,  $t$  is the measured drift time and  $t_0$ , referred to as t-zero, is the measured drift time corresponding to  $x = 0$ . Obviously, it is convenient to have a linear space-time relationship which is obtained by having a uniform drift electric field. By operating the drift chamber as close to the plateau in the drift velocity-electric field relation as possible, the uniformity of the electric field is made less critical. Initially, for this reason, a gas mixture of 90% argon and 10% propane with its broad plateau, figure 4.1, was used in the forward muon drift chambers. However, this gas mixture is flammable and for safety reasons, it was decided to replace it by the present non-flammable 92.5% argon, 5% CO<sub>2</sub> and 2.5% CH<sub>4</sub> gas mixture. This gas mixture has a faster drift velocity, as required by the forward muon trigger, but also leads to an increased drift distance resolution. For the new gas mixture, the plateau in the drift velocity - electric field relation is narrower, figure 4.2, leading to a less uniform drift velocity over the drift space. Thus, it was necessary to determine reasonably accurately the plateau in the drift velocity-electric field relation for the new gas and to investigate the behaviour of the drift velocity over the drift space. The details of the study made can be found in reference [25].

The experimental set up used is shown in figure 4.3. The drift chambers are numbered 0 to 7 going from top to bottom. The set up is designed to provide a uniform illumination of horizontal cosmic tracks across the whole of the drift space of the drift chambers. The resulting time distribution is expected to be 'top hat' provided the acceptance (efficiency) and the drift velocity are uniform across the cell. It is very difficult to disentangle these two contributions to the non-uniformity of the time distribution, however, the global efficiency of a cell is easily found. The

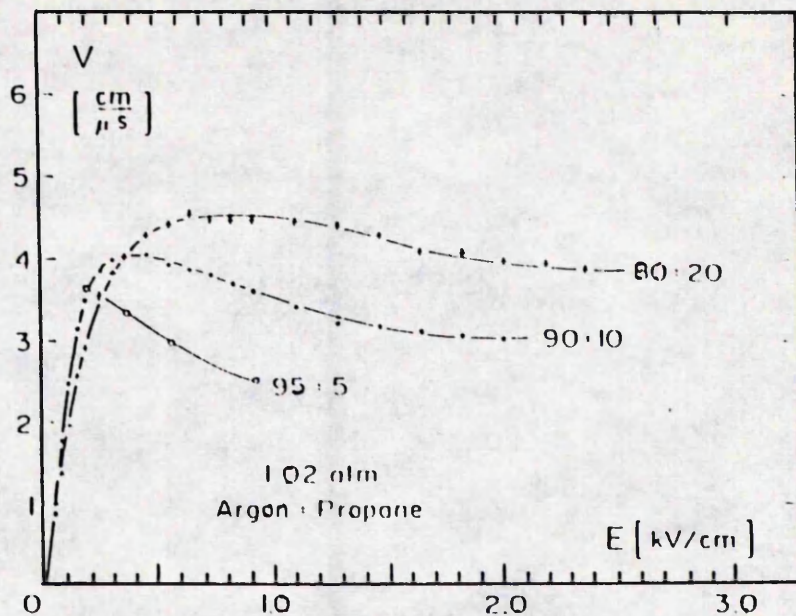


Figure 4.1: Graph of the drift velocity against electric field for various argon/propane mixtures.

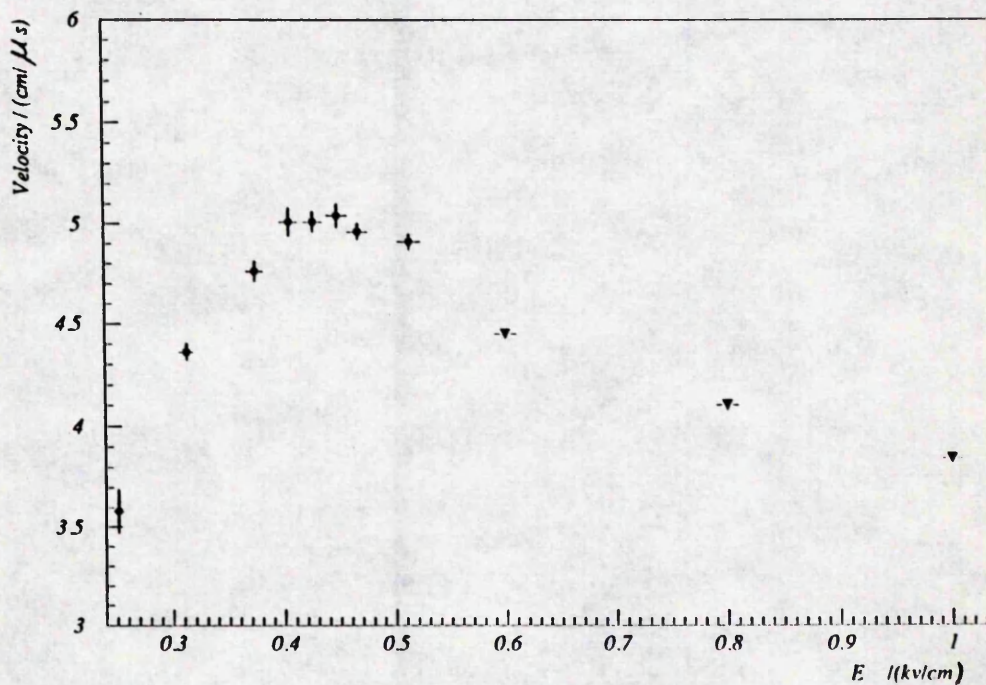


Figure 4.2: Graph of the drift velocity against electric field for the present 92.5% argon, 5.0%  $CO_2$  and 2.5%  $CH_4$  gas mixture.

global efficiency is given by:

$$Efficiency = \frac{N_{TOTAL} - N_{NOHIT}}{N_{TOTAL}} \times 100\%$$

where  $N_{TOTAL}$  is the number of events with a hit in cell 5 and 7 and  $N_{NOHIT}$  is the number of these events which do not have a hit in cell 6. The global efficiency is found to be greater than 97%. Thus, even if the chamber efficiency was not uniform over the drift space, it could not account for the deviation of the drift time distribution obtained, from a top hat. The space-time relation is obtained from the time distribution using:

$$x_p = \frac{\Delta x}{N} \sum_{i=0}^p n_i$$

where  $x_p$  is the distance corresponding to the  $p^{th}$  time bin and  $n_i$  is the number of hits in the  $p^{th}$  time bin,  $\Delta x$  is the total drift distance and  $N$  is the total number of events.

The results obtained for two electric fields are shown in figure 4.4 and 4.5 where the mean electric field,  $\bar{E}$ , is defined as the total voltage across the drift space divided by the total length of the drift space. The behaviour of these curves can be explained with the aid of the drift velocity curve, figure 4.2. A mean field,  $\bar{E} = 0.26 \text{ kV cm}^{-1}$ , is significantly below the plateau in the drift velocity-electric field curve and, hence, in the regions at low and high  $x$  where the field varies substantially from its uniform central  $x$  value, the drift velocity varies substantially, correspondingly. By moving the mean field on to the plateau,  $\bar{E} = 0.45 \text{ kV cm}^{-1}$ , the effect of variation in the electric field is reduced and the drift velocity is kept constant over a larger region of the drift space, substantial variation being limited to the region near the wire.

### 4.3 Electrostatic Modelling of the Drift Cells

To understand the space-time relation of the chambers fully, the electrostatics of the chambers must be understood. Electrostatic modelling was carried

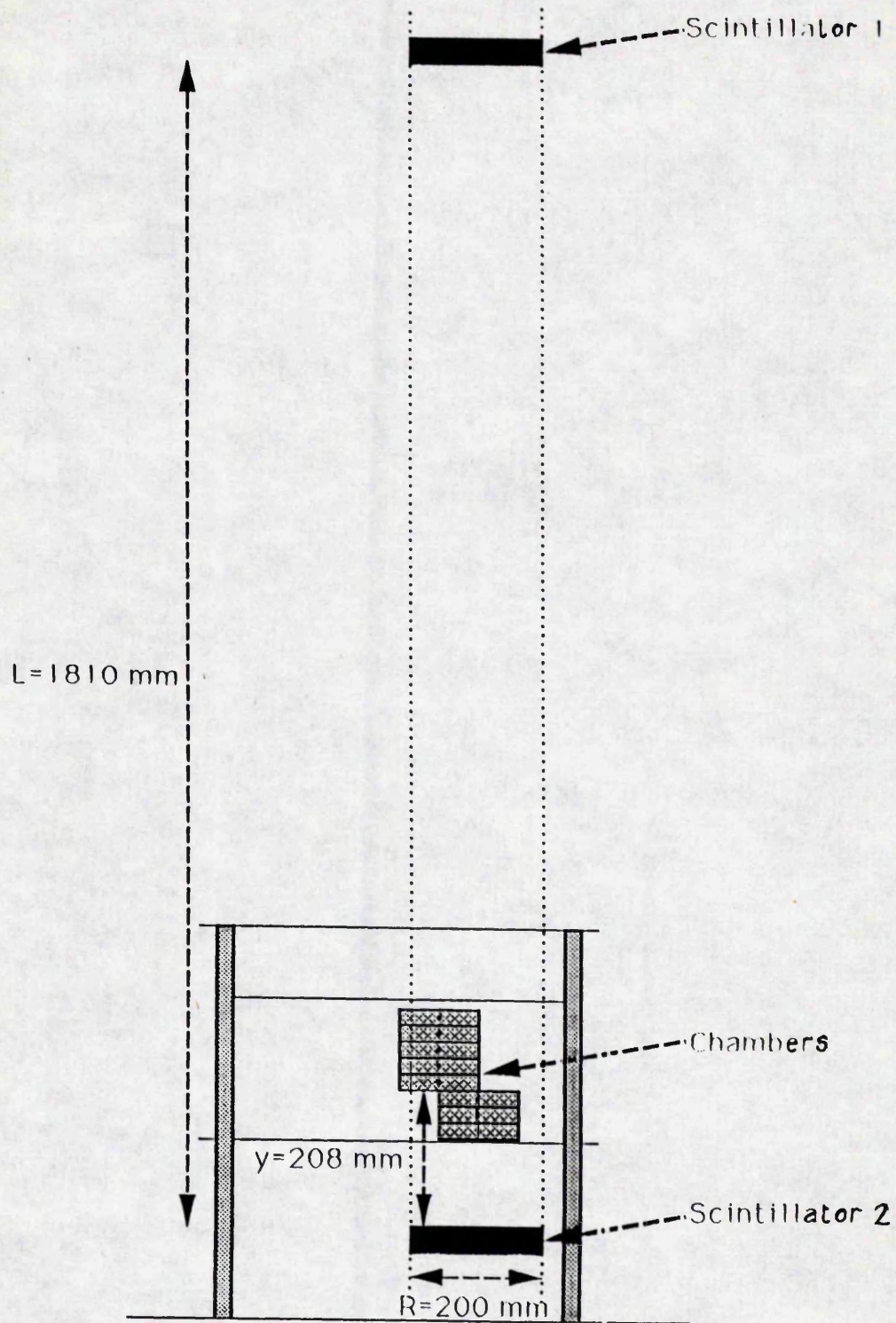


Figure 4.3: Scale diagram of stack, set up for uniform illumination of the lower three cells.

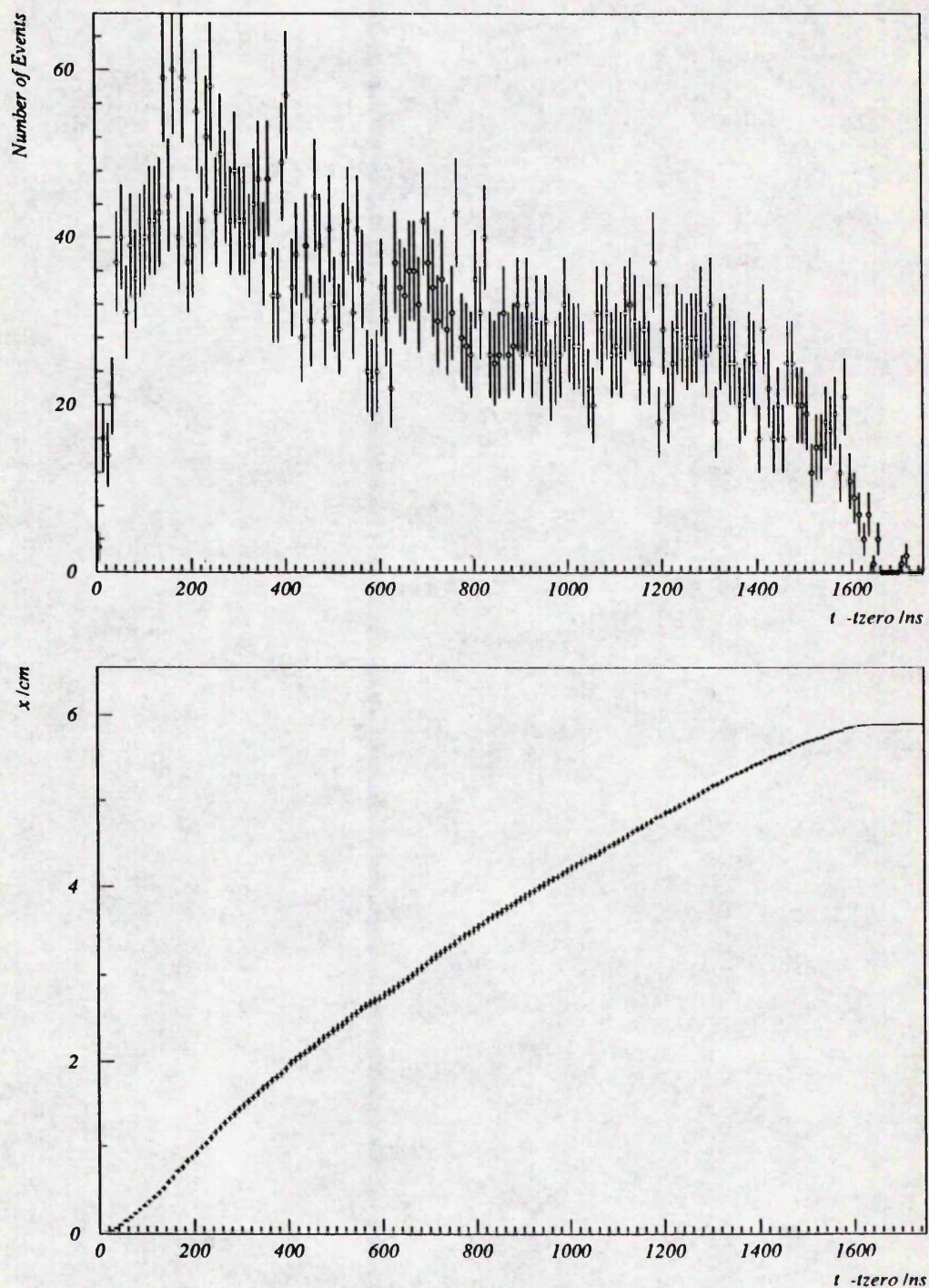


Figure 4.4: Time distribution (top) and integrated time distribution (bottom) for mean electric field  $\bar{E} = 0.26 \text{ kV cm}^{-1}$ .

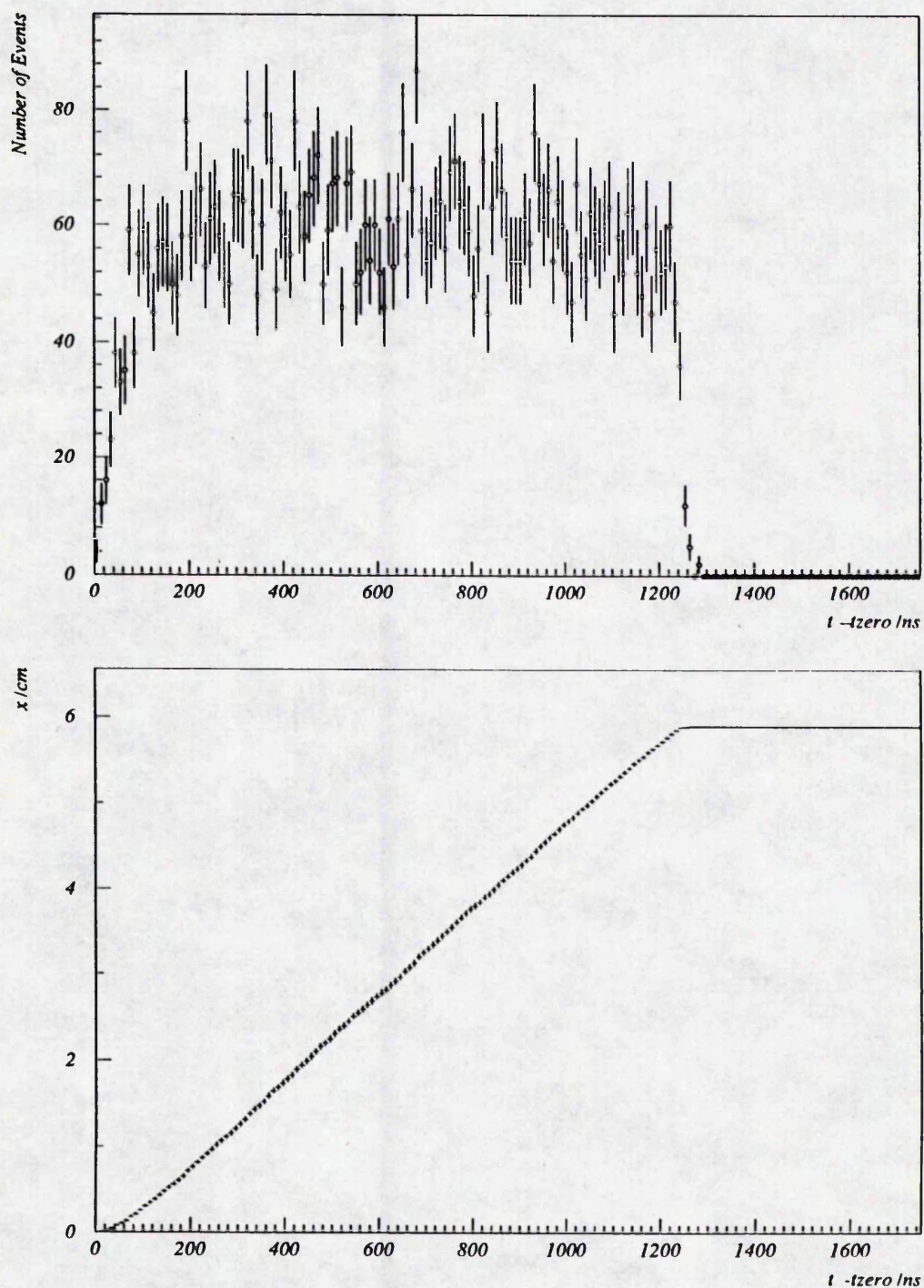


Figure 4.5: Time distribution (top) and integrated time distribution (bottom) for mean electric field  $\bar{E} = 0.45 \text{ kV cm}^{-1}$ .

out by [26] during the development of the FMD drift chambers and later by [25]. The latter electrostatic modelling was done using a substantially modified version of MOPAL, the program used to model the OPAL barrel muon chambers [27]. In this program, a quarter of a drift chamber is depicted by a square lattice of points, with a separation of 0.1 mm. This lattice is separated further into two diamond sublattices, displaced by 0.1 mm. The known voltages (those on the copper strips, those on the chamber walls and those in the region surrounding the wire) are assigned to their respective lattice points and kept constant throughout. All other points start out at zero. Each point in the second sublattice is assigned the mean of the four points directly surrounding it from the first sublattice. The two lattices now swap roles, with the first lattice assigned the value of the mean of the surrounding points from the second. This process is repeated until the point values relax to their final values. The results for a mean field,  $\bar{E} = 0.43 \text{ kV cm}^{-1}$  are shown in figures 4.6 and 4.7. Graph 4.8 shows the electric field obtained by differentiating the modelled voltages for a mean field,  $\bar{E} = 0.45 \text{ kV cm}^{-1}$ , along the  $y = 0$  plane. As previously mentioned there is a region of non-uniform field at low  $x$  ( $< 2 \text{ cm}$ ) and at high  $x$  ( $> 4.5 \text{ cm}$ ).

It was found from electrostatic modelling that there is a small but significant difference between two chambers with exactly the same nominal electric field setting, but different wire radii ( $20 \text{ }\mu\text{m}$  and  $25 \text{ }\mu\text{m}$ ). The result is shown in figure 4.9. The difference in electric field is  $0.05 \text{ kV cm}^{-1}$  over much of the cell and up to  $0.45 \text{ kV cm}^{-1}$  near the wire. From the drift velocity-electric field curve, it can be seen that this corresponds to a significant difference in the space-time relation between the two wire radii. By comparing the measured space-time relations for the two wire diameters, the difference in  $x$  was found to vary by up to 1 mm near the wire.

#### 4.4 Determination of Drift Velocity and T-zero

For an electric field of  $0.45 \text{ kV cm}^{-1}$ , the space-time relation can be repre-

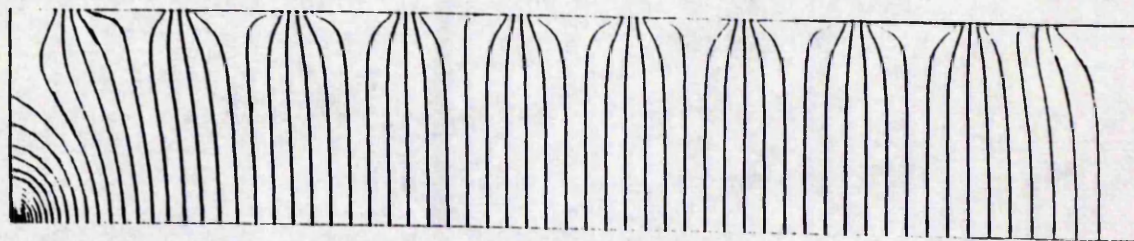


Figure 4.6: Cross-section through quarter cell, showing equipotential for mean field  $\bar{E}$  of  $0.43 \text{ kV cm}^{-1}$ .

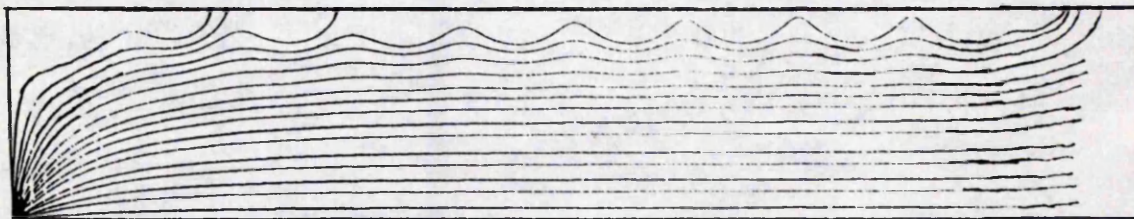


Figure 4.7: Cross-section through quarter cell, showing the electric field lines for mean field  $\bar{E}$  of  $0.43 \text{ kV cm}^{-1}$ .

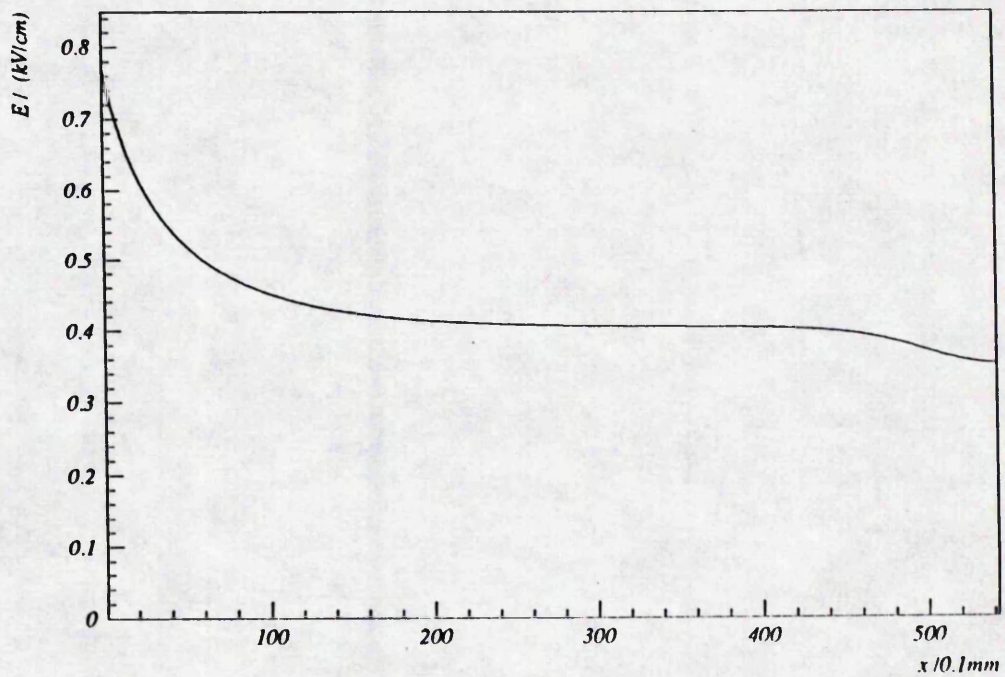
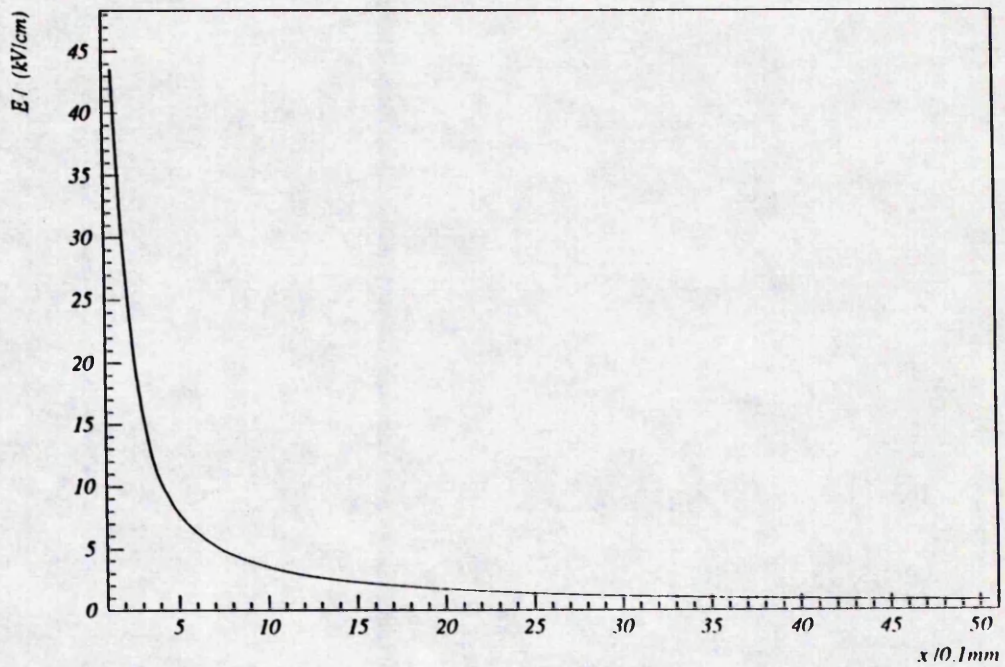


Figure 4.8: Graph of electric field versus  $x$  for  $x < 0.5\text{cm}$  (top) and  $x > 0.5\text{cm}$  (bottom) for a mean field  $\bar{E}$  of  $0.45\text{ kV cm}^{-1}$  along  $y = 0$ .

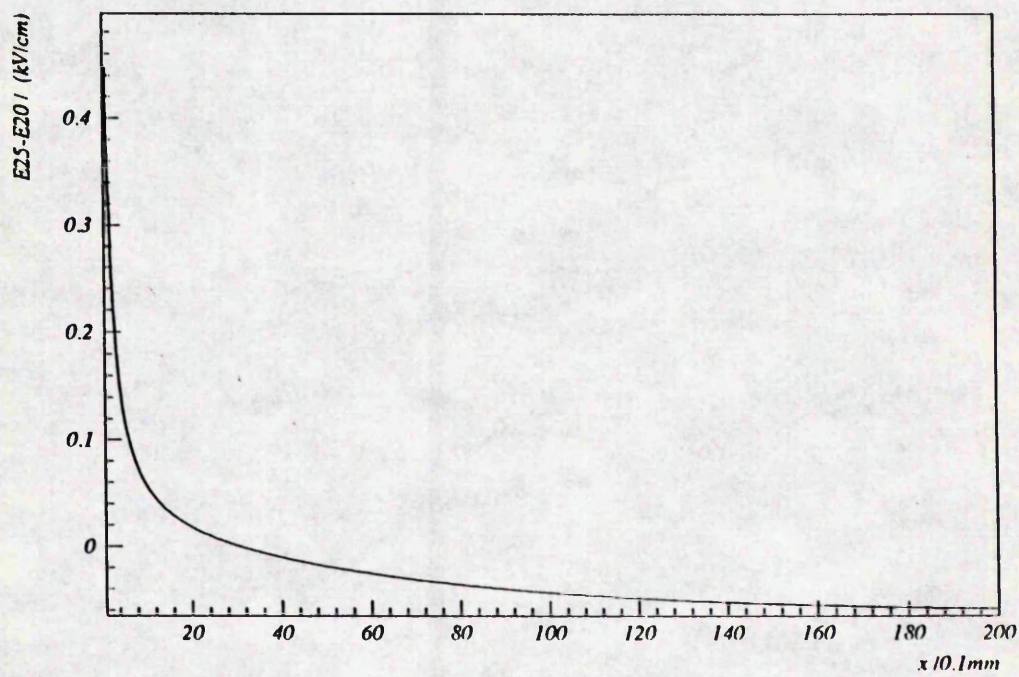


Figure 4.9: Graph showing the difference between the electric field of two chambers with the two different wire radii.

sented for most of the drift distance by the linear expression:

$$x = v \times (t - t_0)$$

where  $x$  is the drift distance,  $t$  is the drift time,  $t_0$  is t-zero and  $v$  is the drift velocity of the gas, which is considered to be constant in this expression. Variation of t-zero between cells is obtained from test pulse runs and by calculating the time of flight difference between the different theta layers in the FMD. When these are taken into account, this leaves only a global t-zero to be determined. Muon tracks which pass through the FMD, as for example those provided by beam halo, are used to determine the global t-zero and drift velocity [28].

For uniform illumination, efficiency and drift velocity over the full drift distance, a top hat drift time distribution is expected. However, due to large electric field variations at large and small drift distances, the effect of angled tracks and finite drift time resolution, the drift time distribution obtained, shown in figure 4.10, is smeared at the edges. In spite of this, the drift time,  $t_{mid}$ , corresponding to half the drift distance (3cm) can be obtained by finding the time which has equal number of tracks above and below. The value of  $t_{mid}$  obtained is  $823 \pm 2$  ns. By taking an arbitrary time interval,  $\Delta t$ , symmetrically around  $t_{mid}$  where the distribution is still flat and counting the number of tracks,  $N_{mid}$ , in this interval, the drift velocity can be determined from the following expression:

$$v = \frac{\Delta x \cdot N_{mid}}{\Delta t \cdot N}$$

where  $\Delta x$  is the full drift distance and  $N$  is the total number of tracks in the drift time distribution. The drift velocity obtained is  $v = 4.93 \pm 0.04$  cm  $\mu s^{-1}$ .

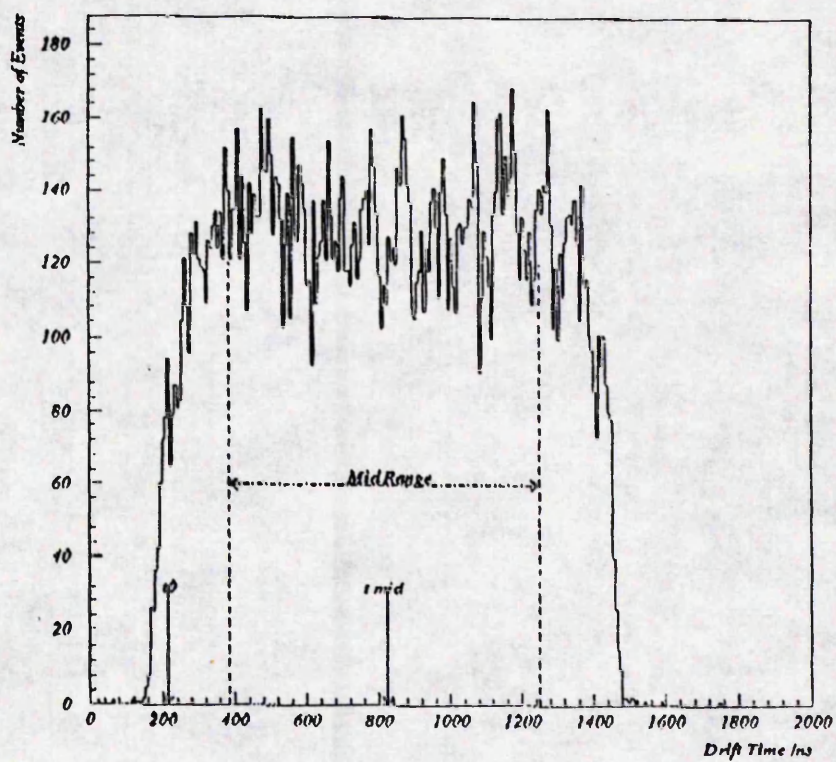
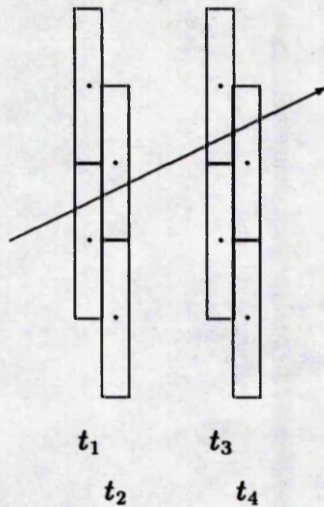


Figure 4.10: The drift time distribution for the drift cells of the FMD.

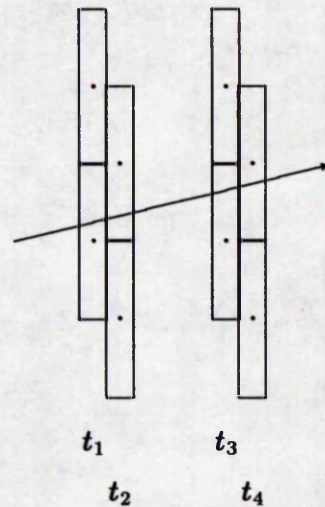
Depending on the specific geometry of the drift cells, one of two checksums can be used:

## The First Checksum



$$t_1 + t_2 + t_3 + t_4 = 4.t_{mid}$$

## The Second Checksum



$$t_1 + t_2 - t_3 - t_4 = 0$$

where  $t_1, t_2, t_3$  and  $t_4$  are the drift times for the two pairs of drift cells in the two theta layers on one of the sides of the toroid. The checksum distributions obtained are shown in figures 4.11 and 4.12. The first checksum provides an independent and more accurate measurement of  $t_{mid}$ . The value of  $t_{mid}$  obtained is  $824.7 \pm 0.1$  ns. The width of the two checksum distributions can be used to find the spatial resolution of the chambers. Using the second checksum distribution, the value  $310 \pm 5 \mu\text{m}$  is obtained for the spatial resolution. T-zero can be determined from  $t_{mid}$  using the following expression:

$$t_0 = \frac{3cm}{v} - t_{mid}$$

The value for t-zero corresponding to the value of  $t_{mid}$  obtained using the first checksum is  $216 \pm 5$  ns.

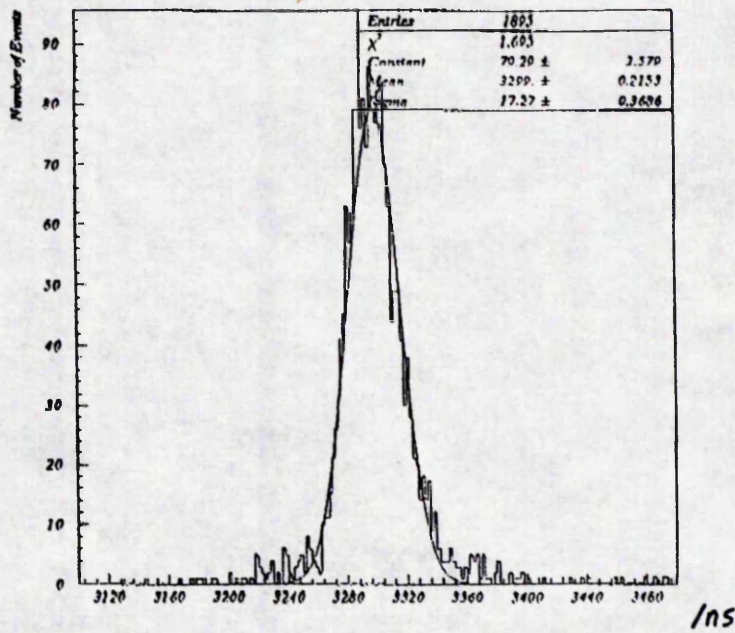


Figure 4.11: The first checksum distribution.

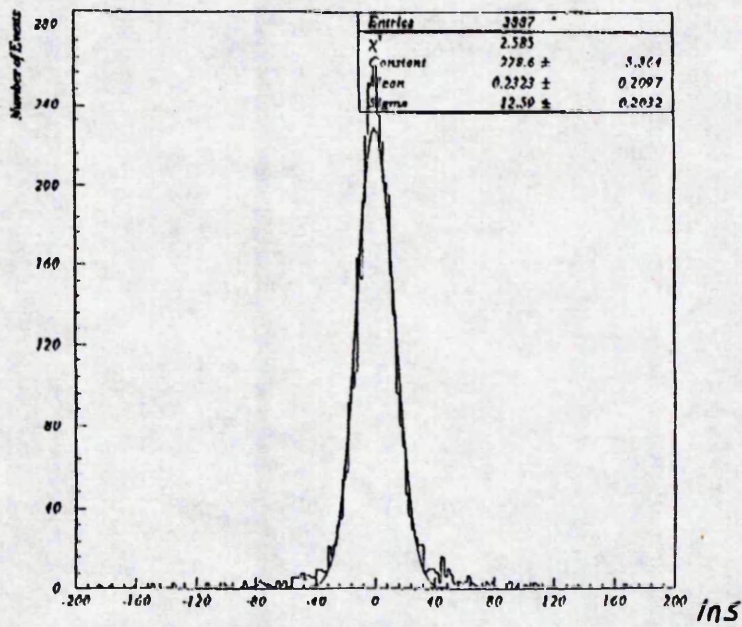


Figure 4.12: The second checksum distribution.

## 4.5 Determination of the Drift Time from Raw Pulse Data

Drift cells provide the position coordinate perpendicular to the sense wire most accurately. The drift time is obtained from the drift cell pulses using the algorithm illustrated in figure 4.13, called the 'leading edge' algorithm. The resulting drift time corresponds to the time at which the first electron arrived. For the front edge of a pulse, the maximum difference of samples is measured, MAXDOS, and located, IMAXDOS. A line with slope  $\text{MAXDOS}^{-1}$  is extrapolated from IMAXDOS back to the background level, LBASE. The time corresponding to a point a fraction,  $K$ , along this line, is taken as the drift time. The fraction  $K$  used is  $1/3$ . The background level is taken to be the average bin content just before the start of the pulse [29].

The resolution of the drift distance is composed of four main contributions [24, 30]:

- Diffusion of the electrons as they drift towards the sense wire leads to a contribution,  $\sigma_{diff}$ , which varies as the square root of the drift distance. A simple expression can be derived, estimating the value of  $\sigma_{diff}$  for the case of drift times corresponding to the arrival time of the first primary electron cluster:

$$\sigma_{diff} = \frac{\pi}{2} \sqrt{\frac{2kT}{3eE \ln(n)}} \sqrt{x} \quad (4.1)$$

where  $k$  is Boltzmann's constant,  $T$  is temperature,  $E$  is the drift electric field,  $n$  is the number of primary electron clusters and  $x$  is the drift distance.

- There is a further constant contribution,  $\sigma_{elec}$ , which results from the finite bin width of the FADCs and which is given by equation:

$$\sigma_{elec} = \frac{vt_{bw}}{\sqrt{12}} \quad (4.2)$$

where  $v$  is the drift velocity of the electrons and  $t_{bw}$  is the FADC bin width.

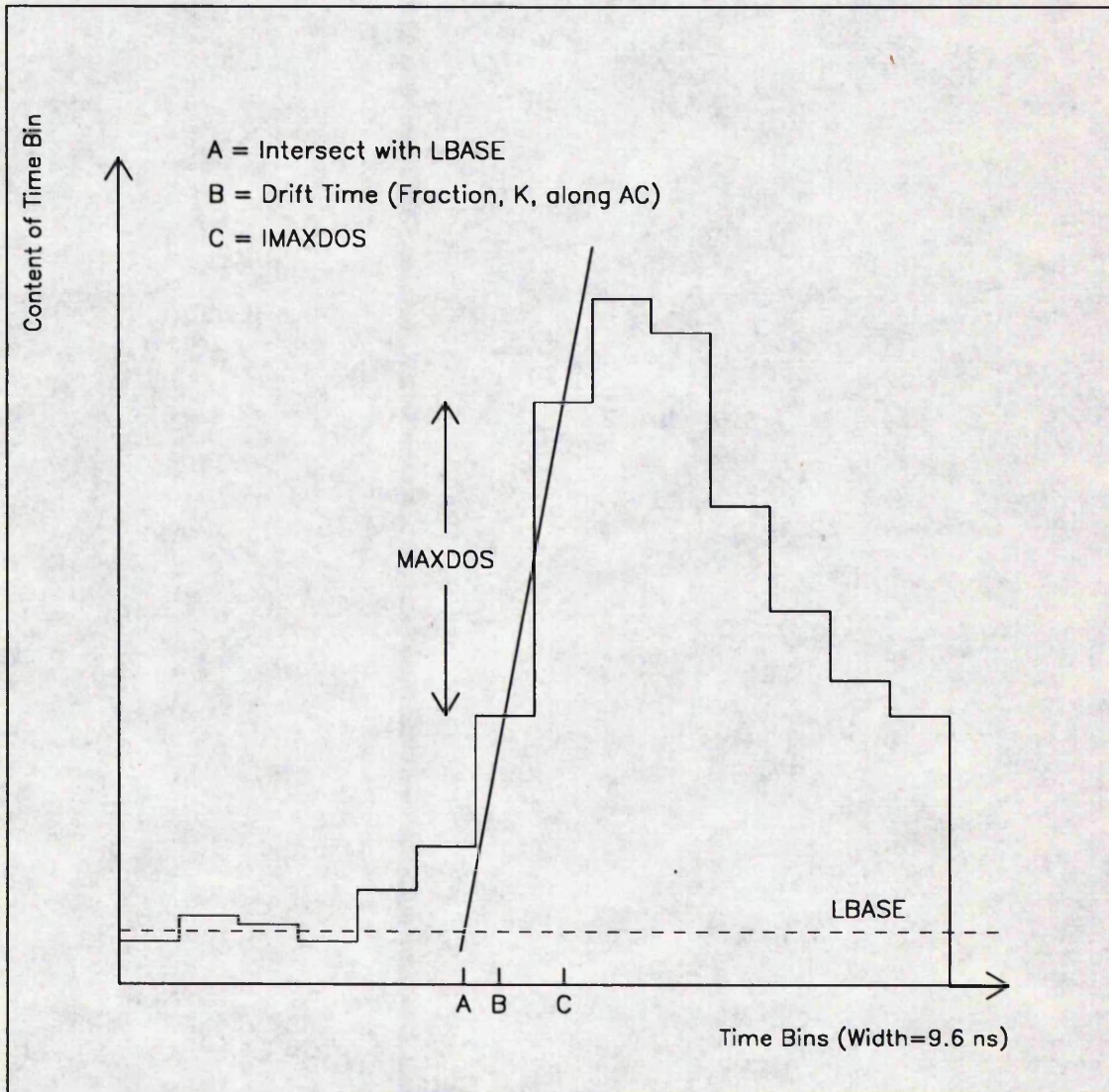


Figure 4.13: The leading edge algorithm for finding the drift time from the raw pulse data.

The final two contributions are a consequence of the non-uniformity of the drift field, which results in a variation in drift path length for primary ionisation clusters produced at different points along the particle track as it traverses the cell, and in a variation in drift velocity along the drift paths.

- Statistical fluctuations in the size and position of the primary ionisation clusters along the particle's track result in a contribution,  $\sigma_{clust}$ . For drift times obtained from the arrival time of the first primary electron cluster, this contribution to the drift distance resolution is only significant close to the sense wire.
- There is a systematic contribution due to the inaccuracy to which the drift velocity and its variation over the drift space and  $t$ -zero are known.

The individual contributions to the  $x$ -resolution are summed in quadrature to give the resultant  $x$ -resolution,  $\sigma_{tot}$ .

The variation of the drift distance resolution with drift distance obtained from studies with the previous argon/propane gas mixture is shown in figure 4.14. The final two contributions to the drift distance resolution are not significant over the drift range shown in figure 4.14 for the gas used. Thus, the function:

$$\sigma_{tot} = \sqrt{\sigma_a^2 x + \sigma_b^2}$$

was fitted to the first four points in the curve. The value  $68 \pm 3 \mu\text{m cm}^{-\frac{1}{2}}$  was obtained for  $\sigma_a$ . This can be identified with the equation 4.1 which predicts a value for  $\sigma_a$  of  $37 \mu\text{m cm}^{-\frac{1}{2}}$  where  $T$  was taken to be 300 K,  $n$  to be 100 and  $E$  to be  $0.67 \text{ kV cm}^{-1}$ . The fitted value for  $\sigma_b$  was  $139 \pm 4 \mu\text{m}$ . This corresponds to  $\sigma_{elec}$  given by equation 4.2 which predicts a value of  $112 \mu\text{m}$ , where the drift velocity was taken to be  $4 \text{ cm } \mu\text{m}^{-1}$  and  $t_{bw}$  to be 10 ns. Thus, these results are in broad approximate agreement with the theory.

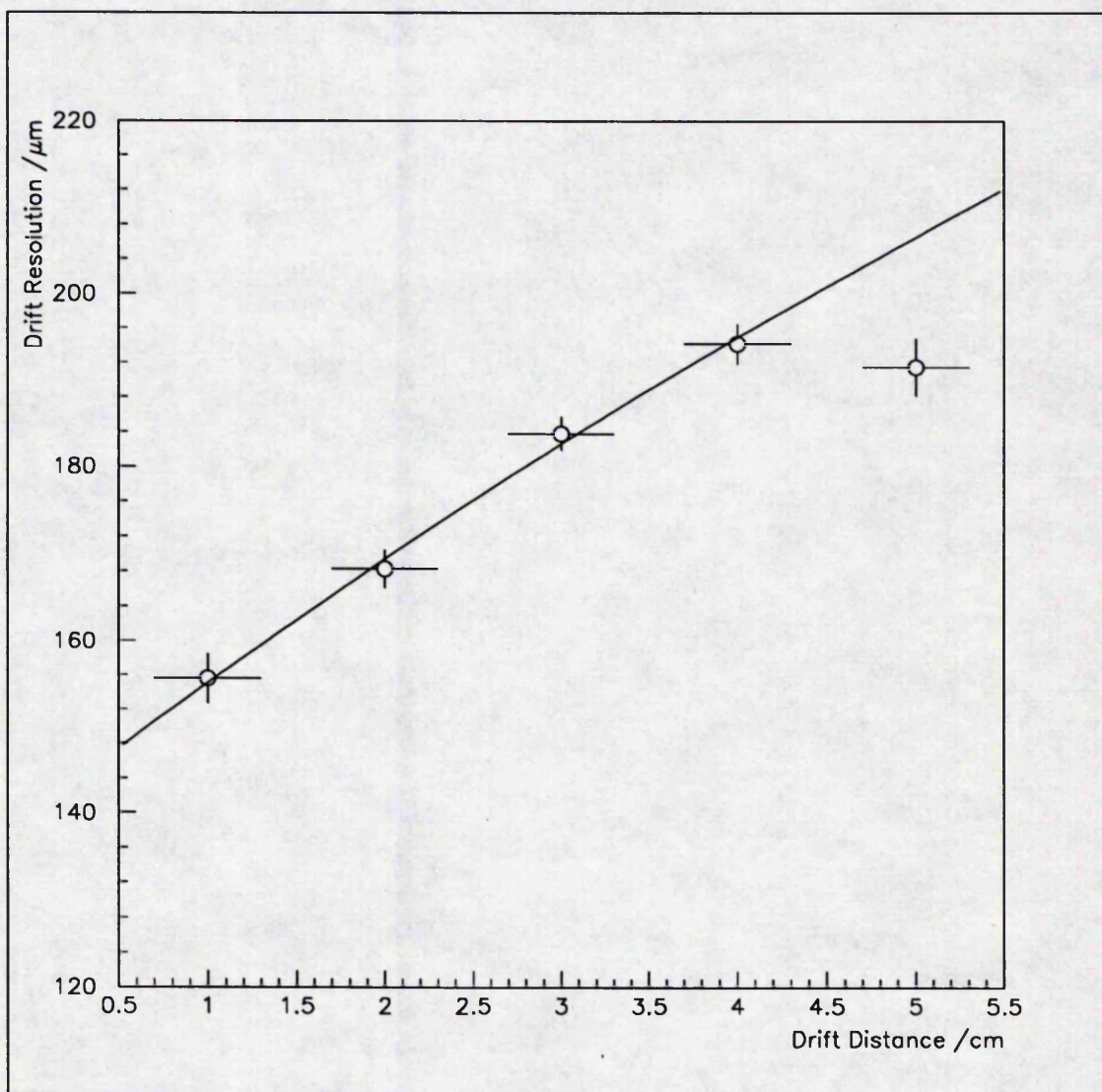
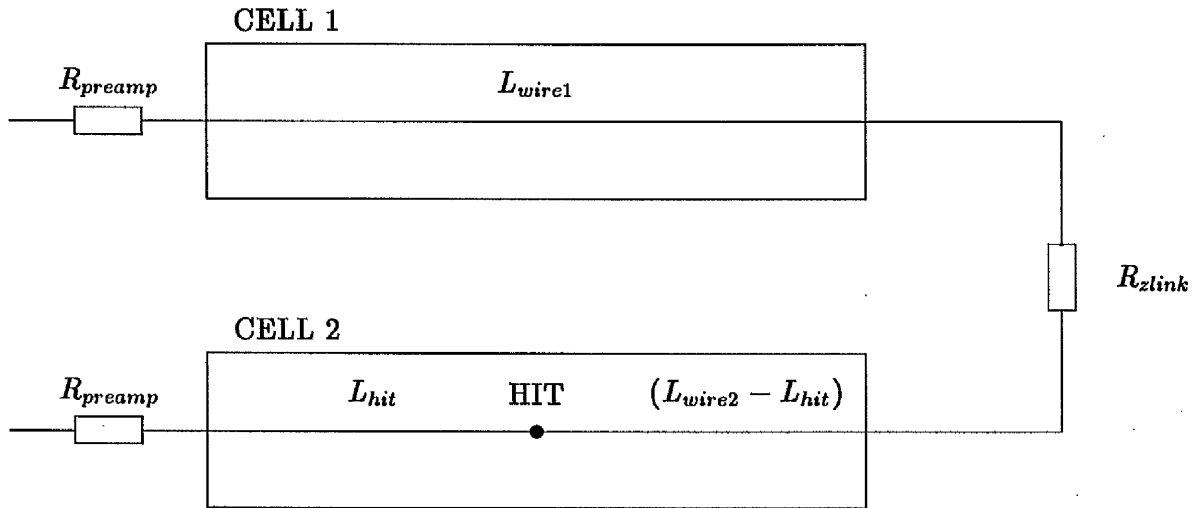


Figure 4.14: Drift distance resolution against drift distance for the previous argon/propane gas mixture.

## 4.6 Charge Division

The charge division method for determining the coordinate of the hit along the sense wire is based on the idea that the charge is divided between the two ends of the sense wire in a ratio inversely proportional to the resistance of the wire along which the pulse has travelled.



$$\frac{Q_{wire1}}{Q_{wire2}} = \frac{R_{preamp} + \rho L_{wire1} + R_{zlink} + \rho(L_{wire2} - L_{hit})}{R_{preamp} + \rho L_{hit}} \quad (4.3)$$

This simplistic idea of charge division is, in fact, false. The pulse is generated at the hit coordinate along the sense wire and identical pulses travel in opposite directions away from this point down the sense wire which can be considered to act as a dispersive transmission line. So, in reality, the pulses arriving at the two ends of the sense wire contain the same charge, but are dispersed, the extent of which depending on the distance along the sense wire that the pulse has travelled. However, by optimizing the algorithm for calculating  $q$ , the charge division equation above, 4.3, can be made to work.

The algorithm [29] used by the forward muon chambers obtains  $q$  by integrating the charge in a pulse over a fixed number of channels. Eight channels are summed over, unless one or both the pulses are less than eight channels long in

which case the number of channels of the shorter pulse is used. A correction is then made to shift the integral so that it starts at the drift time obtained for the pulse, instead of the start of the first channel in the hit pulse. Finally, the integral over the background level, LBASE, is removed.

A detailed study of the measurement of the hit coordinate along the sense wire (referred to here as the  $z$ -coordinate) using charge division was done by [31] in which the above algorithm was developed. The new algorithm was compared to the original algorithm in which the  $q$  is obtained by summing the contents of the channels from the first channel of the pulse to two after the peak of the pulse. The study was done with two cells, each 1350 mm long, linked by a  $z$ -link of  $330 \Omega$  which is equivalent to about 600 mm of sense wire. Figure 4.15 shows the distribution of measured coordinate along the sense wire,  $z_{meas}$ , for events triggered in the range 870-910 mm from the  $z$ -link, comparing the old and new algorithms. As can be seen the new algorithm produces a more Gaussian distribution with fewer anomalous events. Figure 4.16 shows a comparison between the old and new algorithms of the variation of the resolution of the measured coordinate along the sense wire against the distance along the sense wire. The new algorithm gives an improved resolution (particularly near to the readout end of a cell) which is uniform over the length of the cell. The resolution obtained using the new method is about 34 mm which corresponds to a resolution of 1% of the total effective length for the system of 3300 mm. It is assumed that a resolution of 1% is the case for all linked cell lengths, independent of operating conditions. Figure 4.17 shows the linear relationship between the measured and actual coordinates along the sense wire obtained with the new algorithm. The fraction of events for which the hit was identified to be in the wrong cell of the linked pair was measured to be 2.6%. This is probably a pessimistic value, as some of these tracks may actually have gone through the wrong cell.

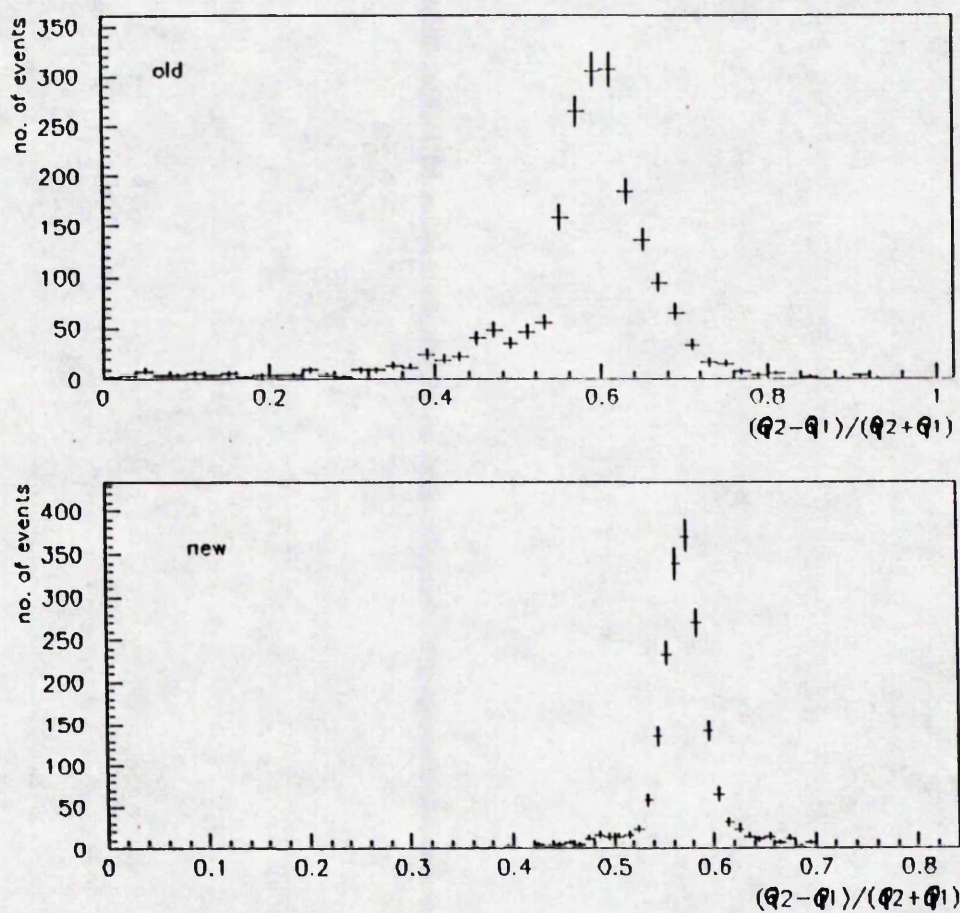


Figure 4.15:  $z_{meas}$  distributions for events triggered in the range 870-910 mm from the z-link, for the old and new algorithms.

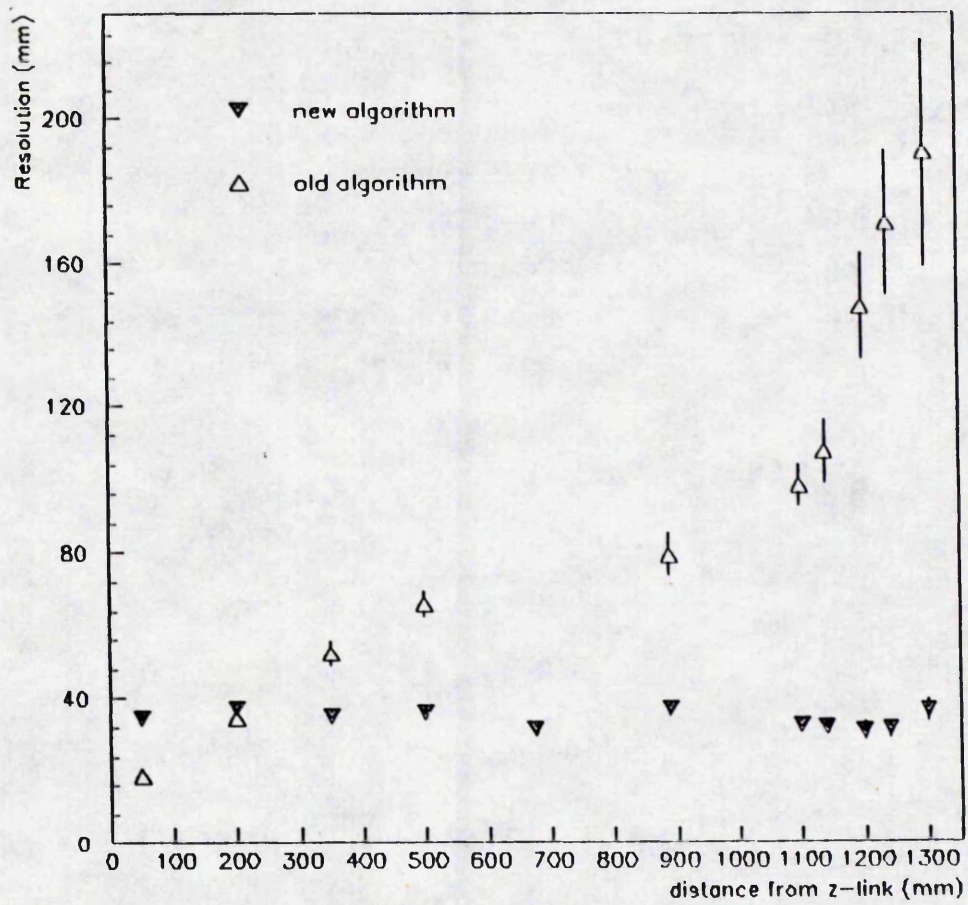


Figure 4.16: Comparison of the variation of the z-resolution with z between the old and new algorithms.

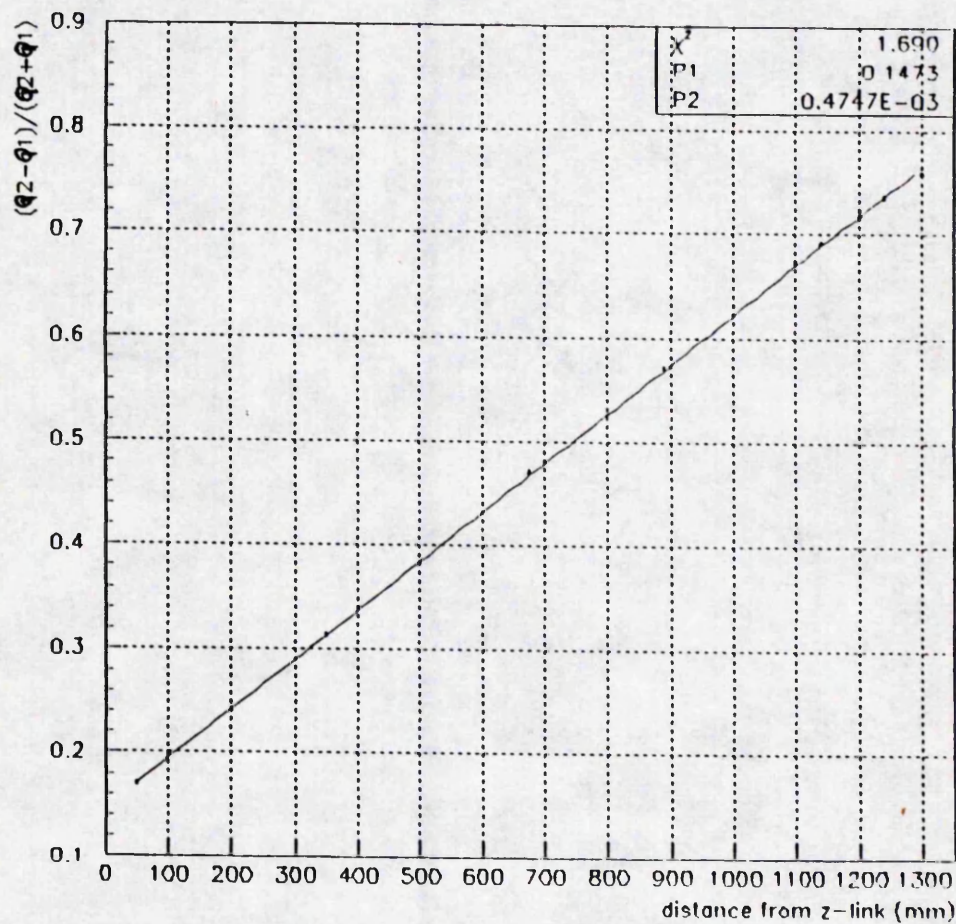


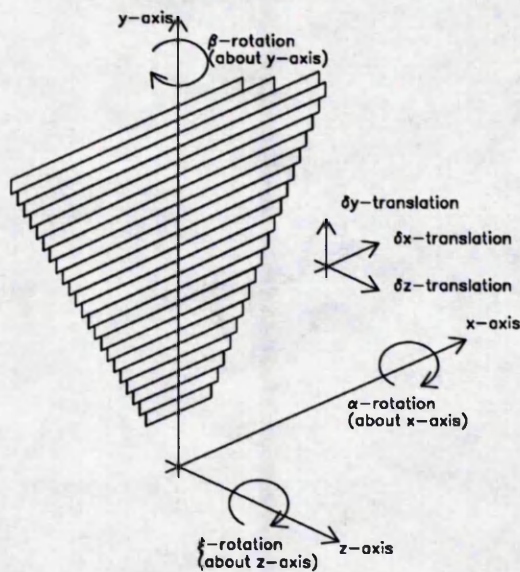
Figure 4.17: Straight line fit to  $z_{meas}$ , obtained using the new algorithm, against  $z$ .

# Chapter 5

## Alignment

### 5.1 Introduction

The momentum resolution of the forward muon spectrometer is primarily dictated by multiple scattering in the iron toroid but at higher momenta the spatial resolution of the drift chambers becomes increasingly important. In order to fully utilise the spatial resolution of the drift chambers, it is necessary to align the drift chambers to an accuracy of  $50 \mu\text{m}$  along the drift axis, defined here as the  $y$ -axis, and to an accuracy of 1 cm along the charge division axis, defined here as the  $x$ -axis. As it is the  $\theta$  angle of the track which is ultimately being measured, it is also necessary to align the chambers along the direction of the beam axis, defined here as the  $z$ -axis, with sufficient accuracy so as not to compromise the  $y$ -alignment of the drift chambers. For the forward muon spectrometer in which tracks have an angular range in  $\theta$  of  $3^\circ$  to  $18^\circ$ , the drift chambers need to be positioned in  $z$  to an accuracy of 1 mm. The drift cells are supported on the octant frames by dowels to a precision of  $50 \mu\text{m}$  along the  $y$ -axis and of order a few mm along the  $x$ - and  $z$ -axes. However, the octants are only positioned to an accuracy of order 1 cm by their support structure and thus, require further alignment. For each octant, three translational and three rotational quantities are required to fully describe their position. The precision to which these quantities must be measured is determined by the accuracy to which the individual drift chambers must be aligned. All these quantities and their required



Alignment Quantity	Estimated Accuracy Required
$\delta y$	$50\mu\text{m}$
$\delta x$	1cm
$\delta z$	1mm
$\delta \xi$	$0.01^\circ$
$\delta \alpha$	$1^\circ$
$\delta \beta$	$10^\circ$

Figure 5.1: Alignment requirements for the forward muon detector.

precision are summarized in figure 5.1.

Two methods have been considered for alignment of octants of the forward muon detector:

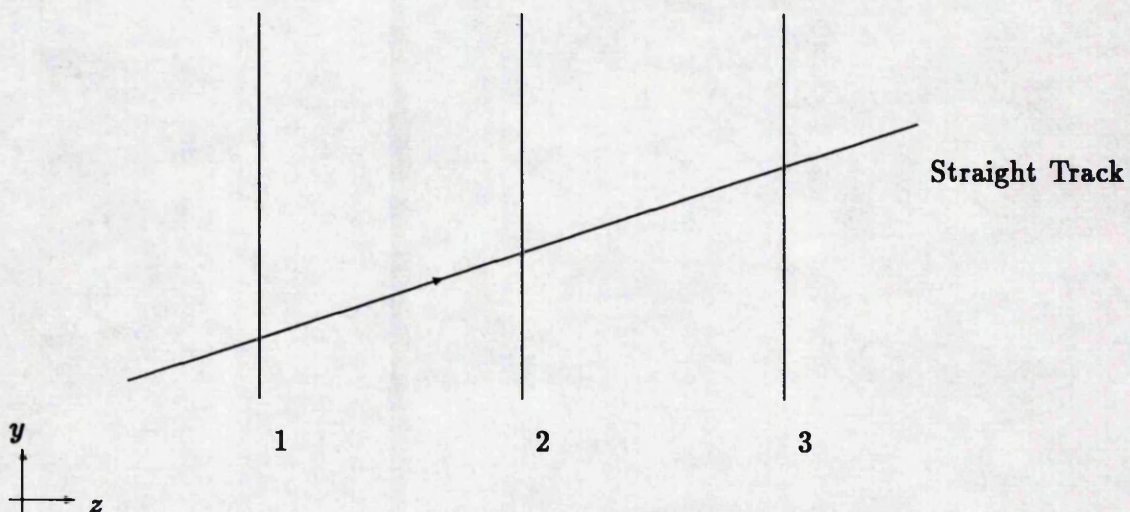
- A survey of the forward muon detector.
- The use of 'checksums' on straight tracks, measured by the forward muon detector with the toroid field off.

Access to the forward muon detector is restricted, so a survey at best can achieve resolutions of a few mm. The 'checksum' method can provide more precise alignment

information, if sufficient numbers of tracks are used. In reality, a combination of these two methods will be used.

## 5.2 The 'Checksum' Method

Consider a straight line which intersects three parallel planes ( $z = z_1, z_2, z_3$ ) at  $(x_1, y_1)$ ,  $(x_2, y_2)$  and  $(x_3, y_3)$  respectively.



For the points of intersection, the following expression is generally true,

$$\frac{y_2 - y_1}{y_3 - y_1} = \frac{z_2 - z_1}{z_3 - z_1}$$

Rearranging this expression, the following checksum is obtained,

$$C = Ay_3 - y_2 + (1 - A)y_1 \quad (5.1)$$

where

$$A = \frac{z_2 - z_1}{z_3 - z_1}$$

and  $C = 0$ . The equivalent checksum for the  $x$ -coordinate can be obtained by replacing  $y$  by  $x$  in equation 5.1.

If the FMD is run with the toroid field off, then equation 5.1 may be applied to the hit coordinates for the resulting straight tracks measured by the FMD. Two checksums are considered:

$$C_1 = -A_1 y_3 + y_2 - (1 - A_1) y_0$$

$$C_2 = +A_2 y_3 - y_1 + (1 - A_2) y_0$$

where

$$A_1 = \frac{z_2 - z_0}{z_3 - z_0}$$

$$A_2 = \frac{z_1 - z_0}{z_3 - z_0}$$

and  $y_n$  is parallel to the drift axis,  $z_n$  is parallel to the beam axis and the indices correspond to the theta layers, as shown in figures 3.1. Similar checksums are obtained for the charge division,  $x_n$ , axis by replacing  $y_n$  by  $x_n$ . Due to the finite spatial resolution of the drift chambers and to the multiple scattering in the iron toroid, checksums on the hit coordinates of real tracks measured by the FMD form a distribution. Furthermore, the distribution is shifted from zero due to the misalignment of the octants, and thus, by measuring this systematic shift, the octants can be aligned with respect to each other. Initially, only internal alignment of the theta octants parallel to the drift and charge division axes was considered, so that the systematic shift in  $C_1$  and  $C_2$  are given by:

$$C_1 = -A_1 \delta y_3 + \delta y_2 - (1 - A_1) \delta y_0 \quad (5.2)$$

$$C_2 = +A_2 \delta y_3 - \delta y_1 + (1 - A_2) \delta y_0 \quad (5.3)$$

where  $\delta y_n$  and  $\delta x_n$  are the misalignment of the octants in theta layer  $n$  parallel to drift and charge division axes respectively. The internal coordinate system with respect to which the alignment is done can be chosen freely, so the internal axes are

chosen so that theta layers 0 and 3 have no translational misalignment along their  $x$ - and  $y$ - axes:

$$\delta y_0 = \delta y_3 = \delta x_0 = \delta x_3 = 0$$

Equations 5.2 and 5.3 then become:

$$C_1 = +\delta y_2$$

$$C_2 = -\delta y_1$$

and hence, the systematic shift in the distributions of the checksums  $C_1$  and  $C_2$  for the  $x$ - and  $y$ -coordinates gives directly the misalignment of the theta 1 and theta 2 layers,  $\delta y_2(\delta x_2)$  and  $-\delta y_1(-\delta x_1)$ , with respect to the internal coordinate system used, respectively.

To study the checksum method of alignment, simulations with muon tracks generated at a single point immediately in front of the forward muon detector, travelling in the proton direction parallel to the beam, were done with the forward muon toroid field turned off. Five sets of simulated data, each with a different discrete generated muon momentum (5, 15, 25, 35, 50 GeV/c), were produced. Gaussians were fitted to the resulting checksum distributions obtained. Figures 5.2 and 5.3 show plots of the root mean square and the ratio of the mean to the error in the means for these Gaussian fits against the momentum of the generated tracks.

The theoretical rms of the checksum distributions for tracks parallel to the  $z$ -axis of the detector, referred to as 'flat' tracks, is given by,

$$\sigma_{C_1}^2 = A_1^2(z_0 - z_B)^2 \sigma_{scat}^2 + A_1^2 \sigma_0^2 + \sigma_2^2 + (1 - A_1)^2 \sigma_3^2 \quad (5.4)$$

$$\sigma_{C_2}^2 = (1 - A_2)^2(z_3 - z_B)^2 \sigma_{scat}^2 + A_2^2 \sigma_0^2 + \sigma_1^2 + (1 - A_2)^2 \sigma_3^2 \quad (5.5)$$

The first term in equations 5.4 and 5.5 corresponds to multiple scattering in the toroid.  $\sigma_{scat}$  is the root mean square deflection of the muon track in the plane of

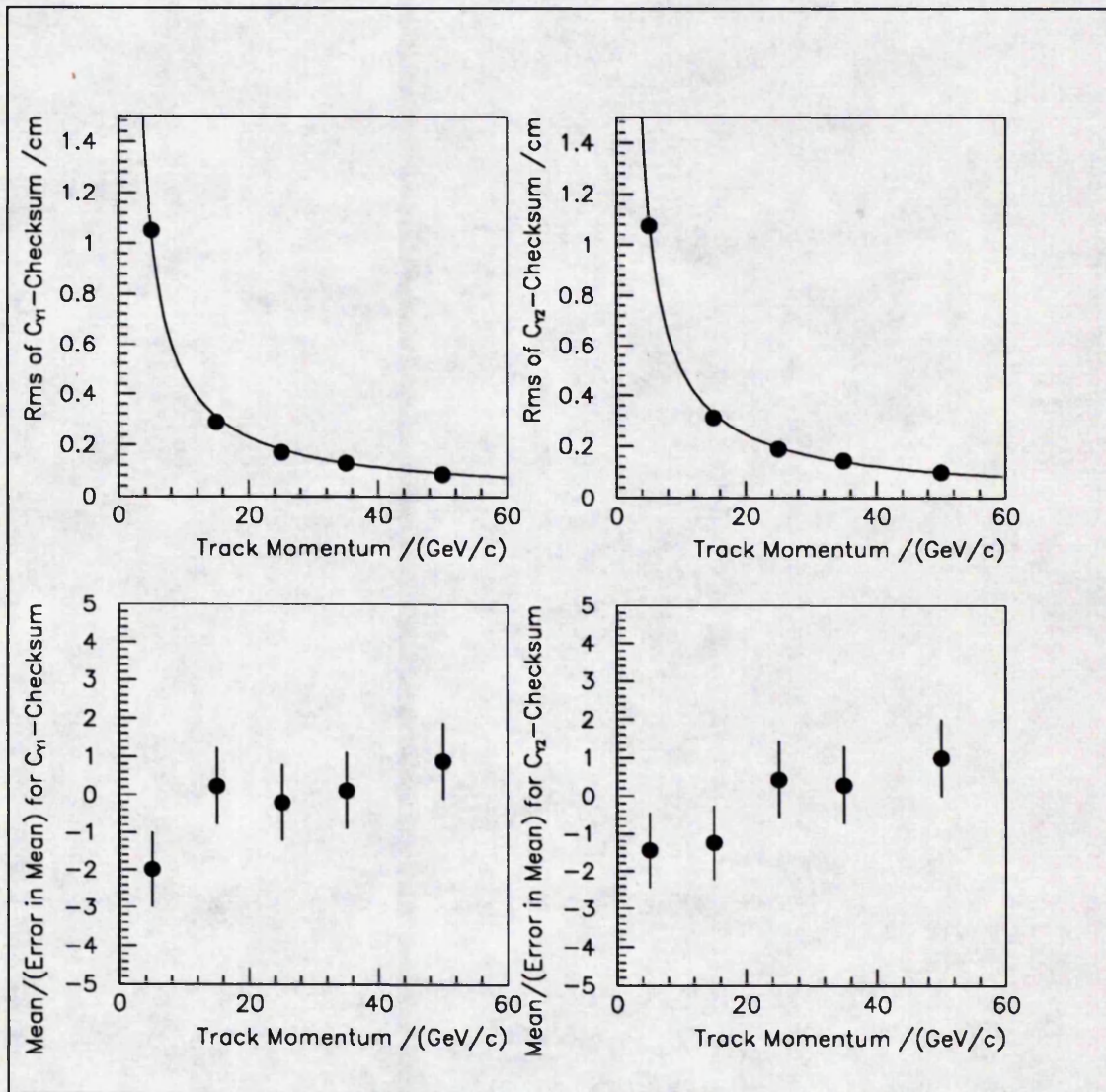


Figure 5.2: Parameters of Gaussian fits to  $y$ -checksum distributions.

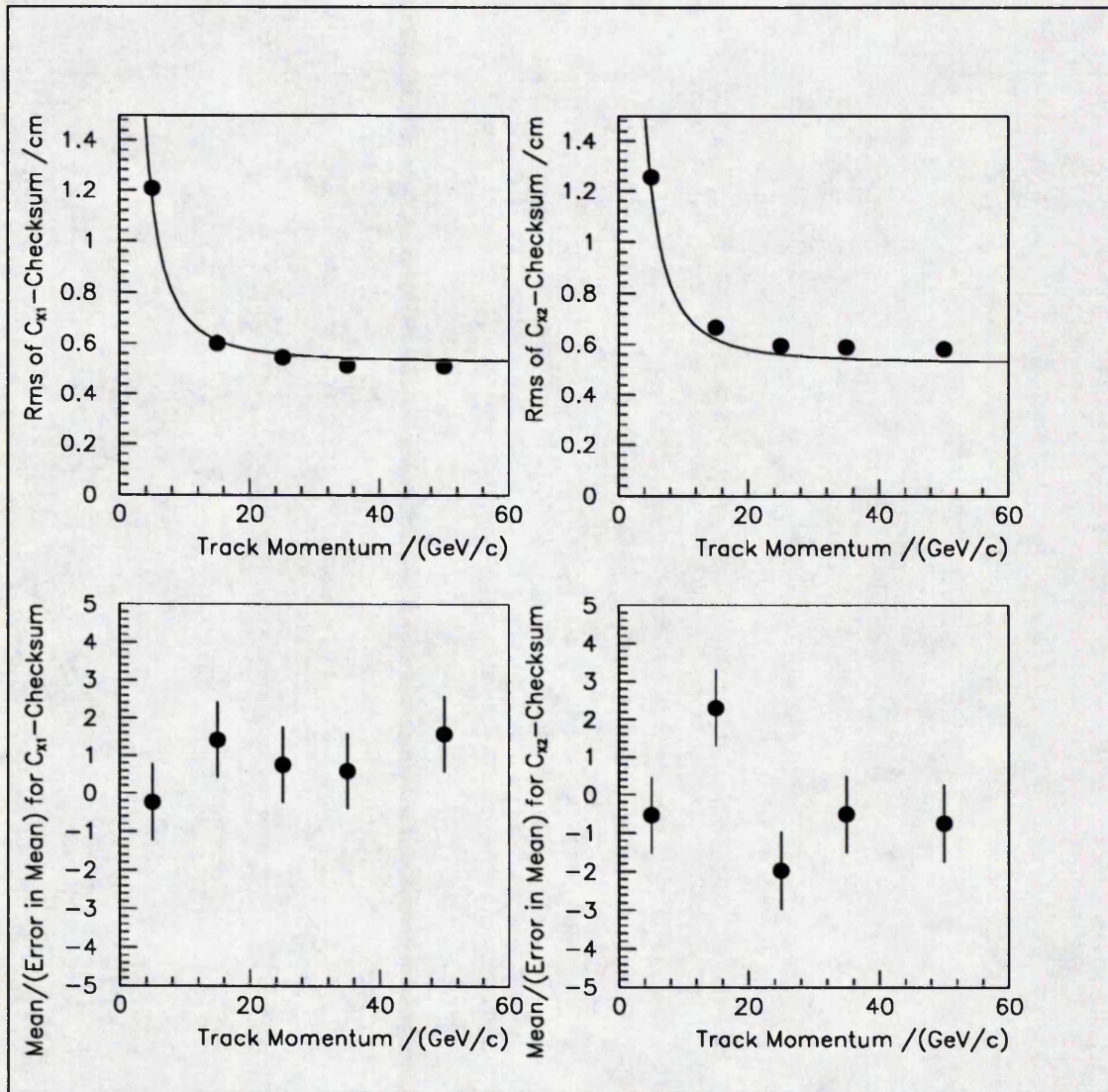


Figure 5.3: Parameters of Gaussian fits to  $x$ -checksum distributions.

the appropriate coordinate on traversing the iron toroid and is given by equation 3.2. The remaining terms result from the intrinsic spatial resolution of the drift chambers. For checksums on the hit  $y$ -coordinates,  $\sigma_n$  is the resolution of the drift coordinate and is independent of  $n$ . However, for checksums on the hit  $x$ -coordinate,  $\sigma_n$  is the resolution of the charge division coordinate which depends on the length of the drift chamber in which the track hit occurred and hence, is different for each of the hits in the checksum. The theoretical curves of  $\sigma_{C1}$  and  $\sigma_{C2}$  against the momentum of tracks incident on the forward muon detector are shown in figures 5.2 and 5.3. For these curves, the value for the momentum substituted into equation 3.2 was the geometric mean of the muon momentum entering and leaving the iron toroid; the muon was assumed to be minimally ionising [23], losing 1.4 GeV on traversing the iron toroid. It can be seen that expressions 5.4 and 5.5 represent the alignment checksum rms reasonably well. It can also be seen from the graphs that the means of the checksum distributions are consistent with zero.

The sensitivity of the alignment checksums makes them a good test of forward muon detector simulation code and reconstruction track finding code. The above results, thus, also confirm that the code is behaving correctly.

### 5.3 'Angled' Tracks

So far, only flat tracks have been considered. Tracks at an angle,  $\theta$ , to the  $z$ -axis of the detector ('angled' tracks) introduce further complications to alignment using the checksum method, in addition to the intrinsic complications of determining the coordinate of a hit in a drift cell associated with angled tracks.

As a result of the increased track length in the iron toroid for angled tracks and the geometry involved for converting the multiple scattering angle into the first term in the expressions for  $\sigma_{cn}^2$ , the first term in expressions 5.4 and 5.5 gain an additional factors of  $\sec^5(\theta)$  in the case of checksums on the hit  $y$ -coordinates; for checksums on the hit  $x$ -coordinates the factor is  $\sec^3(\theta)$ . This does not significantly effect the rms of the checksum distribution, even for  $18^\circ$  tracks. However, for the same reasons the rms of the checksum distribution varies with the actual magnitude of the multiple scattering angle and hence, varies on moving across the checksum

distribution. A small, symmetric increase in the rms of the checksum distribution on moving away from the centre is produced, except in the case of  $y$ -checksum distributions for angled tracks for which the rms of the checksum distribution varies monotonically on moving across the checksum distribution, resulting in a slight asymmetry. Although this does not significantly effect the rms of the checksum distributions, the mean of the asymmetric  $y$ -checksum distributions for angled may be significantly shifted from zero.

To investigate the effect of this asymmetry in the  $y$ -checksum distributions of angled tracks on its mean,  $\theta$  in the first term of the expression for  $\sigma_{c1}^2$  was replaced by the angle of the track leaving the iron toroid, after being multiple scattered,

$$\sigma_{c1} \rightarrow \sigma_{c1}(1 - aC_{y1})$$

where

$$a = \frac{2.5 \sin \theta}{A_1(z_B - z_0)}$$

and all the other terms were neglected. This modified expression for  $\sigma_{c1}$  was then used as the rms of a Gaussian distribution, resulting in the expression:

$$\exp \left[ \frac{-C_{y1}^2}{2\sigma_{c1}^2(1 - aC_{y1})^2} \right]$$

for the  $C_{y1}$  distribution. Plotting such curves and fitting Gaussians revealed that the shift in the mean is proportional to  $\sigma_{c1}^2$ ,  $\theta$  and the range over which the fit is made,  $\Delta C_{y1}$ , leading to the following expression for the ratio of the shift in the mean to the resolution of the mean:

$$\frac{\delta \bar{y}}{\sigma_{\bar{y}}} \propto \sigma_{c1} \theta \Delta(C_{y1}) \sqrt{N} \quad (5.6)$$

where the resolution with which the mean of the distribution can be determined,  $\sigma_{\bar{y}}$ , is given by  $\frac{\sigma_{c1}}{\sqrt{N}}$ ,  $N$  being the number of tracks used. Thus, this model indicates

that the shift in the mean will be of greatest significance for low momentum, high theta tracks, as would be intuitively expected.

This model provides only a rough representation of the effect on the mean of the asymmetry in the  $y$ -checksum distributions for angled tracks and the actual values for the shifts in the mean predicted by this model are expected to be pessimistic. Thus, simulations were carried out with 5 GeV/c tracks at  $15^\circ$  to obtain an accurate value for the shift in the mean. The mean obtained for the  $C_{y1}$  checksum distributions from these simulations was  $320 \pm 350 \mu\text{m}$  for 1500 tracks, compared with  $600 \mu\text{m}$  from the above model. Thus, no asymmetry can be resolved for this sample of 1500 tracks and from equation 5.6, it is expected that no asymmetry will be resolvable for samples of less than 1500 tracks at lower angles in theta and higher momenta.

## 5.4 Nature of Beam Halo

Experience with previous experiments suggests that a high rate of high momentum tracks will be produced by beam-gas and beam-wall interactions. These may provide a suitable source of tracks for alignment of the FMD, enabling sufficient statistics to be accumulated rapidly. Beam background tracks also tend to have low theta angles, removing any problems of asymmetric distributions. Simulations of beam background events already exist on the DESY IBM and these can be used to study the feasibility of aligning the octants in the forward muon detector using beam halo.

Beam-gas events are simulated by generating 820 GeV proton on fixed target proton interactions and distributing the event vertices evenly in  $z$  over the range -87.5 m to 10 m, this being the estimated range over which the H1 detector is expected to be sensitive to beam-gas events. The  $x$ - and  $y$ -coordinates are given by the calculated phase ellipse of the beam. The events are then tracked to a plane in front of the H1 detector. For beam-wall events, the interactions are generated by shooting 820 GeV protons, parallel to the  $z$ -axis, on the first QS quadrupole (-40 m). The events are then again tracked to a plane in front of the H1 detector. 57613 beam-wall events and 100000 beam-gas were generated.

Simulations with these beam background events tracked through the H1 detector were available on the DESY IBM. These simulations which require a large amount of CPU time, had the forward muon toroid field on and so could not be used directly to test the 'checksum' method of aligning the forward muon detector. However, they allowed the nature of beam halo tracks through the H1 detector and forward muon detector to be investigated.

For the simulated beam halo events, particle tracks leaving the FMD volume were extrapolated back to the plane of the last theta layer, and a cut in the radius at which the particles crossed this plane was made (60 cm to 325 cm), to select only tracks which passed through the last theta layer. The track was required to be charged and to have a momentum greater than 100 MeV/c to remove low energy tracks which were mainly secondary electrons and photons. The track was also required to point back to a  $z$ -vertex before the last theta layer to remove tracks which originated from the beam pipe after the last theta layer. 3796 tracks were obtained from the 57613 beam-wall events generated. These tracks were a mixture of protons, pions, kaons and muons, each with a mean momentum of order 1 GeV/c and electrons which had a mean momentum of 200 MeV/c. Similarly, 8641 tracks were obtained from the 100000 beam-gas events generated, with a composition similar to the beam-wall case.

If a further cut is made on the above selected tracks such that the parent track must pass through the plane in front of H1 at a radius greater than 30 cm, corresponding to the inner radius of the veto wall, then only muon tracks which have penetrated the rest of the H1 detector are retained. 193 muons from beam-wall and 207 muons from beam-gas events were obtained, both with a mean momentum of 14 GeV/c. These muon tracks may be suitable for aligning the forward muon detector. The veto wall is actually situated between 6.55 m and 6.45 m, whereas the plane in front of H1 is at 5.80 m. However, the muon tracks selected have a mean angle to the beam axis of  $2.5^\circ$  and so the above results are not significantly affected by this shift in the  $z$ -position of the veto wall.

## 5.5 Alignment with Beam Halo

To test the possibility of using beam halo muons to align the forward muon detector, the original simulations of beam-wall and beam-gas events, tracked to a plane in front of H1, were scanned and muon tracks which passed through the plane in front of H1 at a radius greater than 30 cm were filtered out. These selected muons were then tracked through H1 using the H1 simulation program with the forward muon toroid turned off. By processing only the selected muon tracks, the CPU time required was significantly reduced. 311 muon tracks, for the combined beam-wall and beam-gas simulations, passed through a plane in front of the forward muon detector between radii 54 cm and 192 cm, corresponding to the area of the first theta layer. Momentum, phi, theta and radial distributions for these muons are shown in figures 5.5 and 5.4. Figure 5.6 shows the distribution of the hits for these muons in the plane in front of the forward muon detector. An asymmetry in phi can be seen for the beam-wall tracks. This results from a combination of the initial proton - beam-wall interaction vertex being asymmetrically off-axis in phi and the magnetic field in the beam. In reality, protons can be off-axis along any axis perpendicular to the beam and, hence, no asymmetry is expected.

The checksum distributions for these tracks are shown in figure 5.8. Fitting functions to these distributions is more complicated than for the simulations with fixed track momenta and positions, as previously done. Variation in track momenta and position leads to checksum distributions which are a convolution of Gaussians with a corresponding variation in rms. For the  $y$ -checksum distributions, the Gaussian rms depends only on the track momentum, ignoring the small variation with track angles. Attempts to fit Gaussians to the  $y$ -checksum distribution gave only poor results and so the effect of variation in track momentum had to be investigated. The momentum distribution of the tracks on which the  $y$ -checksum was performed is shown in figure 5.7. By considering figures 5.2 and 5.7, it can be seen that over the beam halo track momentum distribution range, the rms of the corresponding Gaussian varies significantly. In order to obtain an analytic function for the  $y$ -checksum distributions, the beam halo momentum distribution was represented by the function  $e^{-ap^2}$ . Neglecting the contribution of the spatial resolution of the drift chamber to  $\sigma_{cn}$  so that  $\sigma_0/p$  can be used to describe the variation of  $\sigma_{cn}$  with track momentum,  $p$ , the  $y$ -checksum distribution corresponding to this momentum distribution

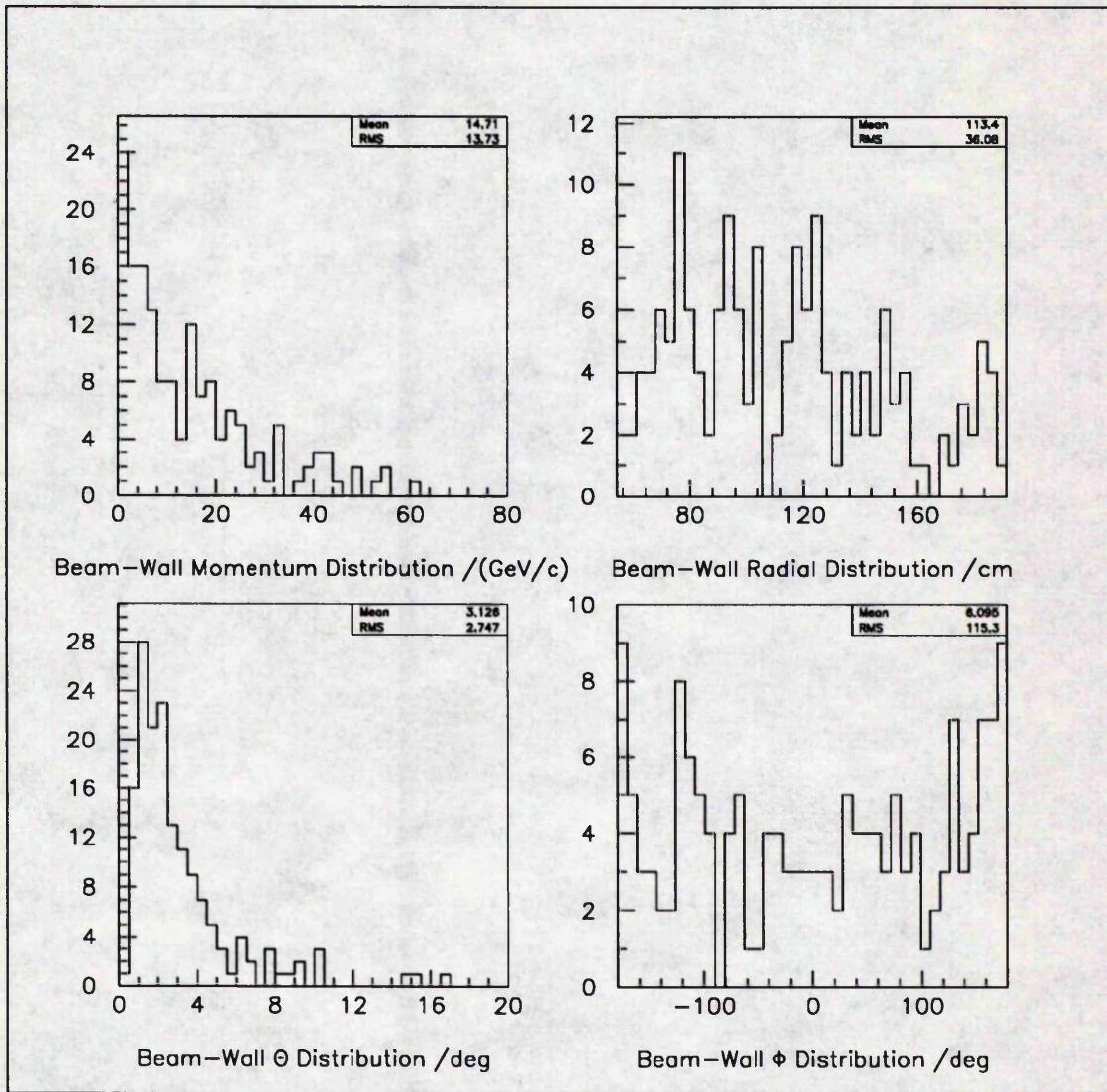


Figure 5.4: Distributions for beam-wall muon tracks.

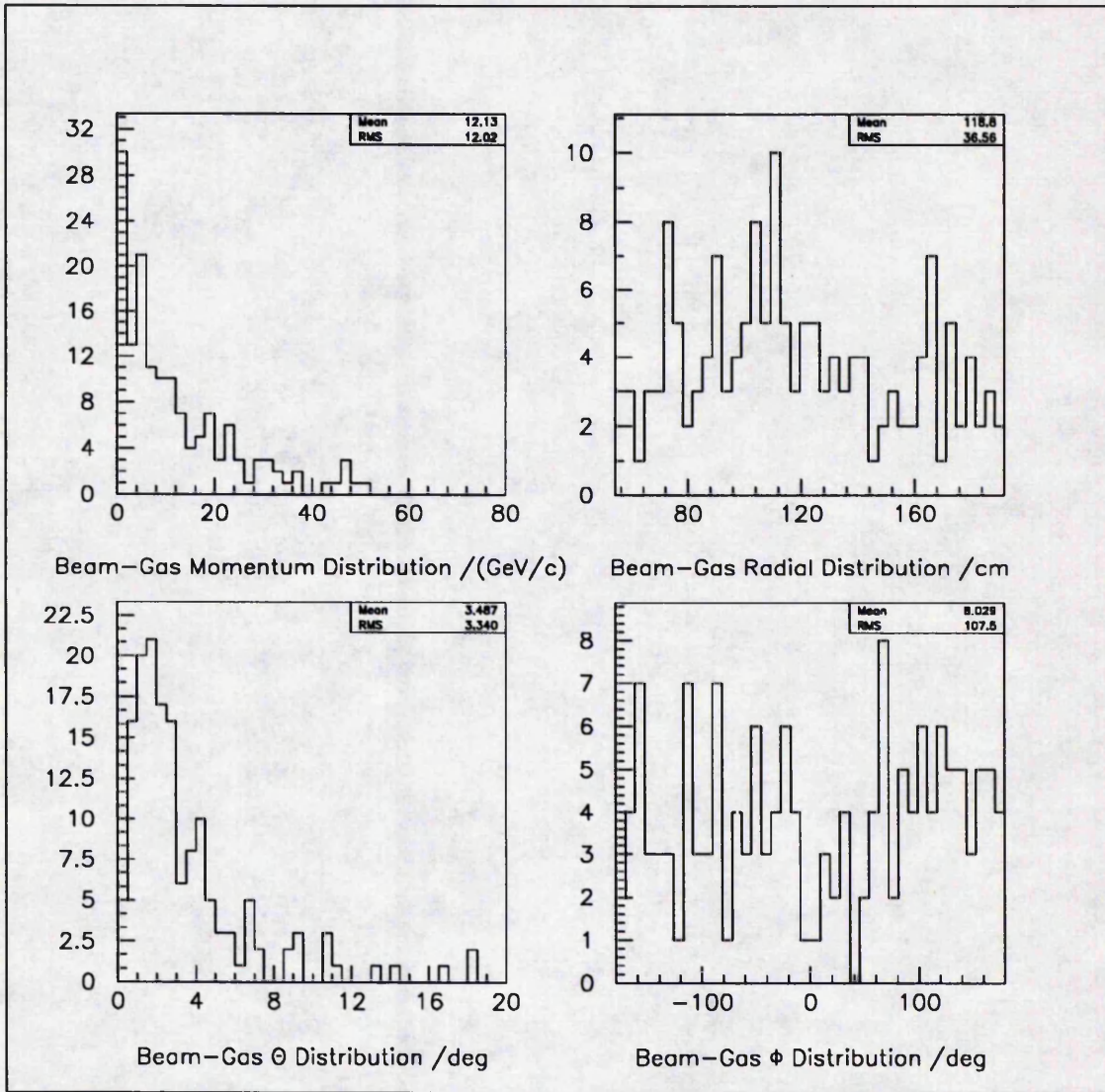


Figure 5.5: Distributions for beam-gas muon tracks.

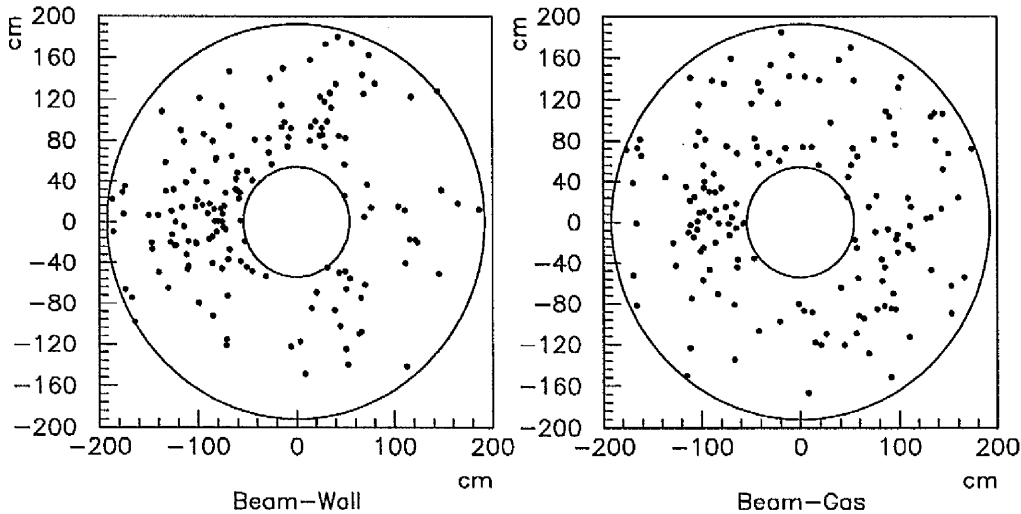


Figure 5.6: Distribution of hits for simulated beam-wall and beam-gas Tracks.

is a Breit-Wigner :

$$\frac{F_0}{(1 + (x - x_0)^2/2a\sigma_0^2)}$$

The function  $e^{-ap^2}$  was found to give a reasonable fit to the beam halo momentum distribution above 12.5 GeV/c, with  $a = (0.82 \pm 0.22) \times 10^{-3}$ ,  $\chi^2 = 0.66$ . The fit becomes increasingly poor below 12.5 GeV/c. However, from figure 5.7 it can be seen that the Gaussian distribution for tracks below 12.5 GeV/c become increasingly broad. Thus, if the region over which a function is fitted to the  $y$ -checksum distribution, is restricted, then tracks below 12.5 GeV/c can be considered to contribute a constant term to the  $y$ -checksum distribution. Fitting a Breit-Wigner plus constant to the  $y$ -checksum distributions over the range -0.35 cm to 0.4 cm gave reasonably good results. The fits are shown in figures 5.8 and the corresponding fitted parameters are given in table 5.1.

It is possible to extend the above method by replacing the function  $e^{-ap^2}$

Table 5.1: Parameters of Breit-Wigner plus constant fits to  $y$ -checksum distributions for simulated beam halo tracks.

	$y$ -checksum 1	$y$ -checksum 2
$F_0$	$9.8 \pm 2.4$	$9.4 \pm 2.2$
$1/2a\sigma_0^2/\text{cm}^2$	$36 \pm 28$	$18 \pm 12$
Mean, $x_0/\mu\text{m}$	$420 \pm 210$	$-300 \pm 290$
Constant	$2.6 \pm 1.1$	$2.3 \pm 1.6$
Entries	134	145
$\chi^2$	0.67	0.68

by  $e^{-ap^2} \times$  (a polynomial in  $p$ ), so that better fits to the beam halo momentum distribution can be obtained. This may be required when higher statistics are used or to describe the real beam halo momentum distribution.

The estimated rate of the proton - beam-wall interactions is 500 kHz. Thus, for the full generated sample of 57613 events, each selected muon track corresponds to 9 Hz. The proton-beam-gas interaction rate is estimated to be 3 kHz  $\text{m}^{-1}$ , assuming a vacuum in the beam pipe of  $3 \times 10^{-9}$  Torr composed of 50%  $\text{H}_2$  and 50%  $\text{O}_2$  and the number of protons in the ring to be  $2 \times 10^{13}$ , corresponding to design luminosity. Thus, for the  $10^5$  beam-gas events generated, each selected muon track corresponds to 3 Hz. The total rate at which muons are selected for alignment of the FMD in the above simulations is then given by  $91 \times 9 + 74 \times 3 = 1041$  Hz. The above checksums provide an alignment resolution along the drift axis of 250  $\mu\text{m}$ . To achieve 50  $\mu\text{m}$  would require, assuming the resolution has a  $\frac{1}{\sqrt{N}}$  dependence,  $25 \times$  more data for each of the eight octants which corresponds to 30 seconds of data taking for a muon track selection rate of 1 kHz.

For the  $x$ -checksum distributions, the situation is expected to be more complicated, as the  $x$ -checksum rms depends on the length of the drift cells hit, as well as the track momentum. However, from figure 5.3 it can be seen that the  $x$ -checksum rms is approximately constant above 12.5 GeV/c for a particular drift cell length, and as tracks tend to pass through near the inner radius of octants for beam halo, the variation in drift cell length is only small. Thus, a Gaussian fit to the  $x$ -checksum

Table 5.2: Parameters of Gaussian plus constant fits to  $x$ -checksum distributions for simulated beam halo tracks.

	$x$ -checksum 1	$x$ -checksum 2
Height	$7.5 \pm 1.2$	$9.6 \pm 1.8$
rms/cm	$0.66 \pm 0.10$	$0.58 \pm 0.13$
Mean/ $\mu\text{m}$	$250 \pm 990$	$192 \pm 84$
Constant	$1.4 \pm 0.4$	$1.7 \pm 0.5$
Entries	152	163
$\chi^2$	0.61	0.75

distribution is actually found to be adequate. A constant is included, as for the  $y$ -checksum distributions, so as to accommodate for tracks with momenta below 12.5 GeV/c and tracks which pass through the octants at higher radii. The fits are shown in figure 5.8 and the corresponding parameters are given in table 5.2.

The above checksums provide an alignment resolution along the charge division axis of 900  $\mu\text{m}$ , which is already better than the required resolution of 1 cm.

As filtering out muon tracks for simulating their passage through H1 significantly reduces the CPU time necessary, it should be possible to increase the number of beam halo events simulated in future alignment studies.

## 5.6 Alignment with Real Beam Halo Data

A run was carried out with the real forward muon detector with the toroidal field off. The veto wall in coincidence with the forward and backward instrumented iron end caps was used to trigger on beam halo tracks. Such tracks correspond to penetrating muon tracks which have passed through the veto wall, as considered in the previous simulations of alignment using beam halo. The drift velocity and  $t$ -zero used to calculate the hit coordinates were obtained as described in chapter 4. To

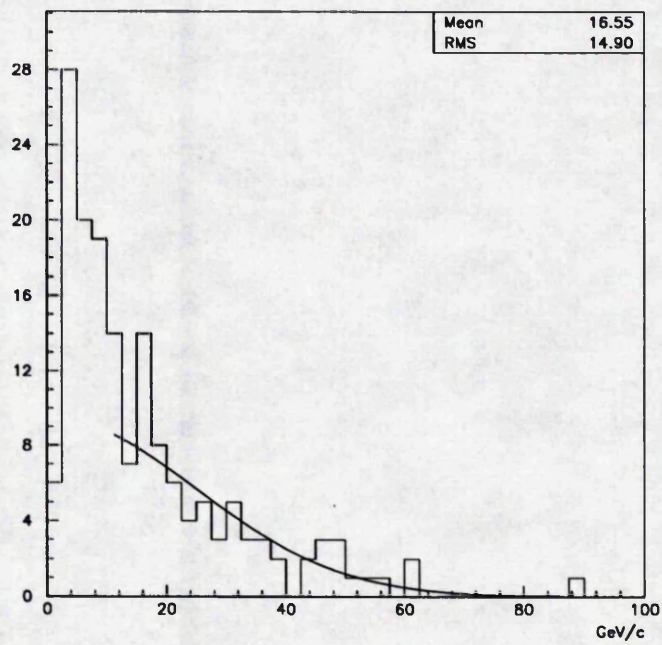


Figure 5.7: Momentum distribution of muon tracks used in the  $y$ -checksum distributions for simulated beam halo tracks.

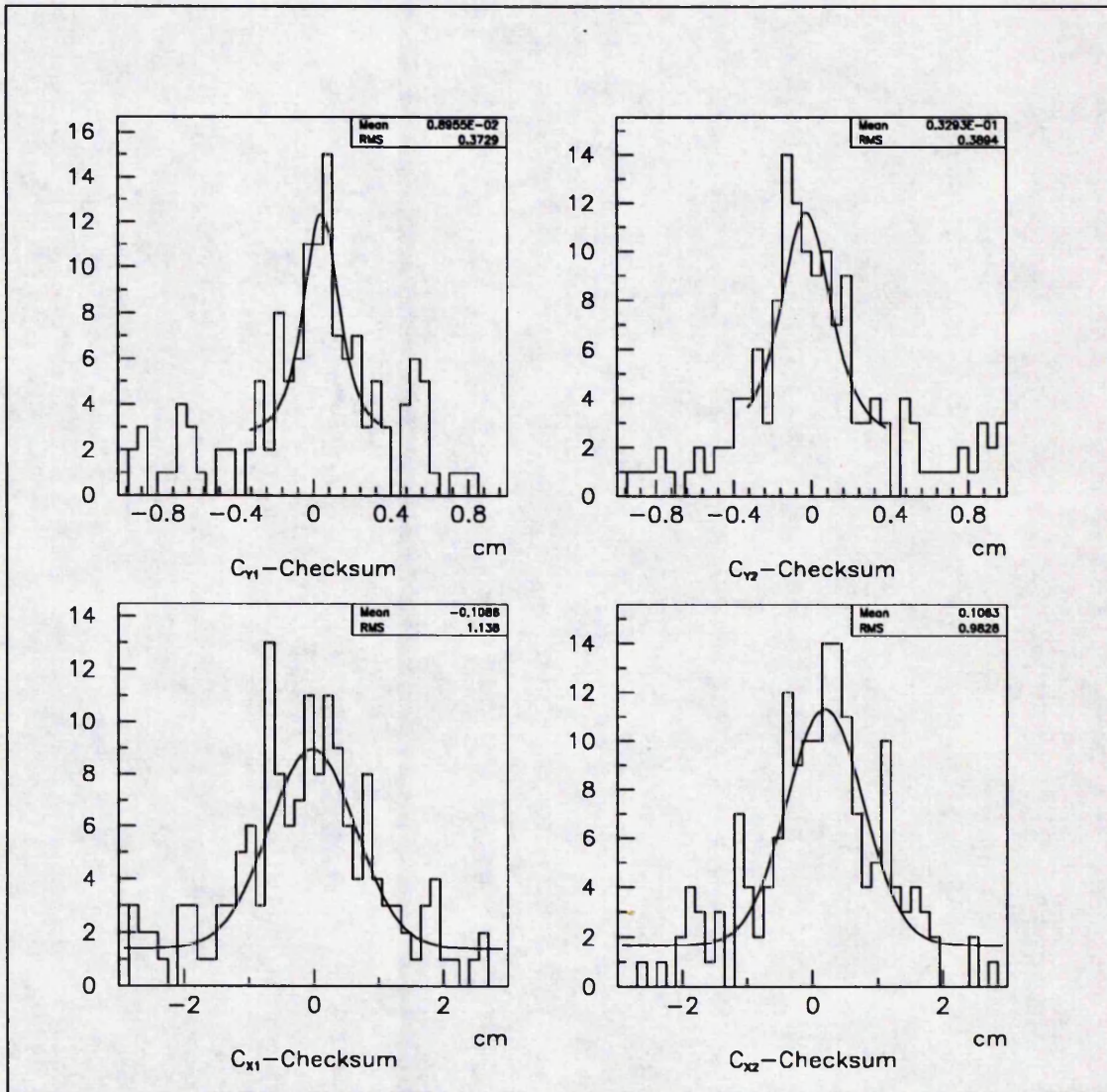


Figure 5.8: Checksum distributions for simulated beam halo tracks.

Table 5.3: Parameters of Breit-Wigner plus constant fits to  $y$ -checksum distributions for real beam halo tracks.

	$y$ -checksum 1	$y$ -checksum 2
$F_0$	$63.7 \pm 4.8$	$54.0 \pm 5.1$
$1/2a\sigma_0^2/\text{cm}^2$	$58.4 \pm 12.7$	$73.4 \pm 22.3$
Mean, $x_0/\mu\text{m}$	$9844 \pm 81$	$-3500 \pm 101$
Constant	$-1.56 \pm 1.39$	$2.26 \pm 1.62$
Entries	426	400
$\chi^2$	1.170	1.574

ensure that only clean tracks were reconstructed, only cells which contained a single hit and only hits which formed pairs were used.

Figure 5.9 shows the distribution of the hits in the first theta layer. These tracks result mainly from a probe inserted in the proton beam. The hits show an asymmetry similar to that produced by the beam-wall simulations, reflecting the asymmetry of the probe in phi. Only octants 3, 4 and 5 contain significant numbers of hits. The results of fitting curves to the  $y$ - and  $x$ -checksum distribution for these octants are shown in figures 5.10 and the fitted parameters are given in tables 5.3 and 5.4. For the Breit-Wigner plus constant fits to the  $y$ -checksum distributions, the fitted constants are consistent with zero and the fitted values for  $\frac{1}{2a\sigma_0^2}$  are consistent with the values obtained from the simulations. For the Gaussian plus constant fits to the  $x$ -checksum distributions, the fitted constants are consistent with zero. The fitted Gaussian rms is 2.0 cm which is  $3\times$  the value obtained by the simulations. This led to the revelation that the charge division resolution was a factor of  $3\times$  smaller in the simulation than for the real drift chambers which accounts for the difference between the real and simulated results.

It would be useful in future alignment studies with real data to carry out runs with the toroid field on, so as to allow the real beam halo momentum distribution to be obtained and compared with simulated beam halo momentum distribution.

Table 5.4: Parameters of Gaussian plus constant fits to  $x$ -checksum distributions for real beam halo tracks.

	$x$ -checksum 1	$x$ -checksum 2
Height	$39.5 \pm 3.0$	$42.5 \pm 4.8$
rms/cm	$1.94 \pm 0.23$	$1.77 \pm 0.26$
Mean/cm	$-0.108 \pm 0.121$	$-0.217 \pm 0.088$
Constant	$3.36 \pm 2.55$	$-1.67 \pm 5.21$
Entries	467	490
$\chi^2$	1.266	0.800

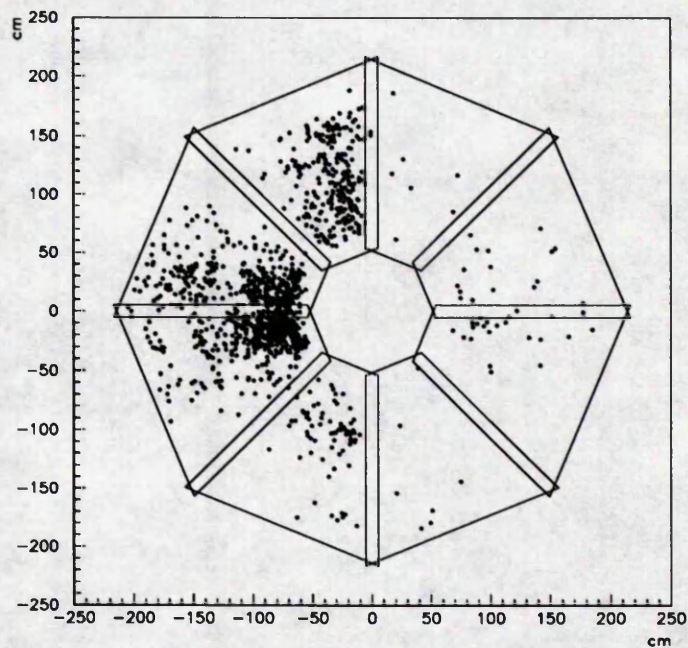


Figure 5.9: Distribution of hits for real beam halo tracks.

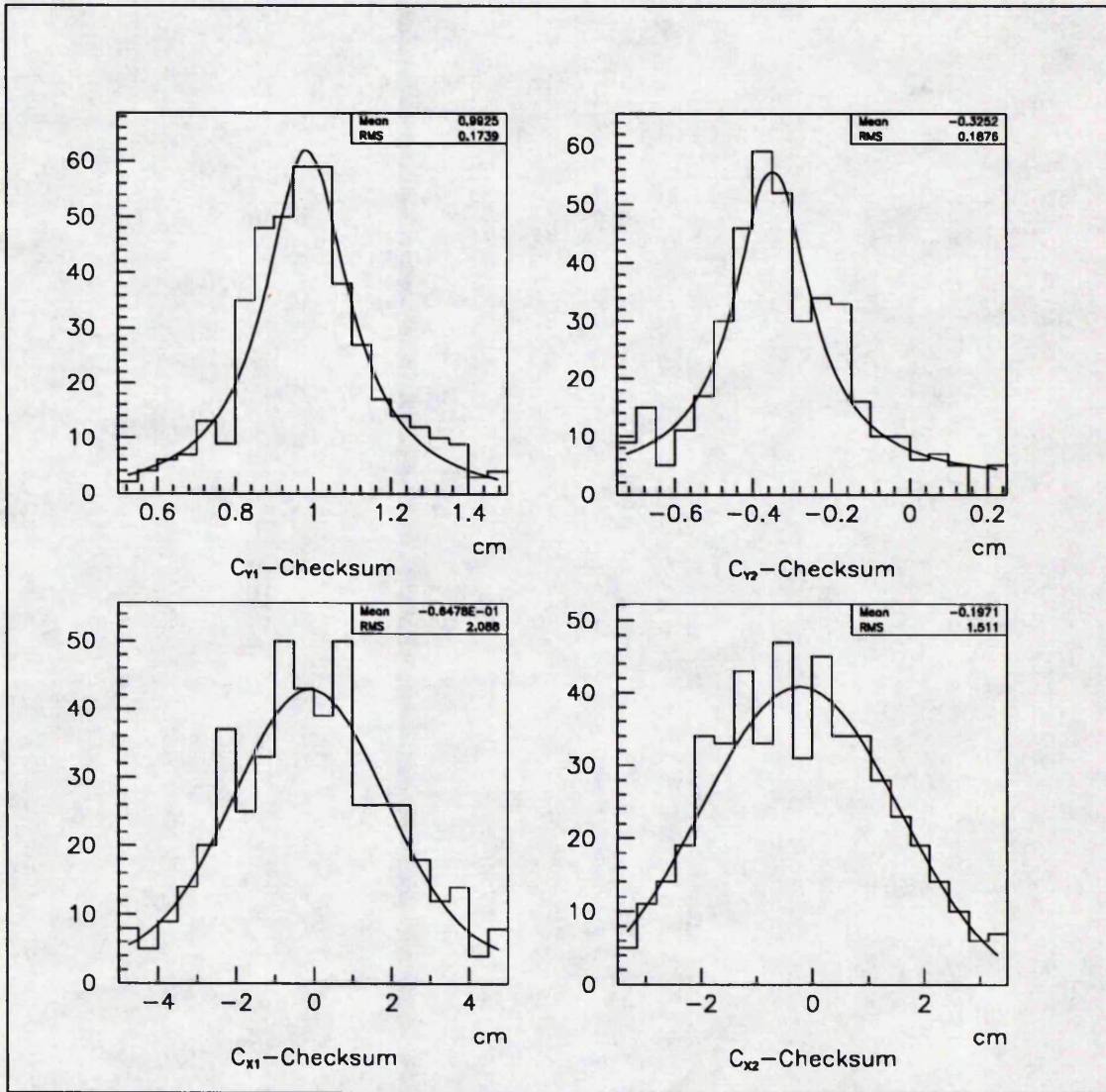


Figure 5.10: Checksum distributions for real beam halo tracks in octant 5.

## 5.7 Further Alignment Considerations

So far, only two translational alignment quantities, parallel to the drift and the charge division axes, have been considered. As can be seen from figure 5.1, other alignment quantities need to be measured. In particular, rotation in the plane of the octants and translation of the octants parallel to the  $z$ -axis need to be measured. These additional misalignments produce systematic variations in the checksum mean with track angle and position. The  $C_{y1}$ - and  $C_{x1}$ -checksums become:

$$C_{y1} = \delta y_2 - (y_3 - y_0) \left( \frac{\delta z_2 - A_1 \delta z_3}{z_3 + z_0} \right) + x_0 (\delta \xi_2 - A_1 \delta \xi_3) + (x_3 - x_0) A_1 (\delta \xi_2 - \delta \xi_3) \quad (5.7)$$

$$C_{x1} = \delta x_2 - (x_3 - x_0) \left( \frac{\delta z_2 - A_1 \delta z_3}{z_3 + z_0} \right) - y_0 (\delta \xi_2 - A_1 \delta \xi_3) - (y_3 - y_0) A_1 (\delta \xi_2 - \delta \xi_3) \quad (5.8)$$

and  $\delta z_n$  and  $\delta \xi_n$  are measured relative to the theta one layer, ie.  $\delta z_0 = 0$  and  $\delta \xi_0 = 0$ . As can be seen from the third and fourth terms in expressions 5.7 and 5.8, the relative rotation of the octants in the plane of the octants,  $\delta \xi_2$  and  $\delta \xi_3$ , can be obtained. However, these expressions only yield a linear combination of the relative  $z$ -translations,  $-\delta z_2 + A_1 \delta z_3$ , from their second terms. Thus, it will be necessary to supplement the information about the  $z$ -alignment of the FMD provided by the checksum method with a survey of the FMD. In order to obtain this alignment information, the radial position and theta angle of the tracks must be independently variable and have as large a range as possible. The beam halo simulations indicate that correlations between the radial position and the theta angle of a track is only weak for the beam halo muons used for aligning the forward muon detector. This would be expected as a result of the significant multiple scattering of the muon tracks by the rest of the H1 detector and also due to the large variation in the  $z$ -position of the initial vertex in the case of beam-gas events. Thus, beam halo may be ideal for obtaining the additional alignment quantities,  $\delta z_n$  and  $\delta \xi_n$ . Although, beam halo only provides a small range for track theta angle and radial position, the high rate of tracks produced by beam halo compensates for this. Further simulations are necessary to check the above expressions and to test the suitability of using beam halo to measure the additional alignment quantities.

A further consideration is any residual field in the iron toroid during the zero field runs. A calculation indicates that for alignment of the octants parallel to their drift axis to a precision of  $50 \mu\text{m}$  requires the residual field to be less than 0.5% of the full 1.5 T toroid field.

In addition to alignment of the theta octants with respect to each other, the phi octants will need to be aligned with respect to the theta octants. This will be achieved using the same checksum method as used to align the theta octants with respect to each other. Using tracks in the forward muon detector linked to tracks in the forward tracker, the forward muon detector will then finally be aligned with respect to the rest of the H1 detector.

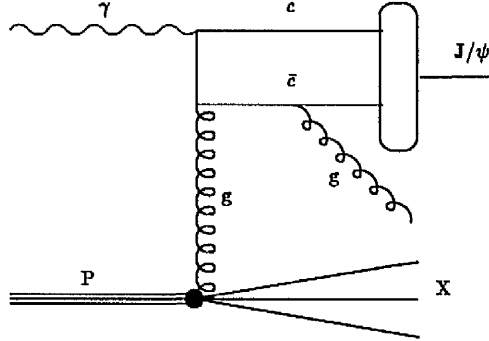
# Chapter 6

## $J/\psi$ Physics

### 6.1 $J/\psi$ Production Mechanisms

$J/\psi$  production has been studied in  $e^-e^+$  annihilation, hadronic collisions, deep inelastic scattering and photoproduction experiments and provides a rich source of information about particle interactions. For deep inelastic scattering experiments with incident electron and muon beam, the majority of  $J/\psi$  production is at low  $Q^2$  where the exchange photon is almost real and hence, such experiments can be considered to be photoproduction experiments. Previous photoproduction experiments and muonproduction experiments in the low  $Q^2$  region [32, 33, 34, 35] (centre-of-mass energy of photon-proton system,  $\sqrt{s_{\gamma p}} < 15$  GeV) have observed elastic, diffractive and inelastic  $J/\psi$  photoproduction.

Inelastic  $J/\psi$  photoproduction can be calculated perturbatively, the lowest order process being photon-gluon fusion of the incoming photon with a gluon from the proton,



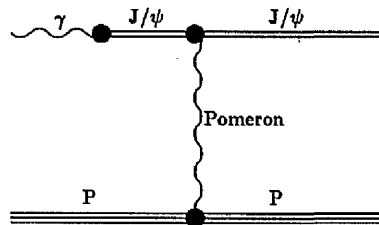
where the  $c\bar{c}$  pair forms a  $J/\psi$  meson. A gluon is included in the final state to conserve colour and spin. The differential cross-section for this process can be written as

$$\frac{d^2\sigma}{dx_{gluon}dt} = G(x_{gluon}) \frac{d\sigma}{dt} \quad (6.1)$$

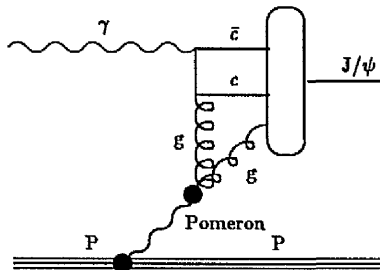
where  $t$  is the difference in the four momentum of the initial photon and the final  $J/\psi$  meson and  $x_{gluon}$  is the fraction of the proton four momentum carried by the initial gluon.  $G(x_{gluon})$  is the gluon distribution function for the proton. The differential cross section  $d\sigma/dt$  is for the process  $\gamma + g \rightarrow (c + \bar{c})_{J/\psi} + g$  which can be calculated using the colour singlet model. In the colour singlet model [36] the  $c\bar{c}$  pair is treated non-relativistically as an s-wave system in which the binding energy has been neglected. The wavefunction of the  $c\bar{c}$  pair at the origin fixes the normalisation and is deduced from the measured leptonic decay width of the  $J/\psi$ . It can be seen from equation 6.1 that inelastic  $J/\psi$  production is already sensitive to the gluon distribution of the proton in the leading order and thus can be used to determine the gluon density of proton. Rapidity,  $\eta$  and transverse momentum of the  $J/\psi$ ,  $p_{\perp}$  distributions measured by previous experiments [32, 33, 34, 35] were found to be in good agreement with those calculated using the colour singlet model. The overall normalisation, however, is typically out by a factor two to five. This is because only the lowest order process has been considered by the colour singlet model. Thus, a factor,  $K$ , which is assumed to be constant in  $\eta$  and  $p_{\perp}$ , is introduced into the calculated inelastic  $J/\psi$  photoproduction cross section.

Elastic and diffractive  $J/\psi$  photoproduction are high energy, small momentum transfer,  $t$ , processes which are described in terms of pomeron exchange between the incident proton and the incident photon. In elastic  $J/\psi$  photoproduction, the final state is an exclusive proton and  $J/\psi$  meson. In the case of the diffractive processes either the proton remains intact while the photon is dissociated into a  $J/\psi$  meson plus additional hadronic system (Diffractive Inelastic), or the photon couples to a  $J/\psi$  meson and the proton breaks up into a hadronic system (Diffractive Dissociation). Two examples of possible models for elastic  $J/\psi$  photoproduction via single pomeron exchange are:

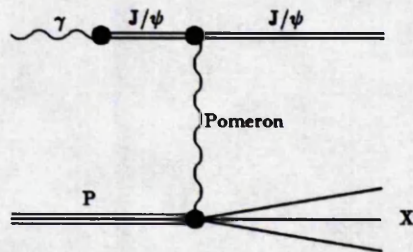
- The photon couples to a  $J/\psi$  using vector meson dominance, then the  $J/\psi$  is scattered by the proton via the exchange of a photon type pomeron which couples to single quarks [37].



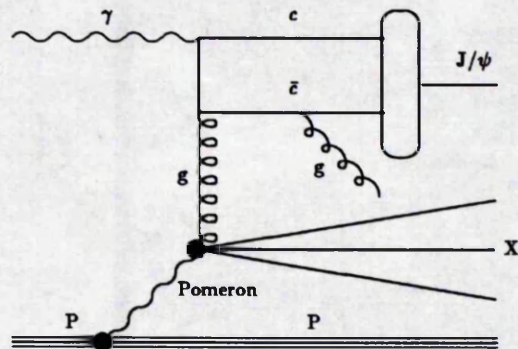
- The photon undergoes photon-gluon fusion with a gluon from the pomeron to produce a  $c\bar{c}$  pair which combines with the remnants of the pomeron, a gluon in the simplest case, to produce a  $J/\psi$  meson [38, 39].



The diffractive dissociation process can be modelled in a similar way to the first pomeron model by replacing the proton form factor by an inelastic structure function.



The diffractive inelastic process can be modelled in a similar manner to inelastic  $J/\psi$  photoproduction, except the initial state gluon for the photon-gluon fusion comes from a pomeron emitted by the proton rather than directly from the proton itself.



Elastic and diffractive  $J/\psi$  photoproduction at HERA will provide information about the photon- $J/\psi$  coupling and will allow the nature of the pomeron to be studied. Table 6.1 shows the predicted cross-section [10] for the elastic, inelastic and diffractive processes at HERA.

There is a probability of the photon behaving like a hadron. At the highest photon energies accessible at HERA, processes become significant in which a parton from the photon scatters off a parton from the proton. Such 'resolved photon' contributions to  $J/\psi$  photoproduction, are expected to be measurable for the first

Table 6.1: Main  $J/\psi$  production mechanisms at HERA

Elastic production with Photon type Pomeron	4.49 nb
Elastic production with Gluon dominated Pomeron (K=2)	2.20 nb
Diffractive Dissociation	1.40 nb
Direct Inelastic (K=2.8)	8.30 nb
Diffractive Inelastic	0.35 nb

time at HERA. Table 6.2 shows the estimated cross-sections [10] for these and other processes which are expected to become measurable at HERA.

$J/\psi$ 's are identified from their leptonic decays which are reconstructed using the tracking system. In order to determine the gluon density of the proton, various cuts must be imposed to select inelastic  $J/\psi$  photoproduction and to ensure that for the selected events, the perturbative calculation of the colour singlet model can be relied upon.  $y$  is obtained using the Jacquet-Blondel method [40] from all from all the final state particles measured in the calorimeter except the scattered electron. Using  $y$  and the reconstructed  $J/\psi$ ,  $x_{gluon}$  can be obtained. The gluon density of the proton is then obtained using equation 6.1 by comparing the experimentally determined differential cross-section,  $d\sigma(x_{gluon})/dx_{gluon}$ , with Monte Carlo simulations:

$$G(x_{gluon}) = \left( \frac{d\sigma(x_{gluon})}{dx_{gluon}} \right)_{Experiment} \left( \frac{G(x_{gluon})}{d\sigma(x_{gluon})/dx_{gluon}} \right)_{Monte\ Carlo}$$

Monte Carlo studies [10] show that a clean sample of  $J/\psi$  from photon-gluon fusion can be obtained with a signal to background ratio of 29 and that a range  $3 \times 10^{-4} \leq x_{gluon} \leq 0.1$  could be measured. They also showed that an integrated luminosity of  $20 \text{ pb}^{-1}$  would allow various parameterizations of the proton gluon density to be distinguished.

Table 6.2: Additional  $J/\psi$  production Mechanisms at HERA

Resolved Photon Process with gluon in the final state $g + g \rightarrow J/\psi + g$	0.09 nb
Resolved Photon Process with a hard photon in the final state $g + g \rightarrow J/\psi + \gamma$	0.023 nb
Resolved Photon Process producing $J/\psi$ via $\chi$ -decay	0.11 nb
$(\gamma, g) + g \rightarrow b\bar{b} \rightarrow J/\psi + X$	0.07 nb
Double Charm Production $c\bar{c} + J/\psi$	0.16 nb
Two Photon $J/\psi$ production $\gamma + \gamma \rightarrow \chi_{0,2} (\rightarrow J/\psi + \gamma)$	0.001 nb

## 6.2 Simulations of $J/\psi$

To test the performance of the forward muon detector, simulations of inelastic  $J/\psi$  production via photon-gluon fusion were studied. Events were generated using the EPJPSI [41] program and the simulated response of the H1 detector produced using the H1SIM program. Tracks in the forward muon detector were then reconstructed using the forward muon reconstruction code. The simulated events can be displayed using the H1 event display [42]. An event is shown in figure 6.1 in which the  $J/\psi$  decays into a dimuon pair where both the muons are detected in the forward muon detector.

The EPJPSI program uses the matrix element for the photon-gluon fusion process:

$$\gamma + g \rightarrow J/\psi + g$$

as given by the colour singlet model to describe the inelastic  $J/\psi$  photoproduc-

tion. The equivalent photon approximation which provides a good description of the  $eye$  vertex for low  $Q^2$  processes is then used to convert the  $J/\psi$  photoproduction into  $J/\psi$  electroproduction. The gluon from the incoming proton is given by the parton density inside the proton and is collinear with the incoming proton. Hadronisation of the proton remnant and the final state gluon is modelled using LUND monte carlo programs. 4441 inelastic  $J/\psi$  photoproduction events were generated with the  $J/\psi$  decaying either to a dimuon or dielectron pair.

### 6.3 Effect on Muon Tracks of Passage Through the H1 Detector

Before considering the detection of tracks by the forward muon detector, it is necessary to investigate the effect on muon tracks of passage through the rest of the H1 detector. 1000 negatively charged muons and 1000 positively charged muons were generated at the nominal vertex with momenta randomly distributed between 5 and 45 GeV/c, the theta angles randomly distributed between 3 and 18 degrees and the phi angles distributed randomly over the full 360 degree range. These muons were tracked through the H1 detector using the H1 simulation program to a plane in front of the forward muon detector and the muons obtained at this plane were compared to the original generated muons.

Muons are expected to lose energy primarily due to ionization of the material of the H1 detector between the interaction vertex and the forward muon detector. The energy lost by muons on passing through the rest of the H1 detector was found to be independent of the momentum of the track, as expected for a minimally ionizing particle, and also of the phi angle of the track. It was also found to be independent of theta angle, except for angles below  $5^\circ$  where the muon loses less energy because it remains for increasing fractions of its track length within the vacuum of the beam pipe. Figure 6.2a) shows the distribution of energy lost by muons before reaching the forward muon detector for tracks with theta angles greater than  $5^\circ$ . For energy loss due to ionisation, the fluctuation of the energy loss about the mean value is dominated by the relatively small number of 'close' ionising collisions which result in large energy losses. The Landau distribution which is obtained is therefore

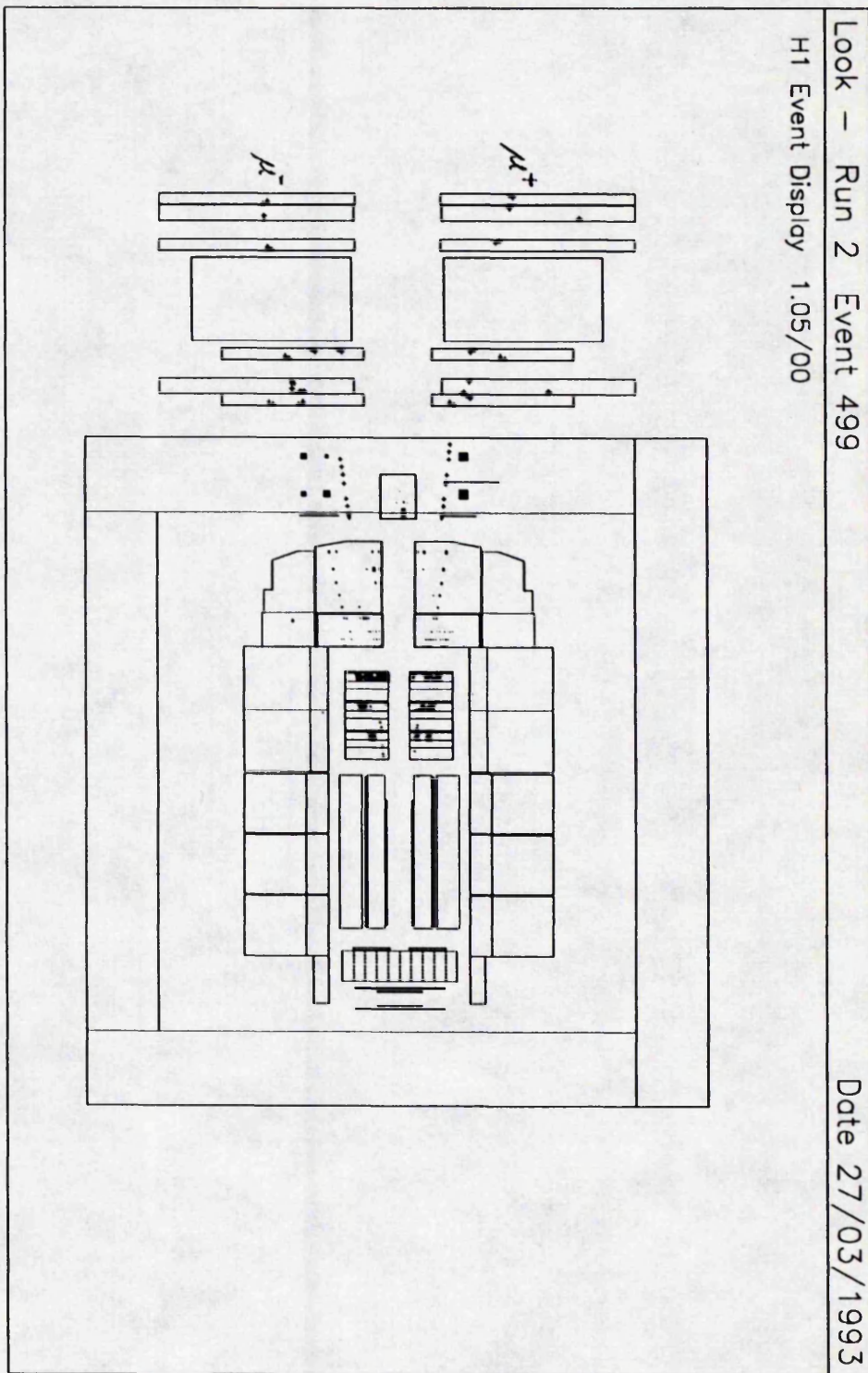


Figure 6.1: An inelastic  $J/\psi$  photoproduction event where the  $J/\psi$  decays into a dimuon pair detected by the forward muon detector.

asymmetric, with a tail extending to values much greater than average, as can be seen in figure 6.2a). To correct the momentum of the muon track as reconstructed by the forward muon detector for this energy loss, it is sufficient to use the mean of the distribution in figure 6.2a:

$$\text{Mean Energy Loss} = 3.0 \text{ GeV}$$

This value corresponds to the energy lost due to ionisation for a muon travelling through  $\sim 2.5$  m of iron which is a reasonable approximation of the material in front of the FMD.

The rms of the change in the theta and phi angles of the muon tracks on passing through the H1 detector show a  $p^{-1}$  dependence, as would be expected from multiple Coulomb scattering (equation 3.2) of the muon track by the material between the collision vertex and the forward muon detector. In addition, the phi angle also shows a systematic shift which has a  $p^{-1}$  dependence and a sign depending on the charge of the muon, as would be expected due to bending of the track due to the magnetic field of the solenoid. To measure the magnitude of the multiple Coulomb scattering and the bending of the track in the magnetic field of the solenoid, distributions of the change in theta,  $\Delta\theta$ , and phi angle,  $\Delta\phi$ , multiplied by the generated track momentum,  $p$ , were produced. Figure 6.2b) show  $\Delta(\theta)p$  for all muon tracks and figures 6.2c) and 6.2d) show  $\Delta(\phi)p$  for negatively charged and positively charged muons respectively. The rms of the  $\Delta(\theta)p$  distribution is  $12^\circ \text{ GeV}/c$  which agrees with the calculated value of  $12^\circ \text{ GeV}/c$  for multiple Coulomb scattering in 2.5 m of iron, obtained using equation 3.2. The rms of both the  $\Delta(\phi)p$  distributions is  $62^\circ \text{ GeV}/c$  which is consistent with the calculated value of  $65^\circ \text{ GeV}/c$  for multiple Coulomb scattering in 2.5 m of iron, obtained using equation 3.2. The mean of the  $\Delta(\phi)p$  distributions is  $\pm 42^\circ \text{ GeV}/c$  with the sign being given by the charge of the muon track. This is approximately consistent with a simple calculation of the bending of the track due to the magnetic field of the solenoid, assuming a field of 1.2 T over the tracking region, which gave  $\pm 50^\circ \text{ GeV}/c$ .

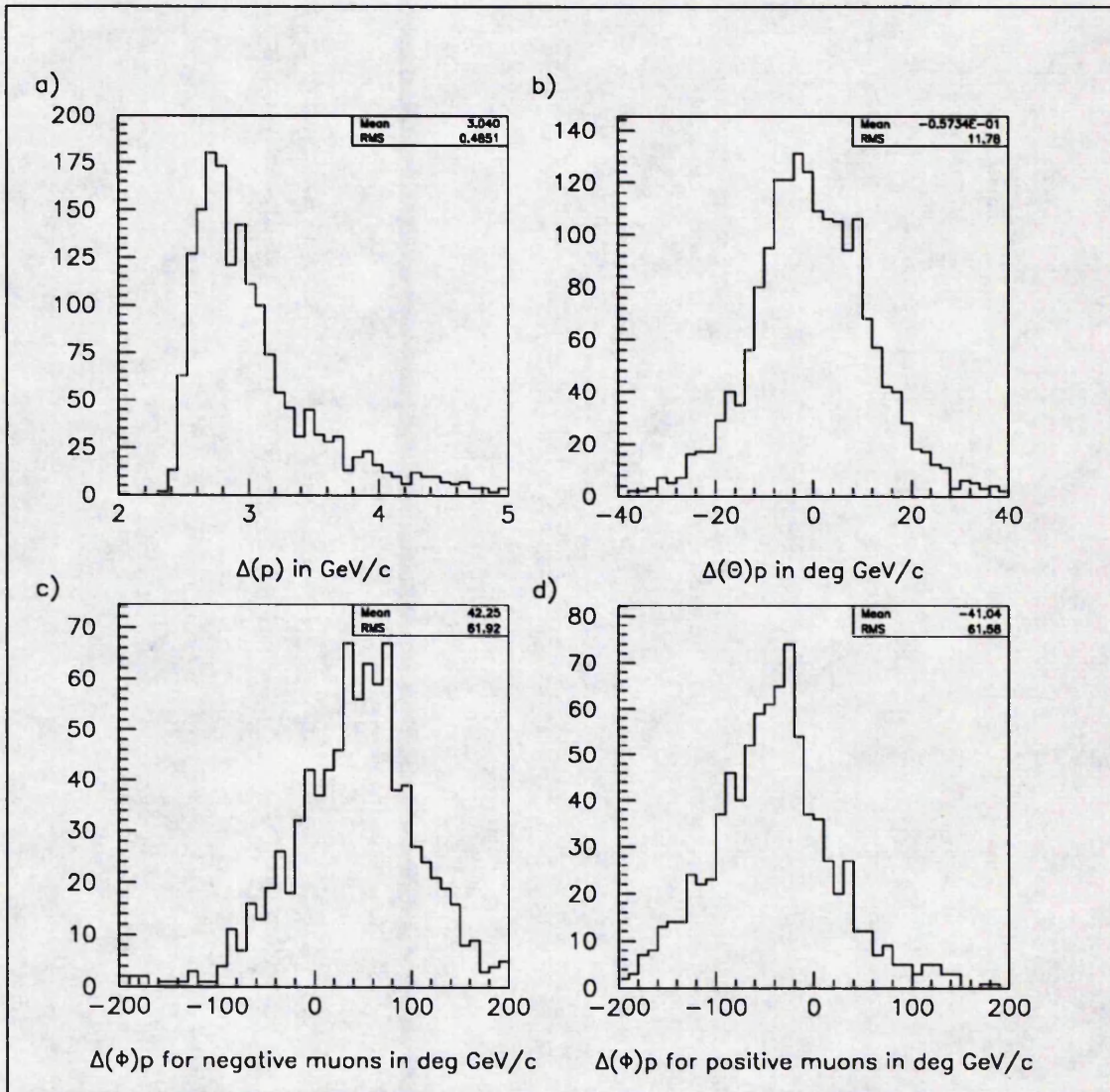


Figure 6.2: Distributions of the change in track parameters as a result of passing through the H1 detector.

## 6.4 Reconstruction of $J/\psi$ from their Dimuon Decays

For the simulated inelastic  $J/\psi$  photoproduction events, approximately half the  $J/\psi$ 's decay to a dimuon pair and half to a dielectron pair. Figure 6.3 shows the momentum distribution of tracks reconstructed in the forward muon detector for events in which the  $J/\psi$  decayed to a dimuon pair. The figure also shows the momentum distribution (shaded) of reconstructed tracks for events in which the  $J/\psi$  decayed to a dielectron pair. As can be seen from figure 6.3, the majority of tracks with reconstructed momenta of less than 3 GeV/c do not result from the decay of the  $J/\psi$ 's. It is also increasingly difficult to reconstruct muon tracks as their momenta falls below 3 GeV/c. Thus, a cut is introduced to remove tracks with reconstructed momenta below 3 GeV/c. A cut in  $\chi^2$  of 15 was also introduced to be consistent with the study of forward muon track reconstruction previously done. The remaining tracks were then corrected for their passage through the rest of the H1 detector as follows:

- Adding 3.0 GeV/c to the reconstructed momentum to compensate for energy lost by the muon on passing through the rest of the H1 detector.
- Using the adjusted reconstructed momentum,  $p_{rec} + 3.0$  GeV/c, the the reconstructed phi angle was corrected for bending of the track in the magnetic field of the main H1 solenoid by adding on,

$$\pm \frac{40}{(p_{rec} + 3.0)} \text{ degrees}$$

where the sign is given by the charge on the muon track.

The distributions of the difference between the reconstructed and generated momenta, theta angle and phi angle of the remaining reconstructed tracks are shown in figure 6.4 and the corresponding resolutions are summarized in table 6.3. Also shown in table 6.3 is the efficiency of reconstruction which is calculated using,

$$Efficiency = \frac{N_{rec}}{N_{expected}}$$

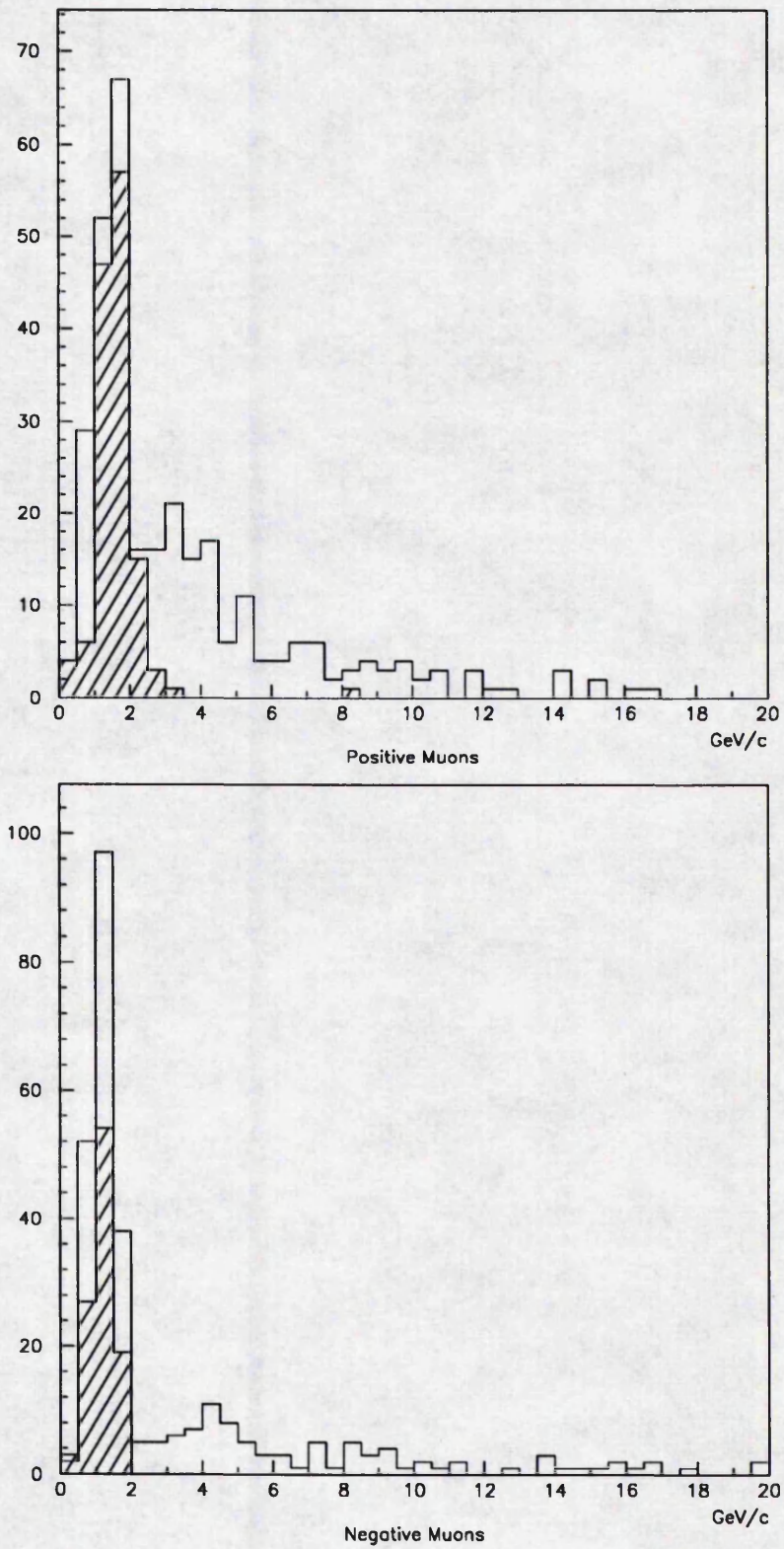


Figure 6.3: Reconstructed track momenta for events in which the  $J/\psi$  decays to a dimuon pair (hollow) and to a dielectron pair (shaded).

Table 6.3: Forward muon track reconstruction resolutions and efficiency.

Charge on Muon	Mean Momentum Resolution	Mean Theta Resolution	Mean Phi Resolution	Reconstruction Efficiency
-	3.5 GeV/c	1.5°	9.0°	37%
+	3.5 GeV/c	1.8°	9.0°	47%

where  $N_{rec}$  is the number of reconstructed tracks and  $N_{expected}$  is the number of tracks generated in the polar angular range  $4.5^\circ \rightarrow 17^\circ$  with momentum greater than 6 GeV/c, which would be expected to be reconstructed. It can be seen that the forward muon detector reconstructs muon tracks reasonably well, except for the low efficiency currently obtained which results for the problems of reconstructing tracks in the angular range  $6^\circ \rightarrow 10^\circ$ , as previously discussed. These results will be improved with the inclusion of the phi chambers and by linking the track to the forward tracker.

Graph 6.5 show the  $\log(x_{gluon})$  distribution for events in which a muon was reconstructed in the forward muon detector compared to the distribution for all generated events in which the  $J/\psi$  decays to a dimuon pair. From the  $x_{gluon}$  distribution it can be seen that although the forward muon detector will contribute to measurement at  $x_{gluon}$  lower than presently known, it does not contribute to the lowest  $x_{gluon}$  region obtainable at HERA where it will be possible to distinguish between various different predictions of the gluon density distribution.

As a final test of the forward muon detector, the invariant mass of dimuon pairs where both muons were detected by the forward muon detector, were reconstructed. The resulting distribution, shown in figure 6.6; has a mean of 3.2 GeV/c<sup>2</sup> compared with the mass of the  $J/\psi$  meson of 3.1 GeV/c<sup>2</sup>. The rms of the distribution is 0.8 GeV/c<sup>2</sup> compared with the cut in the reconstructed  $J/\psi$  invariant mass of  $3.1 \pm 0.4$  GeV/c<sup>2</sup> suggested in [10].

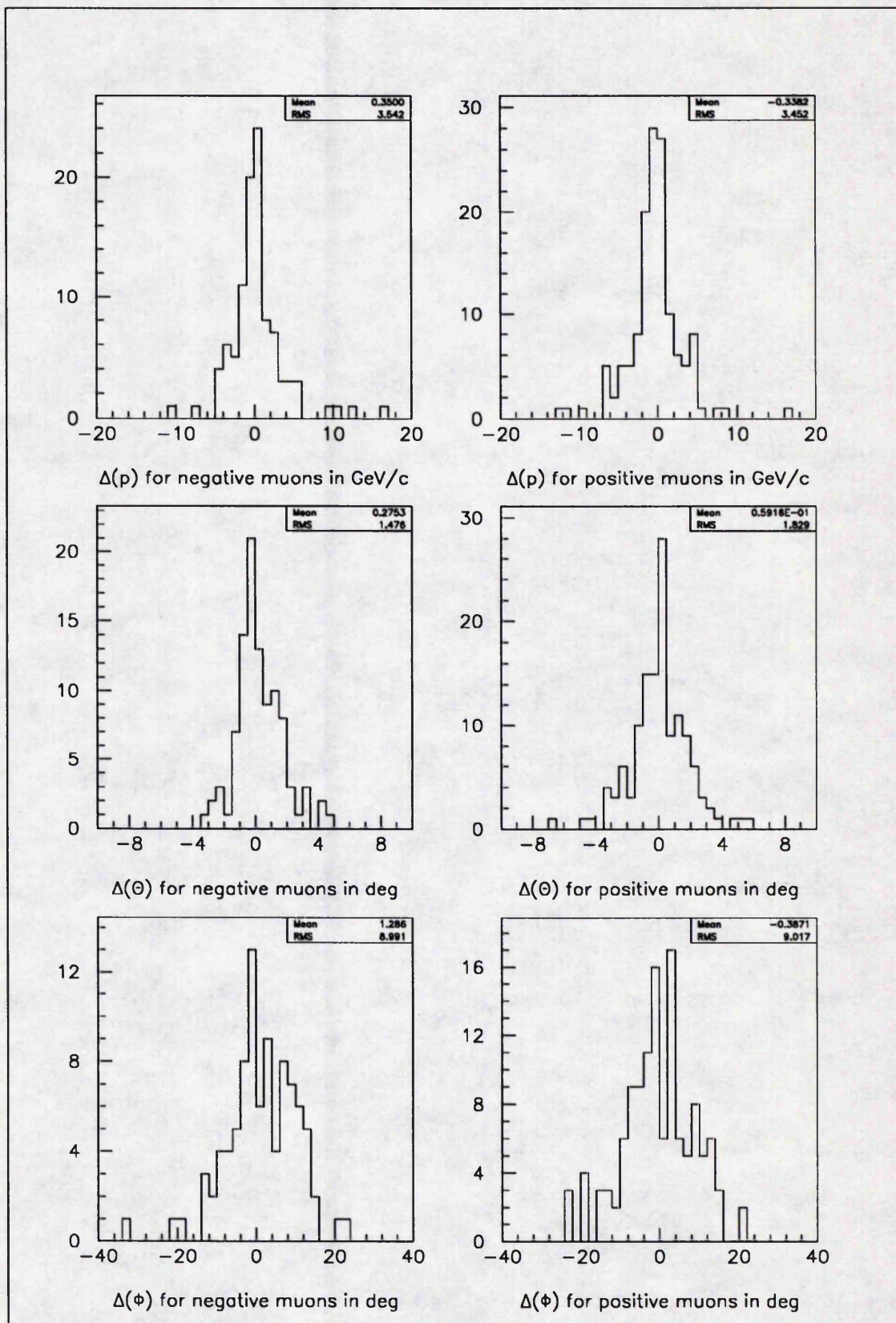


Figure 6.4: Difference between reconstructed and generated track parameters.

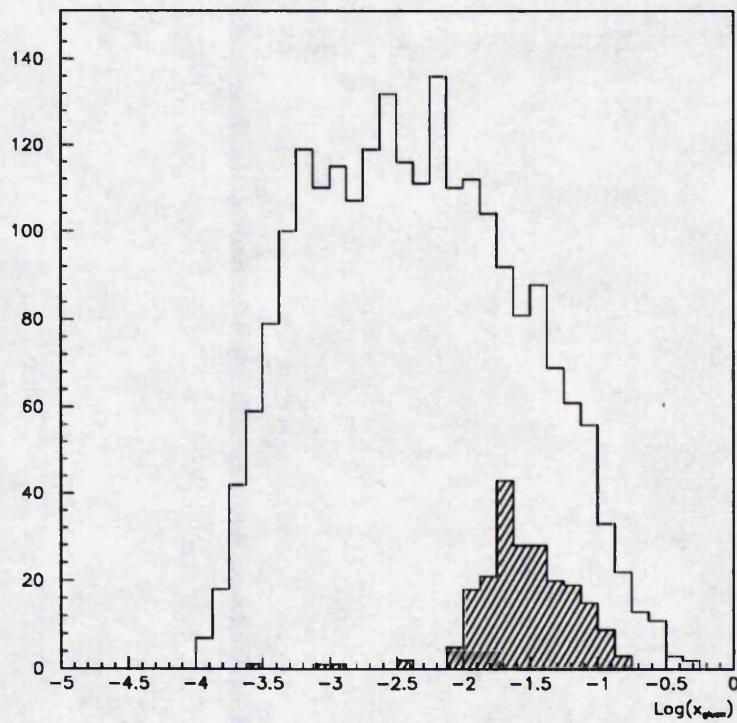


Figure 6.5:  $\text{Log}$  of  $x_{\text{gluon}}$  for all events where the  $J/\psi$  decays to a dimuon pair and for events in which a muon from the  $J/\psi$  decay is reconstructed by the FMD.

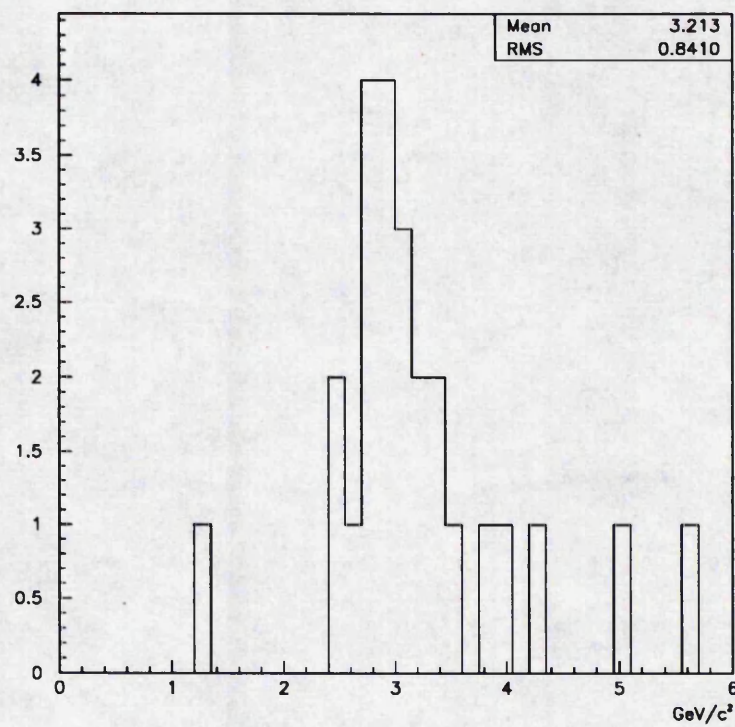


Figure 6.6: Reconstructed invariant mass of  $J/\psi$  meson.

## Chapter 7

# Summary and Conclusion

The simulation studies with single muon tracks generated in front of the FMD show that these tracks are reconstructed reasonably well. However, further work is required to correct for systematic errors associated with extrapolating the track through the iron toroid in the reconstruction code and for the low reconstruction efficiency for certain tracks. The studies also showed the necessity of including the phi layers to improve the momentum resolution of tracks which pass through the octants at large angles in phi relative to their central axes.

Simulations of single muon tracks which pointed in the direction of the FMD and which were generated at the nominal H1 vertex allowed the effect of passage of tracks through the H1 detector to be investigated. It was found that this could be understood in terms of energy loss due to ionisation, multiple Coulomb scattering and the bending of the track in the magnetic field of the solenoid. Using information provided by these studies, muons reconstructed by the FMD in simulations of inelastic  $J/\psi$  production via photon-gluon fusion were corrected for their passage through the H1 detector. Although these simulations gave promising results, they also demonstrated the importance of improving the efficiency of the reconstruction code. Further improvement are expected when the phi layers are included and when the tracks in the forward muon detector are linked to tracks in the forward tracker.

Studies carried out at Manchester on FMD drift chambers using cosmic ray tracks have provided a better understanding of the space-time relation for the drift

cells and of the determination of the charge division coordinate. Measurement of the drift velocity and t-zero of the drift cells of the actual FMD was carried out at HERA using beam halo tracks with reasonably good results, demonstrating that the FMD was working correctly. Simulations of the alignment of the FMD using beam halo provided encouraging results, indicating that the octants can be aligned along their drift and charge division axes to the required accuracy with attainable numbers of tracks. Using real beam halo to align the FMD, results were obtained which were consistent with the simulations, showing that the beam halo simulations describe real beam halo muon tracks in the FMD reasonably well and demonstrating again that the FMD was working correctly.

To conclude, quoting the Chancellor of the Exchequer, Norman Lamont:  
*All the classic ingredients for forward muon detection are now in place.*

# Bibliography

- [1] F. Halzen, A. Martin, *Quarks and Leptons* John Wiley & Sons (1984)
- [2] I. Aitchison, A. Hey, *Gauge Theories in Particle Physics (second ed.)*, Adam Hilger (1989).
- [3] Callan,C.G. and Gross,D.G., *Phys.Rev.Lett.*22,156-159(1969).
- [4] M. Kobayashi, K. Maskawa, *Prog. Theor. Phys.* 49 p.282 (1972).
- [5] G. Altarelli, G. Parisi, *Nucl. Phys.* B126 p.298 (1977).
- [6] E. Kuraev, L. Lipatov, V. Fadin, *Phys. Lett.* B60 p. 50 (1975).
- [7] L. Gribov, E. Levin, M. Ryskin, *Nucl. Phys.* B188 p.555 (1981).
- [8] A. Cooper-Sarkar, R. Devenish, M. Lancaster, *Proceedings of the HERA Workshop Vol.1 Hamburg, Oct. 29-30 p.155 (1991).* ed. W. Buchmüller, G. Ingelman.
- [9] M. Crombie, A. Wegner, *Proceedings of the HERA Workshop Vol.1 Hamburg, Oct. 29-30 p.321 (1991).* ed. W. Buchmüller, G. Ingelman.
- [10] H. Jung, G. Schuler, J. Terron, *J/ $\psi$ -production mechanisms and determination of the gluon density at Hera*, *Proceedings of the HERA Workshop Vol.2 Hamburg, Oct. 29-30 p.712 (1991).* ed. W. Buchmüller, G. Ingelman.
- [11] A. Ali, D. Wyler, *Proceedings of the HERA Workshop Vol.2 Hamburg, Oct. 29-30 p.669 (1991).* ed. W. Buchmüller, G. Ingelman.
- [12] J. Dainton, *Physics at HERA*, *Proceedings of the Annual conference of the HEPP Group of the Institute of Physics, April 2-3, p.79 Sheffield University (1990),* ed. F. Combley.



- [13] T. Helbig, H. Spiesberger, Proceedings of the HERA Workshop Vol.1 Hamburg, Oct. 29–30 p.973 (1991). ed. W. Buchmüller, G. Ingelman.
- [14] Ch. Berger, N. Harnew, F. Schrempp, P. Zerwas, Proceedings of the HERA Workshop Vol.2 Hamburg, Oct. 29–30 p.1029 (1991). ed. W. Buchmüller, G. Ingelman.
- [15] B. Wiik, Proceedings of the HERA Workshop Vol.1 Hamburg, Oct. 29–30 p.1 (1991). ed. W. Buchmüller, G. Ingelman.
- [16] The H1 Collaboration, *Technical Proposal for the H1 Detector*, DESY, Hamburg, (1986).
- [17] M. Düren, K. Rith, Proceedings of the HERA Workshop Vol.1 Hamburg, Oct. 29–30 p.427 (1991). ed. W. Buchmüller, G. Ingelman.
- [18] G. Cozzika, *The H1 Detector*, contributed paper to the Third Int. Conference on Calorimetry in High Energy Physics, Sept.29–Oct.2, Corpus Christi, Texas (1992).
- [19] E. Elsen, *The H1 Trigger and Data Acquisition System*, to be submitted to Nuclear Instruments and Methods (1992).
- [20] J. Meyer (Ed.), *H1SIM manual*, DESY central IBM, 'HERA01.H1SIM' (1992).
- [21] R. Brun et al., *GEANT Detector Simulation Program*, CERN Program Library.
- [22] H. Phillips, *MTREC, Forward Muon Reconstruction Guide*, DESY Central IBM, 'HERA01.H1REC.JOBS(+MTGUIDE)' (1991)
- [23] M. Aguilar-Benitez et al., *Particle Properties Data Booklet* (1992)
- [24] F. Sauli, *Principle of Operation of Multiwire Proportional and Drift Chambers*, 1977.
- [25] A. Metha, *Diploma: Investigation of the Drift Velocity of the Forward Muon Drift Chambers of the H1 Detector*, May 1992.
- [26] P. Emmett, *M.Sc. Dissertation: The Design and Development of a High Resolution Drift Chamber for the H1 Experiment*, July 1990.

- [27] I. Duerdoth, *MOPAL2 Program used to model OPAL drift chambers*.
- [28] A. Metha, *Determination of Drift Velocity, Tzero and Resolution of the Forward Muon Spectrometer*, Dec 1992.
- [29] J. Foster, *QTFMU The Forward Muon QT code*.
- [30] J. Sutton, *Diploma: The Drift Distance Resolution of the Drift Chambers Used in H1 Forward Muon Spectrometer* May 1990.
- [31] C. Hilton, *Diploma: Investigations Concerning the Forward Muon Drift Chambers of the H1 Detector at HERA*, May 1991.
- [32] B. Denby et al., FTPS Collaboration, *Phys. Rev. Lett.* 52,795 (1984).
- [33] R. Barate et al., NA-14 Collaboration, *Z. Phys.* C33,505 (1987).
- [34] J. Aubert et al., EMC Collaboration, *Nucl. Phys.* B213,1 (1983).
- [35] M. de Jong, NMC Collaboration, *PhD Thesis* Utrecht (1991).  
D. Allasia et al., NMC Collaboration, *Phys. Lett.* B258,493 (1991).
- [36] E. Berger, D. Jones, *Phys. Rev.* D23, 1521 (1981).
- [37] A. Donnachie, P. Landshoff, *Nucl. Phys.* B244,322 (1984).
- [38] G. Ingelman, P. Schlein, *Phys. Lett.* B152,256 (1985).
- [39] E. Berger, J. Collins, D. Soper, G. Sterman, *Nucl. Phys.* B286,704 (1987).
- [40] F. Jacquet, A. Blondel, *Proceedings of the Conference on an ep Facility for Europe, Hamburg, (1979)*, ed. U. Amaldi.
- [41] H. Jung, *EPJPSI 2.0 - Monte Carlo generator EPJPSI for J/ψ mesons in high energy electron-proton collisions*, *Proceedings of the HERA Workshop Vol.3 Hamburg, Oct. 29-30 p.1488 (1991)*. ed. W. Buchmüller, G. Ingelman.
- [42] S. Levonian, U. Berthon, T. Naumann, (ed) *H1LOOK, General Purpose H1 Event Display* DESY Central IBM, 'HERA01.H1LOOK.CMZ' deck 'MANUAL' (1992).

## Acknowledgements

I would like to thank the following people:

Mike Ibbotson, who has supervised my work, providing many useful suggestions and comments, and who has provided all necessary support.

Phill Biddulph, Chris Hilton and Andy Metha with whom I worked directly while at DESY, for their stimulating and exciting company at work and also out of work, in particular Chris deserves a special thanks for sharing the experience of 'learning' German with me and being a good friend.

Allister Dann, Graham Bahan and Robert McGowan with whom I shared the experience of doing a Ph.D. over the last three years and the experience of writing-up. Especially Allister who has been a good, honest friend over the last three years, remaining completely calm for almost the entirety of this period. He has been great at putting HEP in perspective and being someone with whom I could share my ignorance. I must also thank him for encouraging me to visit places more exotic than my local bar.

Joe Foster and Ray Thompson for their knowledge of the software and hardware aspects of drift chambers.

John Ellison and Christoph Hoeger for answering many of my queries.

Tony Doyle who provided the initial forward muon simulation and reconstruction code with which I started.

John Banks who provided some genuinely useful computing support.

All my friends from German lessons at Linguothek who were refreshingly different company, being completely unassociated with DESY.

All the technicians with whom I worked on the construction of the octants of the forward muon spectrometer.

All my family who have been very supportive, especially my Uncle Brian and Grandma and Grandad Scallon who have put me up and put up with me for periods during the last three years.

Finally, I would like to thank the entirety of the Manchester high energy physics group and everyone I have been associated with at DESY, who have all been a great bunch of people.